UNIVERSIDADE DE LISBOA
FACULDADE DE CIÊNCIAS

Electromagnetic Device for Axillary Lymph Node Diagnosis

" Documento Definitivo"

Doutoramento em Engenharia Biomédica e Biofísica

Matteo Savazzi

Tese orientada por:
Doutora Raquel Cruz da Conceição
Doutor João Manuel de Almeida Monteiro Felício

Documento especialmente elaborado para a obtenção do grau de doutor

2022

UNIVERSIDADE DE LISBOA
FACULDADE DE CIÊNCIAS

Electromagnetic Device for Axillary Lymph Node Diagnosis

Doutoramento em Engenharia Biomédica e Biofísica

Matteo Savazzi

Tese orientada por:
Doutora Raquel Cruz da Conceição
Doutor João Manuel de Almeida Monteiro Felício

Júri:

Presidente:

- Doutor José Manuel de Nunes Vicente e Rebordão, Investigador Coordenador e Presidente do Departamento de Física da Faculdade de Ciências da Universidade de Lisboa

Vogais:

- Doutora Lourdes Farrugia, Senior Lecturer da Faculty of Science da University of Malta;
- Doutor Lorenzo Crocco, Senior Researcher do Institute for Electromagnetic Sensing of the Environment (Itália);
- Doutor Nuno Miguel de Pinto Lobo e Matela, Professor Auxiliar da Faculdade de Ciências da Universidade de Lisboa;
- Doutora Raquel Cruz da Conceição, Professora Auxiliar com Agregação da Faculdade de Ciências da Universidade de Lisboa (orientadora).

Documento especialmente elaborado para a obtenção do grau de doutor

Trabalho financiado pela Marie Skłodowska-Curie Action (MSCA) com o grant agreement No.764479 e pela Fundação para a Ciência e Tecnologia (FCT) com a bolsa de doutoramento 2021.05385.BD

2022

Acknowledgements

This work was supported by the EMERALD project (funded from the European Union's Horizon 2020 research and innovation programme under the Marie Skłodowska-Curie grant agreement No. 764479), and the Fundação para a Ciência e Tecnologia (under the Strategic Programmes UID/BIO/00645/2020, UIDB/50008/2020, and 2021.05385.BD).

I would like to thank my supervisors, Dr. Raquel Conceição and Dr. João Felício. Thank you for your continuous and tireless support, and for patiently believing in me, especially in the difficult moments. Thank you, Raquel, for being able to treat me as your equal and be protective towards me at the same time; thank you also for considering my ideas as if I were a mature researcher, while always putting my education at the centre of our work. Thank you, João, for being so patient in explaining some concepts to me hundreds of times, never judging my voids; thank you also for taking the time to understand my scientific reasonings in-depth, even (and particularly) when they were too abstruse. Thank you both for tolerating and understanding me when we had different views. You are examples that I will bring with me for the rest of my life.

I sincerely thank Prof. Carlos Fernandes whose advice and criticism were extremely precious to my growth as a student and to this thesis. I also would like to thank Prof. Martin O'Halloran, Dr. Emily Porter, Prof. Hélène Roussel, Dr. Nadine Joachimowicz, Dr. Panagiotis Kosmas, Prof. Francesca Vipiana, and Dr. Jorge Tobon. Thank you very much for your significant contribution to this work, and for hosting me in your labs. I was incredibly lucky to work with all of you even if for short periods or virtually.

I wish to thank all the people who initiated the EMERALD project for giving me a unique opportunity, and for their admirable dedication to the project and organisation of

courses and meetings.

I am sincerely grateful to my host institutions, Instituto de Biofísica e Engenharia Biomédica (IBEB) and Instituto de Telecomuincações (IT), and all the IBEB and IT communities. My special thanks to Dr. Nuno Matela for his insightful suggestions during my yearly assessments.

I would like to thank the doctors of Hospital da Luz, in particular Maria de Lurdes Orvalho, Nuno André Silva, and Tiago Castela for giving a clinical perspective during my research. I would also like to thank the Champalimaud Foundation for providing the CT image that was used to develop the axillary region model presented in this thesis.

A friendly thank you to my colleagues in IBEB, Daniela, Catarina, and Maria, for leisure moments spent together and for their company in the lab. Special thanks to Daniela, for her patience with my questions and for her incredibly lucid answers to tons of doubts I had. A kind thank you to my colleagues in IT, Raquel M., Tomás, Fábio, João S., Guilherme, and Rodrigo for making some stressful days during my PhD thesis writing more enjoyable. Thank you also to all the EMERALD fellows: our (not only) scientific meetings were definitely the funniest part of the project, and an energy boost for the following days. Thank you, Niko, Soroush, Tushar, Olympia, Eleonora, and David for your kind help and contribution to this work.

My affectionate thanks to my *lisboetas* friends for becoming true friends, and for making Lisbon home to me. A deep thank you also to my friends of a lifetime for their affection and unchanged ability to understand me despite time and distances.

Thank you to my parents and brothers for enthusiastically accepting every decision I made, with the only condition being that it brought me happiness. Thank you, Giulia, because as promised this adventure was ours.

Abstract

The diagnosis of axillary lymph nodes (ALNs) is fundamental to determine breast cancer staging before making therapeutical decisions. Non-invasive medical imaging techniques are often used to diagnose ALNs, but they lack sensitivity and specificity. This thesis aims to contribute to the development of microwave imaging (MWI) prototype system to detect and diagnose ALNs.

The dielectric properties of freshly excised animal lymph nodes (LNs) and human ALNs are measured (0.5-8.5GHz) with the Open-Ended Coaxial-Probe technique. The results show that the relative permittivity of healthy ALNs ranges between 30 and 50 at 4.5GHz, which contrasts well with the surrounding fat tissue, potentially enabling ALN detection with MWI. Additionally, the effects of freezing and defrosting of biological tissue dielectric properties are studied, which is motivated by the possibility of measuring previously frozen and defrosted LNs. The results suggest that measuring defrosted tissues does not affect the estimation of their dielectric properties by more than 9% at 4.5GHz, paving the way to measure previously frozen LN

The measured ALN dielectric properties are used to develop an anatomically realistic axillary phantom. The phantom derives from the segmentation of a thoracic computed-tomography scan, and it is made of polymeric containers filled with appropriate tissue mimicking liquids, representing fat and muscle. Finally, ALN microwave tomography is tested (0.5-2.5GHz) on the developed anthropomorphic phantom, using the distorted Born iterative method. The numerical results show that: (i) prior knowledge on the position of muscle tissue is fundamental for ALN detection; (ii) performing two-step measurements, with the antenna set in two different angular positions, can increase the amount of retrievable information, and enhance imaging results. Regarding experimental results, the proposed system can detect an ALN in different positions in the axillary region, which mo-

tivates further studies on ALN MWI.

Keywords **–** Anthropomorphic Phantoms, Axillary Lymph Nodes, Biological Tissue Dielectric Properties, Breast Cancer, Medical Microwave Imaging.

Resumo

O cancro da mama é o tipo de cancro mais comun a nível mundial, e a primeira causa de morte por cancro entre as mulheres. Os gânglios linfáticos axilares (GLAs) são os primeiros órgãos onde as células cancerígenas podem metastizar, e por este motivo, o diagnóstico dos gânglios é fundamental para o estadiamento do cancro da mama e para planear o tratamento terapêutico. O método mais exato de diagnóstico dos GLAs é a biópsia do gânglio sentinela, que é um procedimento cirúrgico, invasivo e que frequentemente resulta numa recuperação mais longa do paciente, risco de infecção e linfedema. Técnicas de imagiologia médica pré-cirúrgica e não invasiva, tais como ultra-som e ressonância magnética, são frequentemente usadas para diagnosticar os GLAs, mas têm limitações a nível da sensibilidade e da especificidade.

A Imagem por Micro-ondas (IMO) é uma técnica emergente de imagem médica que se baseia no contraste de propriedades dieléctricas entre tecidos saudáveis e não-saudáveis em frequências de micro-ondas (tipicamente na banda entre 1 e 10 GHz). Esta técnica tem as vantagens de ser não invasiva, de baixo custo, e potencialmente utilizável para desenvolver dispositivos médicos portáteis. A possibilidade de diagnosticar os GLAs por meio de um sistema de IMO tem sido estudada nos últimos anos, e é apresentada nesta tese como uma técnica complementar às actuais modalidades de imagiologia. Neste contexto, o objectivo desta tese é contribuir para o projeto e o desenvolvimento de um sistema de IMO para diagnosticar os GLAs. Três objectivos principais são identificados: o primeiro é a avaliação das propriedades dieléctricas dos GLAs; o segundo é o desenvolvimento de um modelo antropomórfico e um fantoma físico da região axilar para testar a aplicação pretendida; o terceiro é o desenvolvimento de um protótipo de IMO e a testagem de algoritmos de IMO.

Na primeira parte da tese, as propriedades dieléctricas de gânglios linfáticos animais e de GLAs humanos são medidas *ex-vivo* com o método mais comun do estado da arte, ou

seja, o método sonda coaxial em aberto. Os resultados mostram que a permitividade relativa dos GLAs saudáveis está no intervalo entre 30 e 50 a 4.5 GHz. Estes valores contrastam bem com o tecido adiposo circundante, que tem propriedades dieléctricas baixas, e sugerem que a deteção dos gânglios com IMO é potencialmente viável.

Além disso, dadas as dificuldades encontradas na medição das propriedades dieléctricas dos gânglios linfáticos, é apresentado um método de medição dieléctrica baseado em transmissão para medir tecidos heterogéneos (tais com os gânglios linfáticos). A configuração proposta permite a propagação electromagnética através de amostras de 5mm a 10mm (o que é suficiente para as medições de GLAs), enquanto confina o volume de medida à região de interesse.

Uma outra abordagem à caracterização dieléctrica dos GLAs seria a medição de gânglios linfáticos animais que foram congelados e descongelados *post-mortem*. Para permitir tais medições, o efeito do congelamento e descongelamento de tecidos biológicos sobre as propriedades dieléctricas é estudado. Para tal, são medidas (banda entre 0.5 e 8.5 GHz) as propriedades dieléctricas de 10 amostras de músculo de frango, 10 amostras de fígado bovino e 10 amostras de gordura bovina, cada uma antes e depois do congelamento (até 14 dias) e do descongelamento. Os resultados mostram um ligeiro aumento - menos de 10% - na permitividade complexa dos tecidos com elevado conteúdo de água (músculo e fígado) após o descongelamento, e um efeito negligenciável nos tecidos adiposos.

Na segunda parte da tese, um fantoma da região axilar anatomicamente realístico é desenvolvido para a avaliação experimental do IMO para a detecção dos GLAs. O fantoma deriva da segmentação de um exame de Tomografia Computadorizada torácica e é constituído por contentores impressos em 3D preenchidos com líquidos que representam de forma o mais exata possível as propriedades dielétricas dos tecidos. O fantoma compreende cinco partes impressas em 3D que representam os principais compartimentos de tecidos da região axilar para a aplicação do IMO: gordura, músculo, osso, GLAs, e pulmão. A influência do polímero no acoplamento do campo eléctrico dentro do fantoma é também

estudada. Verifica-se que os compartimentos impressos em 3D alteram o acoplamento do campo eléctrico nos tecidos em 7 dB no máximo, a 4 GHz, o que é aceitável para aplicações de IMO.

Na terceira parte da tese, a IMO da região axilar é avaliada numérica e experimentalmente, usando o modelo antropomórfico da região axilar previamente desenvolvido. A IMO da região axilar apresenta dificuldades que não são comuns noutros sistemas de IMO destinados a aplicações biomédicas. Por exemplo, na IMO da mama e do cérebro, as antenas são normalmente colocadas à volta da região anatómica de interesse, fornecendo informação "angular" suficiente para a reconstrução da imagem. A morfologia da região axilar limita o domínio de medição a um arco ($\approx 70^\circ - 90^\circ$ no plano transversal) em torno da área de interesse, o que impede a medição do signal reflectido a partir de todos os ângulos possíveis. Além disso, a forma côncava da região axilar limita a colocação de antenas e cabos, restringindo também o número de pontos de medição. Finalmente, os GLAs estão normalmente localizados perto de tecido muscular (propriedades dieléctricas semelhantes) que pode ter uma resposta de micro-ondas comparável, o que representa uma dificuldade adicional.

A primeira abordagem à IMO da região axilar consiste em testar um sistema baseado num radar monostático (2-6 GHz), com o objectivo principal de avaliar a resposta muscular. Os algoritmos de IMO baseados no radar reconstituem imagens qualitativas a partir da reflexão das ondas causadas pela descontinuidade das propriedades dieléctricas no meio de propagação. Os resultados mostram que apesar da forte reflexão do músculo - causada pelo elevado contraste dieléctrico entre a gordura e o músculo - um sistema baseado em radar pode distinguir um GLA da gordura circundante.

A segunda abordagem ao IMO da região axilar consiste em testar a tomografia por micro-ondas (TMO) na banda entre 0.5 e 2.5 GHz, usando o algoritmo *distorted Born iterative method (DBIM)*. Os algoritmos de TMO permitem reconstruir imagens quantitativas que podem ser usadas para discriminar GLAs saudáveis e metastisados de acordo

com as suas propriedades dieléctricas. Além disso, os algoritmos TMO exploram a priori a informação disponível sobre a anatomia da região, incorporando um mapa dieléctrico do domínio da imagem no algoritmo de reconstrução.

Como primeira abordagem, o algoritmo é testado numa configuração 2D. Os resultados mostram que - quando a posição da interface músculo-gordura é conhecida a priori - o ALN é detectado com uma boa estimativa das suas propriedades dieléctricas. A robustez do algoritmo aos erros na estimação a priori da interface músculo-gordura também é avaliada: verifica-se que um erro de posicionamento de $\pm 7mm$ não afecta significativamente a detecção do GLA, mas um erro de $\pm 14mm$ causa artefactos.

Como segunda abordagem - mais realista -, a TMO baseada em DBIM, é testada gerando dados com simulações *full wave* ou experimentalmente. Os resultados numéricos demonstram as dificuldades relacionadas com a visão angular limitada, que caracteriza a TMO da região axilar. Além disso, a TMO da região axilar é testada considerando as dificuldades relacionadas com o espaço limitado disponível para a colocação das antenas. A possibilidade de fazer medições de diferentes ângulos de iluminação com um único conjunto de antenas é proposta para aumentar o número de pontos de medição. Os resultados mostram que tal abordagem é eficaz para aumentar a quantidade de informação útil e conduz à obtenção de melhores resultados em termos de imagem.

Como último estudo, uma avaliação experimental da aplicação é realizada usando fantomas antropomórficos com um nível de complexidade crescente. É demonstrado que o sistema proposto pode detectar um GLA em diferentes posições na região axilar, quando se utilizam fantomas homogéneos, ou multi-tecidos. Verifica-se também que, devido a erros de modelação e à falta de medições, o algoritmo falha na estimativa das propriedades dieléctricas do GLA. O último estudo sobre a TMO da região axilar avalia a robustez do método de calibração de dados quantos às alterações do objecto de referência utilizado para a calibração. É mostrado que a possibilidade de medir o fantoma sem GLA é fundamental para minimizar o erro de modelação e, portanto, para obter bons resultados de imagem.

Palavras-chave **–** Cancro da Mama, Caracterização Dieléctrica dos Tecidos Biológicos, Fantomas Antropomórficos, Gânglios Linfáticos Axilares, Imagem Médica por Micro-Ondas.

Contents

List of Figures

List of Tables

List of Acronyms

ALN Axillary Lymph Node

BMI Body Mass Index

CPML Convolutional Perfectly Matched Layer

CT Computed Tomography

DBIM Distorted Born Iterative Method

E-Cal Electronic Calibration

E-field Electric field

EM ElectroMagnetic

EMERALD ElectroMagnetic imaging for a novel genERation of medicAL Devices

FDTD Finite-Difference Time-Domain

LN Lymph Node

MRI Magnetic Resonance Imaging

MUT Material Under Test

MW MicroWave

MWT MicroWave Tomography

OECP Open-Ended Coaxial-Probe

PET Positron Emission Tomography

PLA PolyLactic Acid

R$_x$OECP Reflection-based Open-Ended Coaxial-Probe

RF RadioFrequency

SER Signal to Error Ratio

SLNB Sentinel Lymph Node Biopsy

T$_x$OECP Transmission-based Open-Ended Coaxial-Probe

TM Transverse Magnetic

TNM Tumor-Node-Metastasis

TwIST Two-step Iterative Shrinkage/Thresholding

US UltraSound

VNA Vector Network Analyzer

Chapter 1

Introduction

Breast cancer is the most prevalent type of cancer worldwide, and the first cause of cancer death among women [1]. There were an estimated 2.3 million new cases worldwide (25% of all cancers in women) and 0.7 million cancer deaths (16% of all cancer deaths in women) in 2020 [1]. The incidence and mortality of breast cancer, with respect to other forms of cancer among women, are reported in Fig. 1.1.

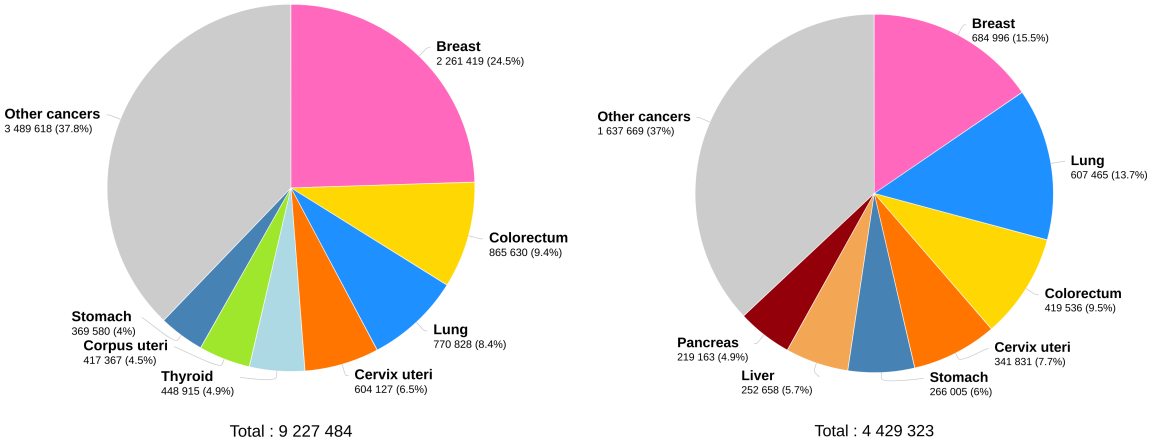

(a) (b)

Figure 1.1: Estimated number of **(a)** new cases and **(b)** deaths for the most common cancers among women (all ages), worldwide, in 2020. Source: Globocan 2020 [1]

According to the Tumor-Node-Metastasis (TNM) [1] classification, different stages of breast cancer can be identified depending on the level of aggressiveness [2]. Stages range from Stage 0 (non-invasive) to Stage 4 (most invasive level). Stage 0 (or Ductual Carcinoma In Situ, DCIS) refers to non-invasive breast cancer, which is confined to the milk ducts. Stages 1 to 3 refer to invasive carcinoma that can involve Axillary Lymph Nodes (ALNs). Stage 4 refers to metastatic carcinoma that involves, not only ALNs, but also distal organs. A more comprehensive characterization of each stage can be found on the AJCC (American Joint Committee on Cancer) Breast Cancer Staging Guidelines online [3].

Lymph Nodes (LNs) are kidney-shaped, encapsulated organs of the lymphatic system, with size ranging from a few millimetres to 1 or 2 cm on their longer axis [4]. They are located along the lymphatic vessels (afferent and efferent lymphatic vessels carry the lymph towards and away from the node) and they serve as a filter for the lymph on its way to the vascular (blood) system. Although widely distributed throughout the body, LNs are concentrated in regions such as the axilla, groin and the mesentery regions [4]. A schematic of the structure of a LN is reported in Fig. 1.2. The structural support of a Lymph Node (LN) is provided by the capsule and the trabeculae. The capsule is a dense connective tissue that surrounds the node; the trabeculae, also composed of connective tissue, are extensions of the capsule into the interior of the node which provide support for blood vessels entering into the nodes. The parenchyma of the LN is divided into cortex and medulla. The cortex, which forms the outer part of the node, consists of a dense mass of lymphatic tissue (reticular framework, follicular dendritic cells, lymphocytes, macrophages and plasma cells) and lymphatic sinuses (the lymph channels). These regions surround the inner medulla, which consists primarily of activated antibody-secreting plasma cells [4].

ALNs can be classified in three levels based on their relative anatomical location. Level

[1]The TNM classification of malignant tumors is an internationally recognized cancer staging notation system, periodically edited by the the American Joint Committee on Cancer (AJCC) and the Union for International Cancer Control (UICC). The TNM staging classifies cancer by (primary) **t**umor size (**T**), nearby lymph **n**odes involvement (**N**) and distant **m**etastases existence (**M**).

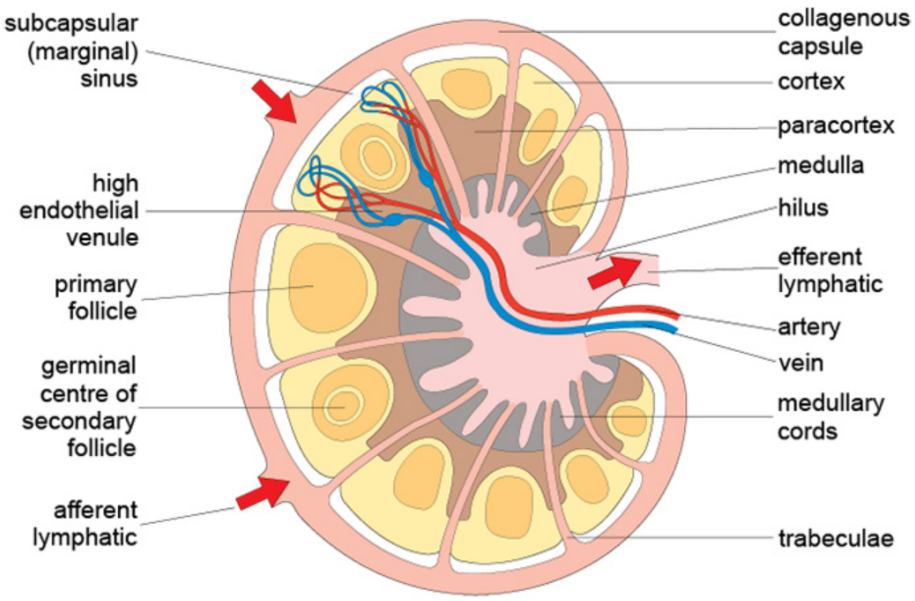

Figure 1.2: Structure of a lymph node (LN). The schematic shows the supporting structures (capsule and trabeculae), the parenchyma and the inner medulla. Afferent and efferent lymphatic vessels are indicated with red arrows. Source: [5]

I ALNs are located in the lower part of the armpit, and are usually surrounded by fat tissue. Their depth (i.e., distance to skin) varies between 14 and 80 mm [6], and correlates to each patient's Body Mass Index (BMI) [7; 8]. Level II ALNs are located between lateral and medial margins of the pectoralis minor muscle, and level III ALNs are medial to the medial margin of the pectoralis minor muscle and inferior to the clavicle[9].

Regarding their physiological function, ALNs drain lymph from the arm, the walls of the thorax, the breast and the upper walls of the abdomen. In fact, about 75% of lymph from the breasts drains into the ALN making the lymphatic system a likely vehicle for breast cancer metastasis. Therefore, the study of ALNs is clinically significant in breast cancer, as the disease status of these nodes is a significant prognostic factor and is crucial for guiding treatment selection [10]. In particular, level I ALNs are more likely to receive drainage from tumour cells first (circa 97% of the cases) [11; 12].

Currently, Sentinel Lymph Node Biopsy (SLNB) is the state-of-the-art method for ALN diagnosis, and it is widely adopted in developed countries. SLNB relies on findings from studies of breast cancer from the late 90s and early 2000s [13; 14]. These studies have shown that breast cancer firstly spreads to one or a few ALNs, known as the sentinel ALN, before it spreads to other ALNs. The sentinel ALN can be identified using vital blue dye and/or a radio-labeled colloid [13; 14].

Several clinical trials showed accuracy higher than 94% and sensitivity between 80% and 90% [13; 15; 16]. However, the sensitivity of the method strongly relies on the physician's experience and intuition [10]. Therefore, high risk of pre-emptive ALN removal is associated with SLNB. This can lead to varying degrees of morbidity such as: limited arm and shoulder motion; risk of infection and lymphedema; paraesthesia; need of regular and specific treatments (e.g., lymphatic drainage), regular visits to a physiatrist and special care when travelling or doing sports. Despite the widespread adoption of SLNB, having prior information about modifications within the ALN is highly valuable, which justifies the development of imaging or sensing methods to detect and analyze the ALNs non-invasively.

The available nonsurgical imaging methods studied in literature include Magnetic Resonance Imaging (MRI), Positron Emission Tomography (PET), Computed Tomography (CT) and UltraSound (US). MRI, used to analyze the primary breast tumour, has been studied to also investigate the existence of ALN metastases [17; 18]. MRI can provide information about the size and morphology of ALNs and additional insight can be obtained by injecting a contrast agent. US [19] demonstrated high specificity in both assessing suspicious ALNs [20] and guiding ALN biopsies [21]. However, US depends significantly on the technician's experience. PET, which has been used for advanced breast cancer stages, has shown high specificity in the identification of metastasized ALNs [22; 23]. This technique is usually combined with CT, which provides anatomical data. However, the PET-CT cannot act as a substitute for SLNB due to high costs and radiation exposure [24]. Last, electrical impedance spectroscopy has been proposed to investigate ALNs when malig-

nancy is suspected based on ultrasound scans [25].

1.1 Aim of the thesis

Microwave imaging is an emerging technology which has been proposed for several applications, including breast cancer diagnosis [26; 27; 28]. This technique relies on the contrast of dielectric properties between healthy and malignant tissues at medical microwave frequencies (typically in the 1 GHz - 10 GHz range). MWI presents several advantages compared to other imaging systems used for breast cancer screening, namely it is low-cost, non-invasive, portable, and it employs non-ionizing radiation. Even though MWI could potentially be valuable to diagnose ALNs non-invasively, only a few efforts - besides those of our research group [29; 30; 31; 32; 33; 34; 35; 36; 37; 38; 39; 40; 41] - have been made in the literature to investigate such an application [24; 42; 43].

In this context, the aim of this Ph.D. project is to contribute to the design and the development of a full MWI prototype system to detect and diagnose ALNs. The specific research objectives can be summarized as follows:

1. Review of the literature of ALN properties, and dielectric measurements of healthy and malignant ALNs (and surrounding tissue) at MW frequencies;

2. Development of computational models and fabrication of physical anatomically-realistic anthropomorphic model (i.e., a phantom) of the axillary region which will allow the assessment of the system performance in a controlled, yet realistic, environment;

3. Design of a MWI setup to operate in the axillary region, implementation of both qualitative and quantitative microwave imaging algorithms, and experimental testing of the MWI setup for ALN examination.

This thesis presents the work developed during the past four years of the Doctoral Programme in Faculdade de Ciências da Universidade de Lisboa (FCUL), at the Instituto de Biofísica e Engenharia Biomédica (IBEB) and Instituto de Telecomunicações - Lisboa (IT), in partnership with the National University of Ireland Galway (Galway, Ireland), the Laboratoire de Génie Electrique et Electronique de Paris at Sorbonne University (Paris, France), the Faculty of Natural and Mathematical Sciences, at King's College London (London, UK), and the Dipartimento di Elettronica e Telecomunicazioni, at Politecnico di Torino (Turin, Italy). Hospital da Luz (Lisbon, Portugal) and Champalimaud Foundation (Lisbon, Portugal) were involved as clinical partners. The Ph.D. project was part of a Marie Skłodowska-Curie ITN consortium, the ElectroMagnetic imaging for a novel genERation of medicAL Devices (EMERALD) network, which is the coherent action of leading European engineering groups involved in electromagnetic (EM) technology for medical imaging. The first three years of research were funded by EMERALD, while the fourth year was funded by Portuguese national agency for science, research and technology (Fundação para a Ciência e a Tecnologia, FCT).

1.2 Structure of the thesis

The structure of the thesis is as follows:

Chapter 2 introduces preliminary concepts required to understand the work developed in this thesis. Firstly, the state-of-the-art methods for the dielectric properties measurements of biological tissues are described. Secondly, the theory behind inverse scattering problems and the distorted Born iterative method are detailed.

Chapter 3 addresses the study of the dielectric properties of ALNs. Firstly, a transmission-based method is proposed for the dielectric measurement of heterogeneous biological tis-

sues; the method was designed *ad hoc* for ALN measurements. Secondly, the measurements of freshly excised animal LNs and human ALNs using the state-of-the-art method are described. Finally, a study on the influence of freezing and defrosting on biological tissue dielectric properties is presented.

Chapter 4 describes the development of an anatomically and dielectrically realistic phantom of the axillary region. Firstly, the development of the computational anatomical model of the axillary region and the fabrication of the physical phantom is described. Secondly, the dielectric properties of the axillary tissues are reviewed, and the fabrication and dielectric characterization of tissue mimicking materials are described. Lastly, the electrical behaviour of the fabricated phantom is discussed, in comparison to a realistic axillary region.

Chapter 5 describes the work developed to assess MWI as a potential technique for ALN screening. Firstly, the influence of the muscle tissue on imaging results is studied using a radar-type MWI setup. Secondly, the feasibility of axillary microwave tomography (MWT) for the detection and dielectric properties estimation of one ALN is assessed. The effect of varying prior information in axillary MWT is investigated using a 2D axillary model. The problem of antenna placement is numerically assessed using a 3D axillary model and full-wave simulation data. A MWT setup is then developed, and the application is experimentally assessed.

Chapter 6 concludes the thesis. In a nutshell, it is argued that ALNs can be imaged with MWs as their dielectric properties have significant contrast compared to the properties of the surrounding fat tissue. However, it is also highlighted that differences between healthy and metastasised ALN are still uncertain. Regarding the development of an anthropomorphic axillary phantom, it is shown that the phantom developed in this thesis is a

good representation of the axillary region and a viable tool for pre-clinical assessment of MWI. As for ALN imaging, it is shown that MWT can be a valid tool for ALN detection, even if the correct estimation of the target dielectric properties remains a challenge. Last, it is argued that MWT outcomes are significantly more reliable when performing a data calibration measurement of the so-called "no-target scenario", which is never possible in clinical practice.

1.3 Contributions

During the past four years, part of the developed work was published. One journal letter is published in IEEE Antenna Wireless and Propagation Letters. One journal paper is published in Sensors, in the Special Issue on "Measurements Techniques of Biological Tissues Dielectric Properties, Updated Data and Current Applications". One journal paper is currently under review in IEEE Journal of Electromagnetics, RF and Microwaves in Medicine and Biology. One chapter was written as part of a book that will be published by Springer. Three conference papers were accepted (and presented) at the 14^{th}, 15^{th} and 16^{th} European Conference on Antennas and Propagation (EuCAP 2020, EuCAP 2021 and EuCAP 2022) and they were published by IEEE. A presentation was given at the 2022 IEEE Conference on Antenna Measurements and Applications (CAMA 2022). The publication list is presented below:

- Savazzi M., Porter E., O'Halloran M., Costa J. R., Fernandes C., Felicío J. M., & Conceição R. C. "Development of a Transmission-Based Open-Ended Coaxial-Probe Suitable for Axillary Lymph Node Dielectric Measurements". 14th European Conference on Antennas and Propagation (EuCAP), Copenaghen, Denmark. IEEE, pp. 1-5, 2020. https://doi.org/10.23919/EuCAP48036.2020.9135778

- Savazzi M., Abedi S., Istuk N., Joachimowicz N., Roussel H., Porter E., O'Halloran

M., Costa J. R., Fernandes C., Felicío J. M., & Conceição R. C. "Development of an Anthropomorphic Phantom of the Axillary Region for Microwave Imaging Assessment". Sensors, vol. 20, no. 17, pp. 49–68, 2020. https://doi.org/10.3390/s20174968

- Savazzi M., Costa, J. R., Fernandes C. A., Felício J. M., & Conceição R. C. "Numerical Assessment of Microwave Imaging for Axillary Lymph Nodes Screening Using Anthropomorphic Phantom". 15th European Conference on Antennas and Propagation (EuCAP), Dusseldorf, Germany. IEEE, pp. 1-4, 2021. https://doi.org/10.23919/EuCAP51087.2021.9410925

- Savazzi M., Felício J. M., Costa J. R., Fernandes C. A., & Conceição R. C. "Study of Freezing and Defrosting Effects on Complex Permittivity of Biological Tissues". IEEE, Antennas and Wireless Propagation Letters, vol. 20, no. 12, pp 2210-2214, 2021. https://doi.org/10.1109/LAWP.2021.3102842

- Savazzi M., Karadima O., Felício J. M., Fernandes C. A., Kosmas P. & Conceição R. C. "Effect of Varying Prior Information in Axillary 2D Microwave Tomography". 16th European Conference on Antennas and Propagation (EuCAP), Madrid, Spain. IEEE, pp. 1-4, 2022. https://doi.org/10.23919/EuCAP53622.2022.9769372

- Vipiana F., & Crocco L., "Electromagnetic Imaging for a Novel Generation of Medical Devices - Fundamental Issues, Methodological Challenges and Practical Implementation", Springer, 2023 (*expected*)

- Savazzi M., Rodriguez D. O., Karadima O., Fernandes C. A., Tobon J. V., Vipiana F., Kosmas P., Felício J. M., & Conceição R. C. "Experimental Assessment of Axillary Lymph Node Microwave Tomography using Anthropomorphic Phantoms",

IEEE Journal of Electromagnetics, RF and Microwaves in Medicine and Biology. (*Early Access*). https://doi.org/10.1109/JERM.2023.3241777

- Savazzi M., Rodriguez D. O., Origlia C., Karadima O., Fernandes C. A., Tobon J. V., Vipiana F., Kosmas P., Felício J. M., & Conceição R. C. "Experimental Assessment of the Effects of Increasing Illumination Angles to Maximise Useful Information in Axillary Microwave Tomography", in *2022 Conference on Antenna Measurements and Applications (CAMA 2022)*, Guangzhou, China. (*Accepted abstract*)

Chapter 2

Background

This chapter reviews some concepts that are important to understand the work developed in this thesis. Knowledge on the biological tissue dielectric measurement techniques described in the literature is essential to pursue the characterization of ALN dielectric properties. Sec. 2.1 describes the state-of-the-art reflection-based open-ended coaxial-probe technique for biological tissue dielectric measurements, as well as details a novel transmission-based technique. Additionally, knowledge on the principles underpinning MicroWave Tomography (MWT) are crucial to understand the image reconstruction algorithms adopted in this thesis. Sec. 2.2 illustrates the theory behind MWT and the tomographic algorithm used in this work.

2.1 Dielectric measurement techniques

Several techniques have been proposed in the literature for dielectric properties measurement of materials. The most common ones are: Open-Ended Coaxial-Probe (OECP), Transmission Line, Free Space, Resonant Cavity, and Parallel Plate methods. A complete review of all the above mentioned techniques can be found in [44]. In this section, a com-

prehensive description is provided for the most common method used for biological tissue measurements: the OECP technique. Additionally, the recent and novel transmission-based OECP proposed in [45] is described here, as it has been valuable for the development of the present work.

The Open-Ended Coaxial-Probe (OECP) is a cut-off section of a coaxial cable [1] which can be used for dielectric measurement. The Material Under Test (MUT) dielectric properties are measured by immersing the probe into the MUT (if liquid or semi-solid), or touching the MUT flat surface (if solid or powder). The ElectroMagnetic (EM) field propagates along the coaxial cable and reflection occurs when the EM field encounters an impedance mismatch between the probe and the MUT. The reflected signals (S_{11}) are measured and then used to retrieve the complex permittivity, $\epsilon^*(\omega)$ of the MUT. The OECP measurement setup and the probe cross-sections are schematically represented in Fig. 2.1 (a) and Fig. 2.1 (b), respectively. The method allows for the measurement of the average complex permittivity of the volume under test. The probe should be selected so that the so-called "sensing volume" only contains the MUT and no other material. The extent of the sensing volume depends upon several factors, including the probe diameter. Therefore, the sample size has to be taken into account and compared to the sensing volume of the probe [46; 47].

The OECP has become the most commonly used method to measure the dielectric properties of tissues for several reasons: sample handling is minimal and non-destructive; and both *ex vivo* and *in vivo* measurements over a broad frequency range are possible [48; 49]. Well-known analytical formulations, which allow the de-embedding of dielectric properties, represent another important advantage for the method. Examples can be found in [50; 51]. Regarding the disadvantages of the OECP, the method assumes a homogeneous

[1] A coaxial cable is a type of electrical cable, composed by an inner conductor surrounded by a tubular insulating (dielectric) layer, surrounded by a tubular conducting shield. The coaxial cable conducts electrical signals, restricting electrical and magnetic fields to the dielectric layer, with little leakage outside the shield. Coaxial cables are considered a good choice to carry weak signals that cannot tolerate interference from the environment (as is the case for dielectric measurements).

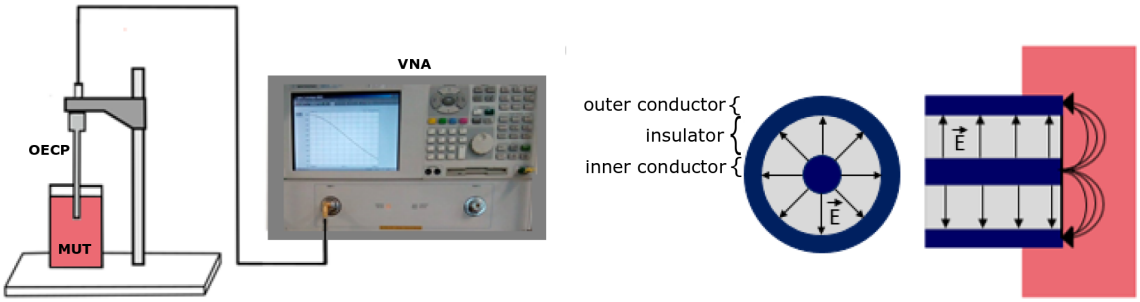

(a) (b)

Figure 2.1: Open-Ended Coaxial-Probe (OECP) technique for dielectric measurement. **(a)** Schematic representation of the measurement setup, including: Vector Network Analyzer (VNA); OECP and coaxial-cables connecting the OECP to the VNA port; liquid sample being measured, i.e., the Material Under Test (MUT). **(b)** vertical and horizontal cross-sections of the OECP, with Electric field ($\vec{E}$) lines indicated.

sample and full contact with the probe (i.e., no air bubbles). As a result, the measurement of heterogeneous samples (such as Axillary Lymph Node (ALN)s) present critical challenges [52]. Finally, the method is very sensitive to small discrepancies in the setup (e.g., cable bending), which makes it very hard to acquire stable and reliable data.

Transmission-based Open-Ended Coaxial-Probe (T_xOECP): Meaney et al. [45] recently developed a Transmission-based Open-Ended Coaxial dielectric Probe (T_xOECP) which aims to overcome some of the limitations of the state-of-the-art (reflection-based) OECP method, from this point onwards designated as Reflection-based Open-Ended Coaxial-Probe (R_xOECP). A schematic representation of the setup is shown in Fig. 2.2, where the end of the two coaxial probes are immersed in the MUT. In this configuration, one of the probes emits the radiofrequency (RF) signals, while the other records them. The RadioFrequency (RF) energy propagates through the MUT over distance d. However, as discuss in [45], this distance is limited by the sensitivity of the measurement equipment (i.e., the Vector Network Analyzer (VNA)). In fact, the authors mention that d can be as large as 20 mm

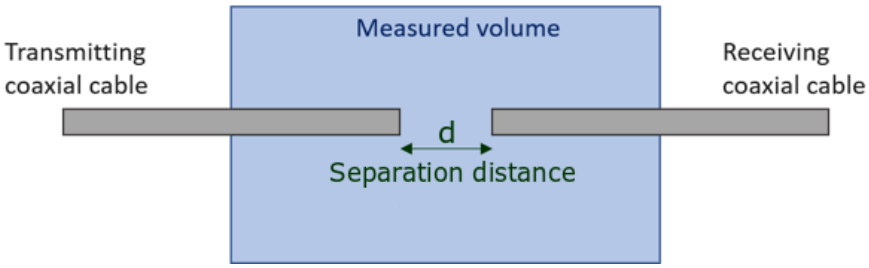

Figure 2.2: Schematic representation of Meaney et al.'s [45] transmission-based Open-Ended Coaxial-Probe (OECP) for dielectric measurements. Two OECP (transmitting and receiving) are immersed inside the Material Under Test and placed in the same direction, facing each other. The separation distance is the sensing depth of the measurement instrument.

for their application and equipment, as a consequence of the low transmission efficiency of the probes (the latter may be perceived as "low-efficiency" antennas). Nevertheless, this sensing volume is much greater compared to the order of a few millimeters in the state-of-the-art R$_x$OECP (the exact value depends on the diameter of the probe and the dielectric properties of the MUT, as reported in [46]).

2.2 Microwave tomography

A microwave tomography problem consists of reconstructing the dielectric properties of an unknown target region D (imaging domain), which is immersed in a known background medium, from the scattered Electric field (E-field) measured by a set of probing antennas on a surface S, external to D. Fig. 2.3 shows a 2D view of a typical MWT setup with a circular antenna array placed on S (a line in the 2D representation), around the imaging domain D, where an unknown object (blue object in Fig. 2.3) is placed. For a measurement at location $(\mathbf{r}_n, \mathbf{r}_m) \in S$, at a given angular frequency ω, the relationship between the field scattered from D and the unknown dielectric profile $\epsilon(\mathbf{r})$ within D can be written as

follows [53]:

$$\begin{aligned}\mathbf{E}_S(\mathbf{r}_n,\mathbf{r}_m) &= \mathbf{E}_T(\mathbf{r}_n,\mathbf{r}_m) - \mathbf{E}_B(\mathbf{r}_n,\mathbf{r}_m) = \\ &= \omega^2\mu \int_D \big[\epsilon(\mathbf{r}) - \epsilon_b(\mathbf{r})\big]\mathbf{G}_B(\mathbf{r}_n,\mathbf{r}) \cdot \mathbf{E}_T(\mathbf{r},\mathbf{r}_m)\, d\mathbf{r}\end{aligned} \tag{2.1}$$

where $\mathbf{r} \in D$, and $\mathbf{r}_m, \mathbf{r}_n \in S$, as indicated in Fig.2.3; $\mathbf{E}_S$ is the scattered E-field; $\mathbf{E}_T$ is the total E-field, measured in the presence of the unknown object under test; $\mathbf{E}_B$ is the background E-field, measured in the absence of the unknown object under test; $\mathbf{G}_B(\mathbf{r}_n,\mathbf{r})$ is the Green's function for the background.

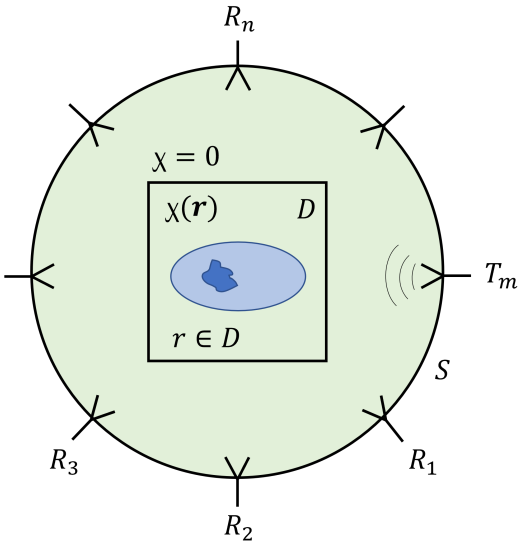

Figure 2.3: Schematic of a generic microwave tomography scenario. A region D with unknown dielectric properties is surrounded by an array of antennas distributed over the measurement domain S (defined by a circle in the present 2D view). The contrast function $\chi(\mathbf{r})$ is unknown inside D, while it is zero outside D.

The difference between the complex permittivity of the object $\epsilon(\mathbf{r})$ and the background $\epsilon_b(\mathbf{r})$ will be referred to as the contrast function $\chi(\mathbf{r}) = \epsilon(\mathbf{r}) - \epsilon_b(\mathbf{r})$. In a set of measurements (several transmitter-receiver pairs), a system of equations in the form of Eq. 2.1 can be written. However, the solution to such a system is not trivial due to the following com-

plications: i) the number of unknowns in D (i.e. $\chi(\mathbf{r})$) is much greater than the number of equations (i.e. measurements), leading to an underdetermined system that - by definition - does not have a unique solution; ii) the solution does not continuously depend on the data, meaning that small perturbations of the data may involve discontinuities in the solution; iii) the total field within D ($\mathbf{E}_T(\mathbf{r}, \mathbf{r}_m)$) is unknown (it cannot be measured non-invasively) and it is itself a function of $\chi(\mathbf{r})$, making the problem non-linear.

2.2.1 Distorted Born Iterative Method (DBIM)

The Distorted Born Iterative Method (DBIM) is an iterative algorithm, originally proposed in [54]. DBIM has been widely used numerically for medical MWT reconstruction [55; 56], and has been experimentally tested both for the detection of simple cylindrical targets [57; 58], and, more recently, for breast [59] and brain [60] medical MWT. The main advantage of iterative tomographic algorithms lies in the possibility to explore available prior information, incorporating a guess of the dielectric map of the investigated body area (*initial guess*) into the reconstruction algorithm. Conversely, iterative algorithms have to solve an EM-problem at each iteration and hence are associated with a longer reconstruction time.

To linearize the system of scattering equations in the form of Eq. 2.1, the DBIM exploits the distorted-Born approximation, which consists of approximating the total field within D by the field in an estimated heterogeneous background profile (i.e., $\mathbf{E}_T(\mathbf{r}, \mathbf{r}_m) \approx \mathbf{E}_B(\mathbf{r}, \mathbf{r}_m)$). It should be noted that such approximation is acceptable if the scattering is weak, i.e., if the scattered field $\mathbf{E}_S(\mathbf{r}_n, \mathbf{r}_m)$ is much weaker than the background field $\mathbf{E}_B(\mathbf{r}_n, \mathbf{r}_m)$ [53]. Weak scattering implies little contrast and/or small size of the scatterer. If valid, the distorted-Born approximation provides a simple linear relationship between

the data and the unknown contrast function $\chi(\mathbf{r})$, which allows to re-write Eq. 2.1 as:

$$\mathbf{E}_T(\mathbf{r}_n, \mathbf{r}_m) - \mathbf{E}_B(\mathbf{r}_n, \mathbf{r}_m) \approx \omega^2 \mu \int_D \chi(\mathbf{r})\, \mathbf{G}_B(\mathbf{r}_n, \mathbf{r}) \cdot \mathbf{E}_B(\mathbf{r}, \mathbf{r}_m)\, d\mathbf{r} \tag{2.2}$$

The DBIM algorithm consists of the following steps:

1. Initialisation of a known background profile $\epsilon_b(\mathbf{r})$, hereafter referred as *initial guess* (in the absence of *a priori* information, $\epsilon_b(\mathbf{r})$ can be assumed as equal to the permittivity of the immersion medium, constant over space);

2. *Forward problem* resolution: computation of the background E-field at the antennas and inside D, using $\epsilon_b(\mathbf{r})$. As a result, $\mathbf{E}_B(\mathbf{r}_n, \mathbf{r}_m)$, $\mathbf{G}_B(\mathbf{r}_n, \mathbf{r})$, and $\mathbf{E}_B(\mathbf{r}, \mathbf{r}_m)$ are updated. This step requires the use of an EM solver which will be referred to in the following text as *forward solver*.

3. *Inverse problem* resolution: the (underdetermined) linear system of equations in the form of Eq. 2.2 is solved to find an approximated solution to the contrast $\chi(\mathbf{r})$. Sec. 2.2.1.1 illustrates the method that will be adopted in this thesis to build the linear discrete system of scattering equation; while Sec. 2.2.1.3 briefly introduces the inversion method.

4. Background update: the background profile is updated adding the contrast function computed at step 3, as follows: $\epsilon_b^{t+1}(\mathbf{r}) = \epsilon_b^t(\mathbf{r}) + \chi^{t+1}(\mathbf{r})$, where index t refers to the t^{th} iteration.

5. The algorithm goes back to step 2.

6. Termination: the algorithm ends when an *a priori* chosen number of iterations is reached. Alternatively, one may also adopt a stopping criteron based on the *Residual* error which is defined as: $Residual = ||M_E^t - M_M^t||_2$ where M_E^t and M_M^t are complex vectors that collect the "experimental" and "modeled" fields at the t^{th} iteration

respectively, at the antenna locations; and where $||\cdot||_2 = \sqrt{\sum|\cdot|^2}$ is the notation for the L^2 norm adopted in this thesis.

In summary, the DBIM algorithm alternates between *forward* and *inverse* solutions, updating the background profile at each iteration until convergence is reached in the minimization of the contrast function.

2.2.1.1 Multiple-frequency approach to define the linear system of scattering equations

This section illustrates the method that was used - at each DBIM iteration - to build a linear system of scattering equations. The ultimate goal of a MWT algorithm is to estimate the complex permittivity profile of the unknown region over a set of discrete frequencies. Rather than reconstructing the profile independently at each frequency, the algorithm employed in this thesis takes advantage of the assumed frequency dependency of tissue dielectric properties [61]. Such assumption reduces the number of degrees of freedom in the system, hence restricting the size of the solution space and easing the computational burden of the imaging algorithm. In the adopted algorithm, the dispersive behaviour of tissue properties was modelled using a single-pole Debye model as proposed in [55]. The relaxation time constant τ is assumed to be invariant among all tissues to keep the dispersion model linear with respect to the unknown parameters and to reduce the number of unknowns.

As a result, to achieve a solution of the multiple-frequency system, Eq. 2.2 can be rewritten substituting the complex permittivity variables by the frequency-dependent Debye model (with a known time-constant). The resulting equation is linear in the remaining 3 Debye parameters: ϵ_∞, $\Delta\epsilon$, σ_s. The contrast function of these three parameters $\delta(\epsilon_\infty)$, $\delta(\Delta\epsilon)$, $\delta(\sigma_s)$ are the new unknowns over $\mathbf{r} \in D$.

For a set of N antennas, there are N^2F total frequency domain measurements, where F is the number of discrete frequencies to be included in the solution. Redundant data from

reciprocal channels are discarded to retain a single unique measurement for each transmit-receive antenna pair. Monostatic data are also discarded since these observations include the source field. Each of the remaining MF measurements, where $M = \frac{N(N-1)}{2}$, yields a pair of real and imaginary vector equations. The resulting set of $2MF$ integral equations (real and imaginary part are separated) can be discretized over the reconstruction region D by using the same uniform voxel basis used in the *forward solution*. The discretized linear system takes the form of:

$$\mathbf{Ax} = \mathbf{y} \tag{2.3}$$

where **A** is the propagation matrix of size $2MF$-by-$3K$, K is the number of discrete elements (voxels) inside the reconstruction domain D; **y** is the vector of the scattered fields recorded at the receivers, of size $2MF$-by-1. **x** is the unknown vector of size 3K-by-1, which contains the contrast functions of the three Debye parameters for each of the K voxels in D. The discritized linear system $\mathbf{Ax} = \mathbf{b}$ is structured as follows [55]:

$$\begin{bmatrix} \Re\{\mathbf{B}_1^{\infty}\} & \Re\{\mathbf{B}_1^{\Delta}\} & \Re\{\mathbf{B}_1^{\sigma}\} \\ \Im\{\mathbf{B}_1^{\infty}\} & \Im\{\mathbf{B}_1^{\Delta}\} & \Im\{\mathbf{B}_1^{\sigma}\} \\ \Re\{\mathbf{B}_2^{\infty}\} & \Re\{\mathbf{B}_2^{\Delta}\} & \Re\{\mathbf{B}_2^{\sigma}\} \\ \Im\{\mathbf{B}_2^{\infty}\} & \Im\{\mathbf{B}_2^{\Delta}\} & \Im\{\mathbf{B}_2^{\sigma}\} \\ \multicolumn{3}{c}{\cdots\cdots\cdots\cdots} \\ \Re\{\mathbf{B}_d^{\infty}\} & \Re\{\mathbf{B}_d^{\Delta}\} & \Re\{\mathbf{B}_d^{\sigma}\} \\ \Im\{\mathbf{B}_d^{\infty}\} & \Im\{\mathbf{B}_d^{\Delta}\} & \Im\{\mathbf{B}_d^{\sigma}\} \\ \multicolumn{3}{c}{\cdots\cdots\cdots\cdots} \\ \Re\{\mathbf{B}_M^{\infty}\} & \Re\{\mathbf{B}_M^{\Delta}\} & \Re\{\mathbf{B}_M^{\sigma}\} \\ \Im\{\mathbf{B}_M^{\infty}\} & \Im\{\mathbf{B}_M^{\Delta}\} & \Im\{\mathbf{B}_M^{\sigma}\} \end{bmatrix} \begin{bmatrix} \delta(\boldsymbol{\epsilon_\infty}) \\ \delta(\boldsymbol{\Delta\epsilon}) \\ \delta(\boldsymbol{\sigma_s}) \end{bmatrix} = \begin{bmatrix} \Re\{\mathbf{E}_{S,1}\} \\ \Im\{\mathbf{E}_{S,1}\} \\ \Re\{\mathbf{E}_{S,2}\} \\ \Im\{\mathbf{E}_{S,2}\} \\ \vdots \\ \Re\{\mathbf{E}_{S,d}\} \\ \Im\{\mathbf{E}_{S,d}\} \\ \vdots \\ \Re\{\mathbf{E}_{S,M}\} \\ \Im\{\mathbf{E}_{S,M}\} \end{bmatrix} \tag{2.4}$$

where $\Re\{\cdot\}$ and $\Im\{\cdot\}$ operators indicate the real and imaginary parts of the complex argument. In Eq. 2.4, the vector of unknowns on the right-hand side of Eq. 2.4 is composed of

three vectors of equal size 1-by-K: $\delta(\boldsymbol{\epsilon_\infty})$, $\delta(\boldsymbol{\Delta\epsilon})$, $\delta(\boldsymbol{\sigma_s})$. These sub-vectors contain the contrast values for the respective Debye parameters ϵ_∞, $\Delta\epsilon$, σ_s, for each of K voxels in D. In Eq. 2.4, $\mathbf{B}_d^p$ and $\mathbf{E}_{S,d}$ are defined as:

$$\mathbf{B}_d^p = \begin{bmatrix} c_p(\omega_1)\left[b_1^d(\omega_1)\cdots b_K^d(\omega_1)\right] \\ c_p(\omega_2)\left[b_1^d(\omega_2)\cdots b_K^d(\omega_2)\right] \\ \vdots \\ c_p(\omega_F)\left[b_1^d(\omega_F)\cdots b_K^d(\omega_F)\right] \end{bmatrix}, d \in \{1,2,...,M\}, \quad p \in \{\infty, \Delta, \sigma\} \tag{2.5}$$

$$\mathbf{E}_{S,d} = \begin{bmatrix} E_{S,d}(r_m, r_n, \omega_1) \\ E_{S,d}(r_m, r_n, \omega_2) \\ \vdots \\ E_{S,d}(r_m, r_n, \omega_F) \end{bmatrix}, d \in \{1,2,...,M\} \tag{2.6}$$

where $b_k^d(\omega) = \omega^2\mu\mathbf{G}_B(r_n, r_k, \omega)\mathbf{E}_B(r_k, r_m, \omega)$, $c_\infty(\omega) = 1$, $c_\Delta(\omega) = (1 + j\omega\tau)^{-1}$, and $c_\sigma(\omega) = (j\omega\epsilon_0)^{-1}$.

In this thesis, all tomographic reconstructions were performed using the linear system presented in Eq. 2.3, including the cases where only a single frequency point was considered. In those cases, solving for $\delta(\epsilon_\infty)$, $\delta(\Delta\epsilon)$, $\delta(\sigma_s)$ (and not for real and imaginary part of complex contrast χ) increases the number of unknowns, though it eases the algorithm implementation. This is common practice in the literature [62; 63; 64] and does not affect image reconstruction.

2.2.1.2 Frequency hopping

The frequency hopping approach was often used throughout the thesis to explore multi-frequency information. Frequency-hopping entails reconstructing lower frequencies first, and then using the resulting dielectric map as the initial guess to subsequent (higher) frequencies. This allows to initially exploit the stabilizing effect of lower frequencies, to-

gether with the finer resolution of higher frequencies, resulting in an enhanced imaging performance as reported in [56; 58; 60].

2.2.1.3 Inverse solution

The linear system of scattering equations in Eq. 2.4 is ill-posed and significantly underdetermined, as $2MF << 3K$. To solve Eq. 2.4, the basic idea is to minimize the least square (LS) object function $f(x) = ||Ax - b||_2^2$. However, in most cases, A is considerably ill-conditioned and the LS solution has a high norm. To obtain a reliable solution, regularization methods can be used to limit the norm. To penalise the norm of the solution, many methods define a solution x that minimizes the convex object function, $F(x)$, defined as the sum between an LS function, $f(x)$, and a regulariser function ,$g(x)$, defined as:

$$F(x) = f(x) + g(x) \tag{2.7}$$

$$\begin{cases} f(x) = ||Ax - b||_2^2 \\ g(x) = \lambda\Phi(x) \end{cases} \tag{2.8}$$

where $\lambda \in [0, +\infty]$ is a weighting parameter and $\Phi(x)$ is a regularization function, which is usually chosen as the L^1 norm or L^2 norm.

In this thesis, Two-step Iterative Shrinkage/Thresholding (TwIST) method [65] was adopted to solve the minimization problem of Eq. 2.7. The TwIST algorithm was already tested to solve inverse scattering problems showing fast convergence [56].

2.2.1.4 Data calibration

In light of the DBIM algorithm description in Sec. 2.2.1, it should be clear that - referring to Eq. 2.2 - the total E-field $\mathbf{E}_T(\mathbf{r}_m, \mathbf{r}_n)$ corresponds to the data (i.e., to the measured S-parameters $S_T^{meas}(\mathbf{r}_m, \mathbf{r}_n)$), while the background fields ($\mathbf{E}_B(\mathbf{r}_m, \mathbf{r}_n)$ and $\mathbf{E}_B(\mathbf{r}_n, \mathbf{r})$) are

computed using the *forward model* at each DBIM iteration. Due to such measurement-model mismatch, a calibration of the data becomes necessary to tune $\mathbf{E}_T(\mathbf{r}_m, \mathbf{r}_n)$ with $\mathbf{E}_B(\mathbf{r}_m, \mathbf{r}_n)$ and $\mathbf{E}_B(\mathbf{r}_n, \mathbf{r})$.

The most common method used in the literature to perform such calibration was proposed in [66]. The method considers a known reference imaging domain in both the measurement domain and in the *forward model* domain. Referring to the same known reference scenario, the measured S-parameters and the modelled E-field at the antennas are used to calibrate $\mathbf{S}_T^{meas}(\mathbf{r}_m, \mathbf{r}_n)$, using the following formula:

$$\mathbf{E}_T^{cal}(\mathbf{r}_m, \mathbf{r}_n) = \mathbf{S}_T^{meas}(\mathbf{r}_m, \mathbf{r}_n) * C(\mathbf{r}_m, \mathbf{r}_n) \tag{2.9}$$

where $\mathbf{E}_T^{cal}(\mathbf{r}_m, \mathbf{r}_n)$ is the total field corresponding to the measured S-parameters, after calibration, and

$$C(\mathbf{r}_m, \mathbf{r}_n) = \frac{\mathbf{E}_{ref}^{model}(\mathbf{r}_m, \mathbf{r}_n)}{\mathbf{S}_{ref}^{meas}(\mathbf{r}_m, \mathbf{r}_n)} \tag{2.10}$$

where $\mathbf{E}_{ref}^{model}(\mathbf{r}_m, \mathbf{r}_n)$ is the E-field at the sources computed by the *forward model*, and $\mathbf{S}_{ref}^{meas}(\mathbf{r}_m, \mathbf{r}_n)$ are the S-parameters measured at the sources, in the reference scenario.

Chapter 3

The dielectric properties of axillary lymph nodes

Knowledge on ALN dielectric properties, and the assessment of the level of contrast between healthy and metastasized ALNs is of crucial interest to validate MWI as a potential technique for ALN screening. However, only a few studies in the literature have reported the dielectric properties of lymph nodes at MW frequencies. As will be discussed in detail in this chapter, such studies are rather incomplete or important information about the repeatability of the measured data is missing. In this context, the main objective of this chapter is the characterization of the dielectric properties of healthy and malignant ALNs at MicroWave (MW) frequencies.

The main challenge is the heterogeneity of the tissues under study, which is a critical issue in the application of the state-of-the-art measurement methods for tissue dielectric properties. Indeed, after their excision, ALNs are often surrounded by a variable amount of fat, which affects the estimated permittivity (generally fat results in lower dielectric constant, due to its low water-content). The second challenge in ALN dielectric measurement is the restrictions in human tissue handling. Once ALNs are surgically excised, they are

sent to pathology, and further analyzed. Given the importance of this analysis, ALNs must be handled very carefully and cannot be cut or punctured before reaching the pathologist. This is a very significant constraint that must be taken into account, since accurate dielectric measurements of ALN content would benefit from directly measuring the internal cross-section of the node.

Given the above considerations, to pursue ALN dielectric characterisation, the present thesis focuses on the following tasks:

- Development of a novel dielectric measurement technique (the transmission-based OECP), which is more suitable for the measurement of heterogeneous tissues. The measured dielectric properties should refer to a volume, that is large enough to include not only the superficial fat layer, but also the internal part of the node. In this way, the challenges posed by the heterogeneity of ALNs can be overcome. The measurement technique should be compatible with the above mentioned limitations in human ALN handling. The task includes the numerical and experimental validation of the technique using known materials.

- Measurement of freshly excised LNs with the state-of-the-art method (the reflection-based OECP). Human ALNs and animal LNs were measured. Since animal samples do not have any constraints in terms of how they can be handled, valuable information about ALNs may be inferred measuring the dielectric properties of the inner content of animal LNs.

- Given the limited amount of metastasised human ALNs that were measured for the purpose of this work, one possibility would be to measure LNs excised from dead animals (e.g., cats and dogs) which may have been diagnosed with mammary cancer. *Ex-vivo* characterization of biological tissues would benefit from the flexibility of measuring previously frozen tissue samples. However, to infer reliable conclusions

on LN dielectric properties, it is important to study whether the freezing and defrosting processes affect the dielectric properties of biological tissues, which became an additional objective of the present thesis. To this purpose, the dielectric properties of different biological tissues were measured before and after freezing and defrosting them, comparing the results.

The remainder of the chapter is as follows: Sec. 3.1 reviews the existing literature on LN dielectric properties; Sec. 3.2 describes the development of the transmission-based OECP studied *ad hoc* for LN measurements; Sec. 3.3 reports the measurements performed on freshly excised human and animal LNs; Sec. 3.4 illustrates the study of freezing and defrosting effects on the complex permittivity of biological tissues.

The experimental validation of the transmission-based OECP, and the dielectric measurement campaign on animal LNs and human ALNs were conducted in collaboration with the Translational Medical Device (TMD) Lab, at the National University of Ireland Galway (Galway, Ireland). I visited the TMD Lab for two months during the period of March-May 2019, a planned secondment within EMERALD.

The work developed in this chapter is published in three different papers, each of them corresponding to one of the three tasks listed above. The development of a transmission-based open-ended coaxial probe for the measurement of ALN dielectric properties is presented in:

- Savazzi M., Porter E., O'Halloran M., Costa J. R., Fernandes C., Felício J. M., & Conceição R. C. "Development of a Transmission-Based Open-Ended Coaxial-Probe Suitable for Axillary Lymph Node Dielectric Measurements". IEEE, 2020 14th European Conference on Antennas and Propagation (EuCAP), pp. 1-5, 2020. DOI: 10.23919/EuCAP48036.2020.9135778

The measurements of freshly excised human ALNs and animal LNs with the reflection-based OECP are reported in:

- Savazzi M., Abedi S., Istuk N., Joachimowicz N., Roussel H., Porter E., O'Halloran M., Costa J. R., Fernandes C., Felício J. M., & Conceição R. C. "Development of an Anthropomorphic Phantom of the Axillary Region for Microwave Imaging Assessment". Sensors, vol. 20, no. 17, pp. 49–68, 2020. DOI:10.3390/s20174968

The study of freezing and defrosting effects on the dielectric properties of biological tissues is presented in:

- Savazzi M., Felício J. M., Costa J. R., Fernandes C. A., & Conceição R. C. "Study of Freezing and Defrosting Effects on Complex Permittivity of Biological Tissues". IEEE, Antennas and Wireless Propagation Letters, vol. 20, no. 12, pp 2210-2214, 2021. DOI: 10.1109/LAWP.2021.3102842

Finally, a comprehensive review on ALN dielectric properties will be published in a chapter entitled "The Dielectric Properties of Axillary Lymph Nodes", in the following book:

- Vipiana F., & Crocco L., "Electromagnetic Imaging for a Novel Generation of Medical Devices - Fundamental Issues, Methodological Challenges and Practical Implementation", Springer, 2023 (*expected*)

3.1 Previous studies on lymph node dielectric properties

This section reports previous studies that characterized human LN dielectric properties, prior to the work developed in this thesis.

Joines et al. [67] reported measurements of 2 metastasised LNs from 2 different patients, in the frequency range from 50 to 900 MHz. Measurements were conducted between 1 and 2 hours after tissue excision, once the tissue reached room temperature (23-25 ºC). For each sample, the measurements were repeated in 3 different locations (6 measurements in total).

Results, in terms of average relative permittivity ϵ_r and average conductivity σ, are reported in Fig. 3.1. The average Standard Error on the Mean (SEM) over frequency was $\pm 7\%$ for relative permittivity and $\pm 9\%$ for conductivity.[1] In that study, no measurement of healthy LNs were conducted, and so differences between healthy and metastasised LNs were not inferred. Additionally, Joines *et al.* did not provide details on the sample preparation nor on the tissue composition under the measurement sites. The latter is critical due to LN heterogeneity which can affect the measurements. It should also be noted that the anatomical sites of the excised LNs were not specified.

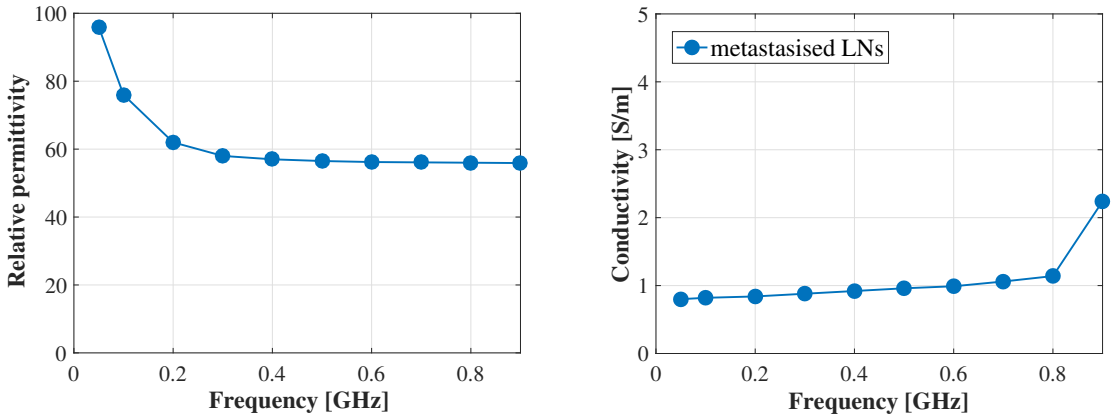

(a) (b)

Figure 3.1: Metastasised Lymph Node (LN) dielectric properties reported by Joines et al. [67]. Data are averaged over 6 measurements (2 LNs at 3 different locations). **(a)**: relative permittivity; **(b)** conductivity.

Choi et al. [42] measured 27 ALNs (either healthy or metastasised) and 7 "pure (breast) cancer tissue" samples, from 12 patients diagnosed with invasive breast carcinoma. Data were sampled in the range from 0.5 to 30 GHz. The results of the study are reported in Fig. 3.2. The authors concluded that ALN dielectric properties are sensitive to cancer cell

[1]The Standard Error on the Mean (SEM) reported in [67] was computed as an average value among several biological tissue measurements (not only LNs).

presence. In particular, cancer tissue and metastasised nodes exhibit high values of relative permittivity at low-GHz and conductivity at high-GHz frequencies, and pronounced dielectric relaxation between 15 and 30 GHz. However, the problem of fat surrounding ALN was not addressed; this can be critical as results may considerably vary depending on the amount of fat in the sensing volume of the probe. This will be discussed in detail in Sec. 3.3.

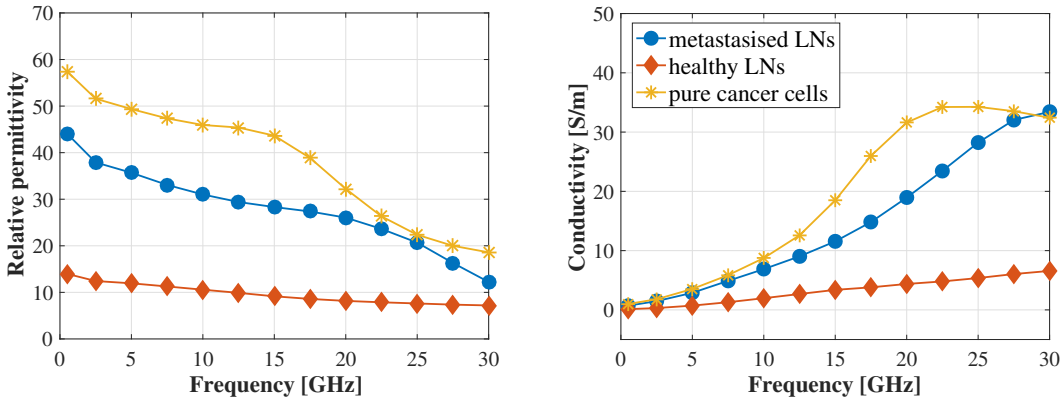

(a) (b)

Figure 3.2: Dielectric properties of "pure (breast) cancer cells", metastasised and healthy Axillary Lymph Nodes (ALNs), reported by Choi *et al.* [42]. **(a)** real part of relative permittivity; **(b)** conductivity. Source: [42].

Cameron et al. [43] reported 30 measurements of 23 freshly-excised ALNs from 14 patients, in the 0.5-20 GHz frequency range. Interestingly, for some of the analysed ALNs, measurements were done placing a probe both on the external surface of the node and on its cross-section (after slicing it). The results of that study showed wide-range variability of ALN dielectric properties. Fig. 3.3, reports the highest and the lowest dielectric properties (black lines) across the 30 measurements performed in [43]. Cameron *et al.* concluded that fat tissue tends to dominate the measurements when placing the probe in contact with the exterior of the node, indicating that the measured real part of relative permittivity in the

range of 1 to 10 (Fig. 2 in [43]) corresponded to predominantly fatty samples. Additionally, the authors noticed that the interior of ALNs had higher dielectric properties due to higher water content. Fig. 3.3 also shows the differences between inner (cross-section) and outer (surface) dielectric properties, for two nodes. Lastly, even though results were only presented for one sample, the authors noted that permittivity and conductivity consistently increased with tumor content.

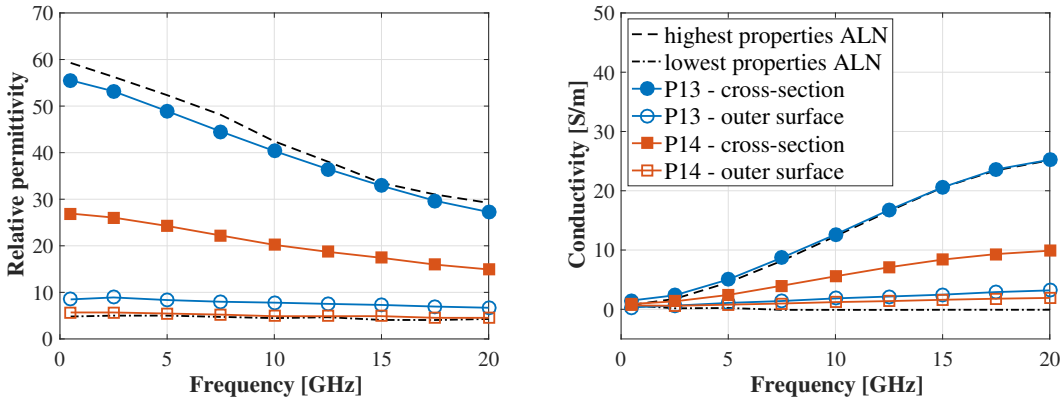

(a) (b)

Figure 3.3: Axillary Lymph Node (ALN) dielectric properties reported by Cameron *et al.* [43]. Black lines show the highest and lowest dielectric property measurements obtained across the 30 samples, indicating the great variability observed in the measurements. Coloured lines represent ALN dielectric properties measured from external and cross-section surfaces. Data refer to 2 samples from 2 patients (P13 and P14). The outer surface measurements correspond to 40% (P13) and 47% (P14) fat under the probe. The cross-sectional measurements correspond to 20% (P13) and 10% (P14) fat content under the probe, with lymphatic tissue becoming the predominant component. **(a)**: relative permittivity; **(b)** conductivity. Source [43].

Lu *et al.* [68; 69; 70] measured a total of 219 (178 healthy and 41 metastasised) thoracic LN samples, obtained from lung cancer surgeries of 76 patients. Applying the Mann-Whitney *U* test at single specific frequencies (64, 128, 298, 433 and 915 MHz, and 2.45GHz), the authors found significant differences (p-value < 0.05) between the dielectric properties

of metastasised and healthy LNs at all the analysed frequencies. Independent tests were performed for relative permittivity and conductivity.

Godinho *et al.* [33] developed a novel methodology which correlates voxel intensity in breast MRI with water-content of the tissues (and hence dielectric properties). The results indicated high variability of the dielectric properties of healthy ALNs (75 samples), with relative permittivity varying between 16.2 and 42.2 at 4.5 GHz. The results also showed the different composition of ALNs (proportion between cortex and hilum) influences the estimated properties. Additionally, based on the analysis of 25 samples, the authors suggested that the dielectric properties of metastasised ALNs are higher (relative permittivity between 41.3 and 50.6 at 4.5 GHz) and have less variability than those of healthy ALNs. An average dielectric contrast of 32% between healthy and metastasised ALNs was found at 4.5 GHz, which is a good indicator to pursue the development of ALN-MWI systems.

3.2 Development and assessment of a T_xOECP

The interpretation of the R_xOECP measurement of heterogeneous tissues is not trivial [52]. The penetration depth of the sensing volume is generally in the order of fractions of a millimeter [71], which is critical when the outer layer of the sample differs from the inner tissue. This is the case of ALNs, which, after their excision, are often surrounded by a variable amount of fat. The fat layer covering the ALN affects the estimated permittivity and tends to confound the measurement. In this context, it would be beneficial to have a sensing volume with greater penetration depth, which would be capable of retrieving average information of a specimen of an organ when is covered by a "confounding" layer.

Meaney et al. recently developed a T_xOECP method, which is intended for the measurement of vertebrae dielectric properties [45]. As detailed in Sec. 2.1, in this configuration, two OECPs are immersed inside the MUT facing each other. The probes work as

two "low-efficiency antennas", and the measured transmission coefficient (S_{21}) is used to analytically solve the complex permittivity of the MUT. Meaney's method is not directly applicable to the case of ALN dielectric measurement, for different reasons. Firstly, the analytical formulation proposed to de-embed dielectric properties assumes that the EM field reflections on the MUT-air interface are negligible. That hypothesis is not realistic in the case of ALN measurement due to the limited size of ALNs (ALN size ranges from 0.5cm to 2cm along their larger axis). Secondly, the method requires the measurement of the S_{21} at several separation distances, which would imply penetrating the tissue with the probes. This is not feasible in the case of ALN, which cannot be punctured, as required by clinicians.

This section presents a T$_x$OECP which is designed to measure relatively small size (few millimeters) heterogeneous samples. In particular, the aim is to develop a probe capable of an elongated sensing volume rather than a transversal field spread. Moreover, given the inapplicability of the analytical formulation proposed in [45], this section investigates an alternative approach to de-embed dielectric properties.

The following sections describe: the preliminary numerical tests used to investigate the feasibility of a T$_x$OECP (Sec. 3.2.1); the developed setup (Sec.3.2.2); the post-processing techniques to de-embed the dielectric properties of a MUT (Sec. 3.2.3). Finally, the final adopted measurement protocol is reported in Appendix A.

3.2.1 Numerical assessment of a T$_x$OECP

In order to investigate the feasibility of a T$_x$OECP, preliminary numerical tests were performed using several simplified T$_x$OECP setups designed in *CST Studio Suite* [72].

As a first test, the behavior of three T$_x$OECP designs was compared. The goal was to maximize the magnitude of the transmitted signal (S_{21}) through the sample, while focusing the EM-field towards the receiving probe (i.e., along the z-axis, as shown in Fig. 3.4a). As

represented on the left of Fig. 3.4, the three setups consist of two coaxial-probes "sandwiching" a cylindrical sample. Inspired by the configuration proposed in [45], one of the probes emits the RF signals, while the other records them. The RF energy propagates through the MUT, over a distance d, as shown in Fig. 3.4. The three T$_x$OECP setups differ in the design of their OECP cut-off sections (i.e., the tips of the probes which are in contact with the MUT). In detail, the following OECPs were tested:

- **probe (a):** *Cut flush* OECPs (Fig.3.4a).
- **probe (b):** *recessed* OECPs (Fig. 3.4b). In this configuration, the outer conductor was removed from the last segment (last 2mm) of the OECPs. This was done to enhance the transmission ability of the OECP. Indeed, shortening the outer conductor could make the emitting probe slightly radiative.
- **probe (c):** OECPs with metal flanges (Fig.3.4c). The rationale behind adding flanges was to create a cavity to keep the EM energy out of the cable, while minimizing the E-field dispersion outside the sample.

All the probes were $100mm$ long, with inner conductor radius $r_1 = 0.46mm$, insulator radius $r_2 = 1.49mm$, and outer conductor radius $r_3 = 1.79mm$. The conductive components of the probes were made of a "perfect electric conductor" (PEC); while the insulator was made of Polytetrafluoroethylene (PTFE), which has relative permittivity $\epsilon' = 2.1$ and loss tangent $tan(\delta) = 0.0002$.

For the three T$_x$OECP configurations, Fig. 3.5 reports the $|S_{21}|$ of a cylindrical material. The cylindrical MUT had radius $r = 5mm$, height $d = 5mm$, real part of permittivity $\epsilon'(\omega) = 55$, and conductivity $\sigma(\omega) = 0.1S/m$, constant in the 0.5-14 GHz frequency band. As as result, both the partial removal of the outer conductor (*recessed* OECP) and the application of flanges (OECP *with flanges*) increase the transmission capability of the T$_x$OECP. This is a promising result since larger $|S_{21}|$ may enhance the sensitivity of the

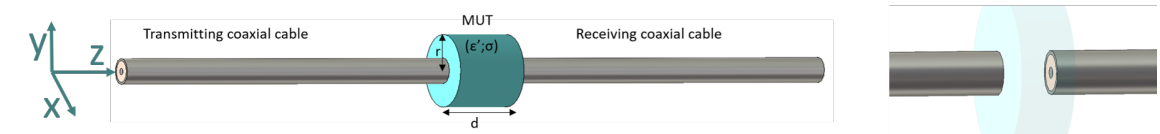

(a) *cut flush* T_xOECP

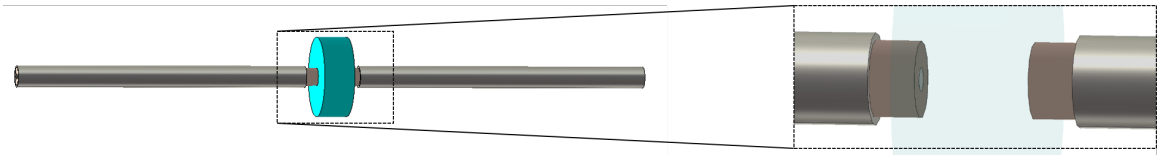

(b) *Recessed* T_xOECP

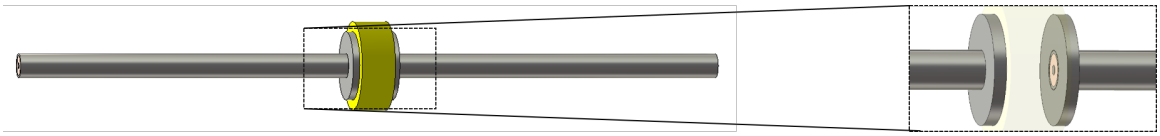

(c) T_xOECP *with flanges*

Figure 3.4: Design of the three transmission-based Open-Ended Coaxial-Probes (T_xOECP), tested in simulation: **(a)** *cut flush* T_xOECP; **(b)** *recessed* T_xOECP; **(c)** T_xOECP *with flanges*. In **(a)**, the tips of the coaxial probes were not modified. In **(b)**, the outer conductor was removed from the tips of the coaxial probes. In **(c)**, two metal flanges were placed at the tips of the coaxial probes. The detailed views of the probe tips are shown on the right.

method.

The E-field inside the MUT was also analysed aiming to assess how it would spread along the transversal direction over the entire volume of the sample. If the E-field spreads over a very large area along the xy-plane, the de-embedded permittivity will be affected by the properties of the entire volume of the sample. This is highly undesired since ALNs often occupy just a small portion of the excised sample (usually, the sample is composed of ALN and a layer of fat tissue). The E-field magnitude map at 6 GHz is reported in Fig. 3.6 for the three probes. The analysis of this plot leads to the following considerations:

- In Fig. 3.6a, the *cut flush* T_xOECP showed good results, as it was able to confine the E-field to a small volume of the sample.

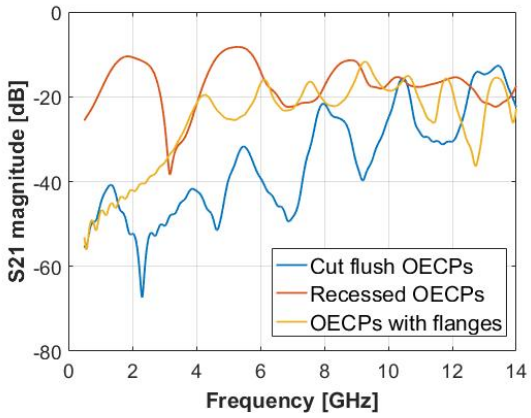

Figure 3.5: Magnitude of the transmission coefficient, S_{21}, for the three probe tip configurations under study. These results were obtained numerically using CST for a sample of size $r = 5mm$, separation distance $d = 5mm$, and relative permittivity $\epsilon' = 55$ and conductivity $\sigma = 1S/m$, constant in the analysed frequency band.

- In Fig. 3.6b, the E-field plot suggests that the *recessed* T$_x$OECP radiates out of the region of the sample, making this configuration unsuitable for the intended application;

- In Fig. 3.6c, the E-field plot suggests that the addition of the flanges causes a uniform spreading of the E-field over the volume of the sample, and aids the transmission towards the receiving probe. However, the spreading of the E-field over the xy-plane is undesired as it is likely that this will also involve the fat tissue surrounding the ALN, thus affecting the estimation of ALN dielectric proprieties. Ideally, the E-field should propagate along the z-axis, limiting as much as possible its spatial spreading on the xy-plane.

Similar behaviours were observed when testing higher frequencies and different MUT. For the sake of brevity, those results are not reported in this thesis.

Given the limitations presented by probe configurations (b) and (c), configuration (a) was adopted as it presented the best trade-off between transmitted power and sensing vol-

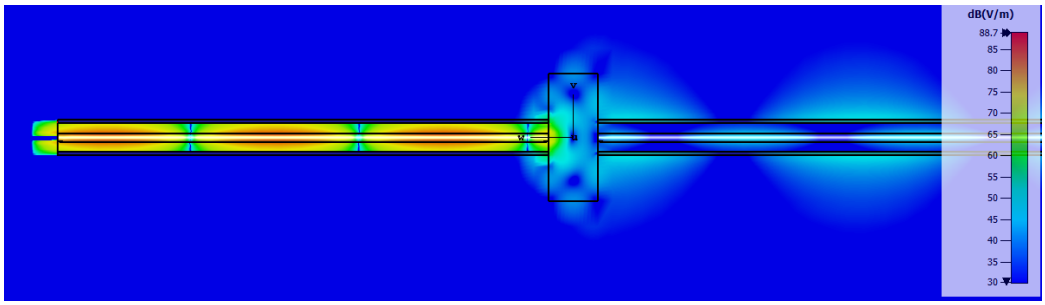

(a) *Cut flush* coaxial probes

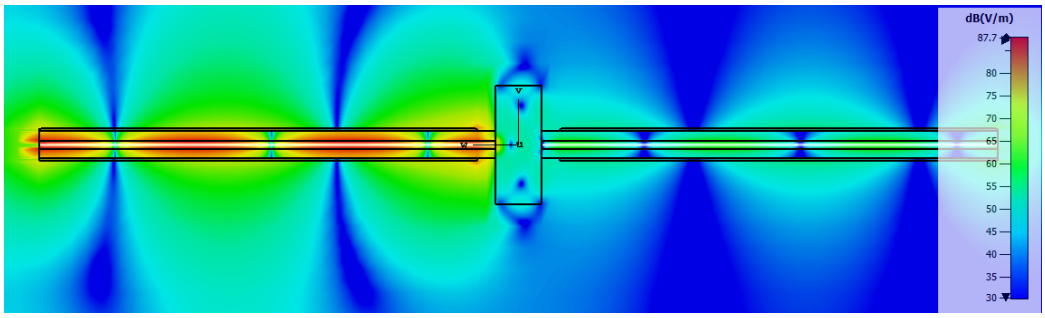

(b) *Recessed* coaxial probes

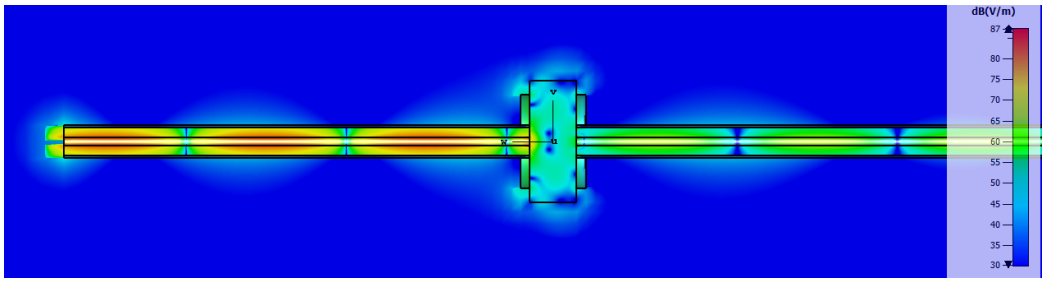

(c) Coaxial probes *with flanges*

Figure 3.6: Magnitude of the electric-field (at 6GHz) for all three tested configurations of the transmission-based open-ended coaxial-probe.

ume. Yet, some limitations regarding the z-dimension of the samples should be expected, since for large values of d, the signal-to-noise ratio may deteriorate significantly.

In order to validate the *cut flush* T$_x$OECP as the preferable measurement setup, the influence of the dielectric properties of the MUT on the transmitted power was further analysed, using probes configuration (a). Fig. 3.7 shows the magnitude of the E-field for several MUTs with varying dielectric properties. Such set of MUTs was selected as they

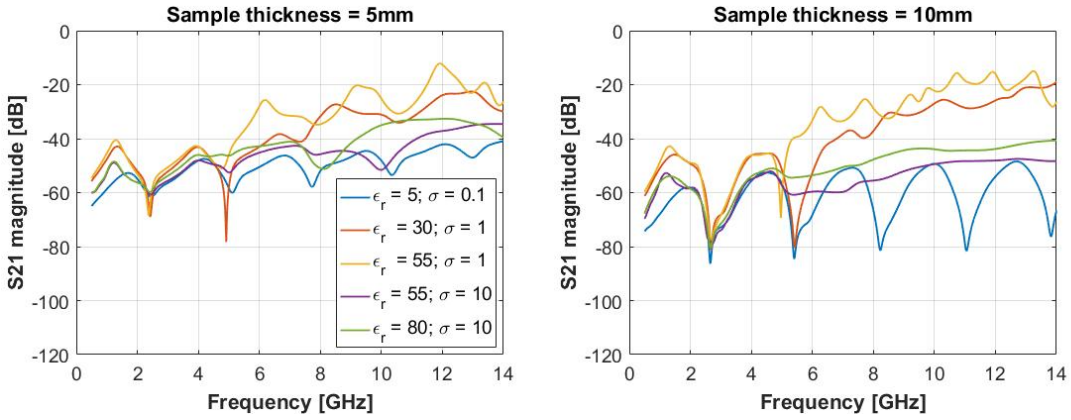

(a) (b)

Figure 3.7: Magnitude of the signals transmitted (S_{21}) through a cylindrical sample when using the *cut flush* T$_x$OECP (Fig. 3.4a). Different materials are considered (relative permittivity, ϵ_r, and conductivity, σ, in the legend). Sample radius: $r = 2.5mm$. Probe separation distance: in **(a)**, $d = 5mm$; in **(b)**, $d = 10mm$

represent the variability in the dielectric properties of biological tissue. The probe separation distance was chosen as $d = 5mm$ (Fig. 3.7a) and as $d = 10mm$ (Fig. 3.7b). The results show that, in the range of 0.5-14 GHz, for any considered dielectric property, the S_{21} is above -90 dB, in the case of the largest separation distance (i.e., $d = 10mm$). Considering a VNA dynamic range of 110dB, it can be concluded that the penetration depth of the *cut flush* T$_x$OECP is large enough to measure ALNs.

Finally, the influence of the radius of the MUT on the S_{21} was investigated. In other words, it was investigated if the S_{21} is affected by changes of the MUT size in the xy-plane. Fig. 3.8 shows the $|S_{21}|$ for several samples, with different radii (details on the MUT size and dielectric properties are reported). The results show that the size (and probably the shape) of the sample influences the S_{21} and has to be taken into account when de-embedding the dielectric properties of a given MUT.

In conclusion, the *cut flush* T$_x$OECP can transmit enough power through an ALN (S_{21} greater than the VNA dynamic range), while confining the EM-field to a limited region of

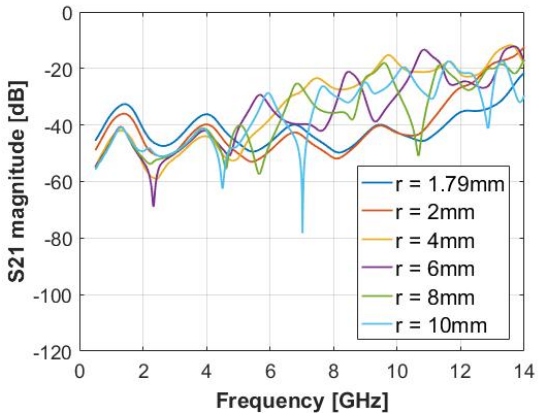

Figure 3.8: Magnitude of the signals transmitted (S_{21}) through a cylindrical sample when using the *cut flush* T$_x$OECP (Fig. 3.4a). The responses of different radii samples are compared. Shorter sample radius ($r = 1.79mm$) is equal to the coaxial probe radius; the larger radius ($r = 10mm$) corresponds to the maximum expected radius for ALN. Relative permittivity: $\epsilon' = 55$; conductivity: $\sigma = 1S/m$; Separation distance: $d = 5mm$.

the sample. However, de-embedding the dielectric properties of any MUT can be challenging due to the high number of variables (including the size of the sample) which affects the measurements. For this reason, during experiments, the size (and, when possible, the shape) of all samples was tracked.

3.2.2 Setup description

Based on the results discussed in Sec. 2.1, the setup was fabricated using the *cut flush* T$_x$OECP configuration. The final setup is illustrated in Fig. 3.9a and consists of the following parts:

- one VNA with 2 ports;
- two flexible coaxial-cables and adapters;
- two (semi-rigid) OECPs;

- one 3D-printed PolyLactic Acid (PLA) structure that served as (i) a holder for the OECPs and (ii) a support table for the MUT. This structure fixes one probe, and allows the other one to move on its z-axis, while ensuring the two probes are perfectly aligned.

- one caliper to measure the MUT thickness (i.e., distance d between the two probe tips).

For any measurement, the MUT was placed on the supporting table; the sliding part of the PLA support allowed to move one of the two OECPs and, therefore, to lightly squeeze the MUT between the two OECPs (Fig. 3.9b). The adopted measurement protocol is detailed in Appendix A.

3.2.3 De-embedding dielectric properties

The de-embedding of dielectric properties relies on an empirical comparison between experiments and simulations. The method is based on the hypothesis that an accurate representation of the experiments in simulation should give approximately the same output (same S_{21}) of the actual experiments. This approach is inspired by the study published in [73], which showed good agreement between experimental and numerical transmission coefficient when using a similar setup to de-embed the dielectric properties of liquids.

To validate the proposed methodology, experimental and numerical measurements were performed on two different phantoms with known dielectric properties and sizes. The measured phantoms were:

- One cuboid sample (25mm x 25mm x 1.77mm) made of acrylic;

- One cuboid phantom (19mm x 19mm x 1.62mm) made of the following mixture: 7.5% w/w graphite; 7% w/w Carbon Black, 85.5% w/w Polyurethane; and 4ml isopropanol per 100g of mixture.

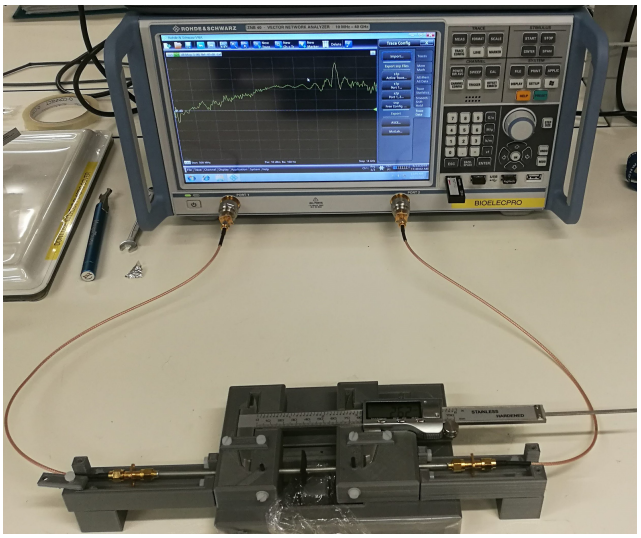

(a)

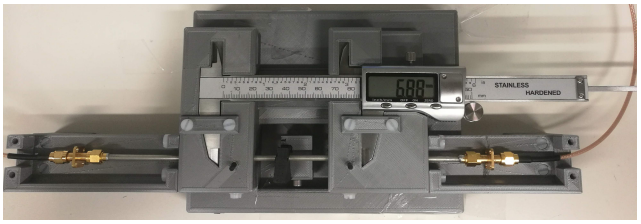

(b)

Figure 3.9: Experimental setup used for transmission-based dielectric measurements. In **(a)**, all the assembled components are present: the Vector Network Analyzer (VNA) is connected through the cables to the two Open-Ended Coaxial-Probes (OECPs), which are placed in the plastic support. In **(b)**, a closer view of the OECPs placed in the support is shown. A material is measured between the two OECPs.

The complex permittivities of the two materials were measured with the T$_x$OECP and are reported in Fig.3.10. Numerical and experimental results are compared in Fig. 3.11, indicating good agreement for both the acrylic (blue plots) and the mixture (red plots) cases. Moreover, a clear separation between the S_{21} of the two materials is observed (note the separation between the blue and red plots in Fig. 3.11). This result suggests that the transmission coefficient, measured with the T$_x$OECP, may be able to discriminate between dielectric properties of different materials.

As a final test, S_{21} acquisitions were performed (through simulation) on an heterogeneous sample. The sample is cuboid-shaped (19mm x 19mm x 1.62mm), composed of two layers (interface perpendicular to the z-axis), which respectively have the dielectric properties of the acrylic and of the above described mixture. Interestingly, the S_{21} of the heterogeneous sample falls between the two S_{21} of the two homogeneous samples, suggesting the need to complete further tests to assess the viability of this system to measure average dielectric properties of heterogeneous samples.

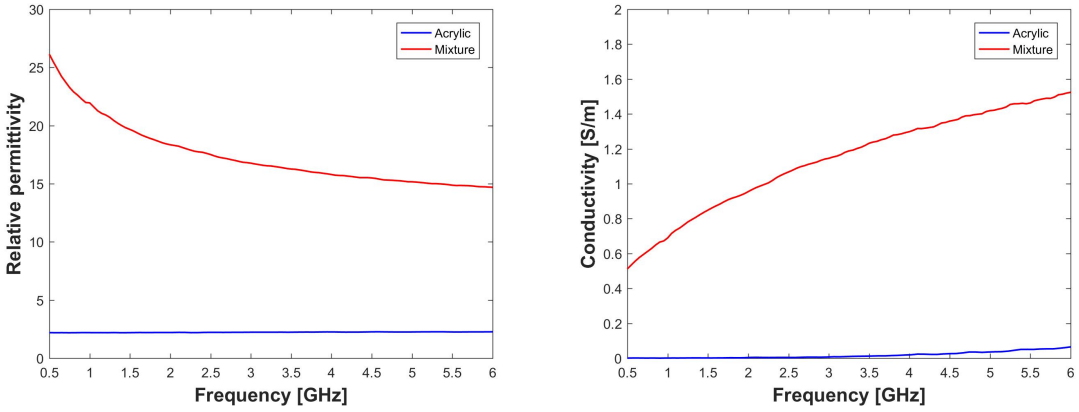

(a) (b)

Figure 3.10: Dielectric properties of the two materials measured with the T$_x$OECP: **(a)** real part of relative permittivity; **(b)** equivalent conductivity. These values were measured using the R$_x$OECP and served as a benchmark to assess the sensitivity of the T$_x$OECP technique.

3.3 Measurements of lymph node dielectric properties

This section describes the measurements that were performed on animal and human LNs at microwave frequencies, when applying the R$_x$OECP method. Firstly, dielectric measurement of human ALNs were performed (Section 3.3.2). However, due to tissue handling restrictions, the measurements were limited to the outer surface of the ALNs, allowing limited conclusions to be drawn. Consequently, the study was extended to animal LNs (Sec-

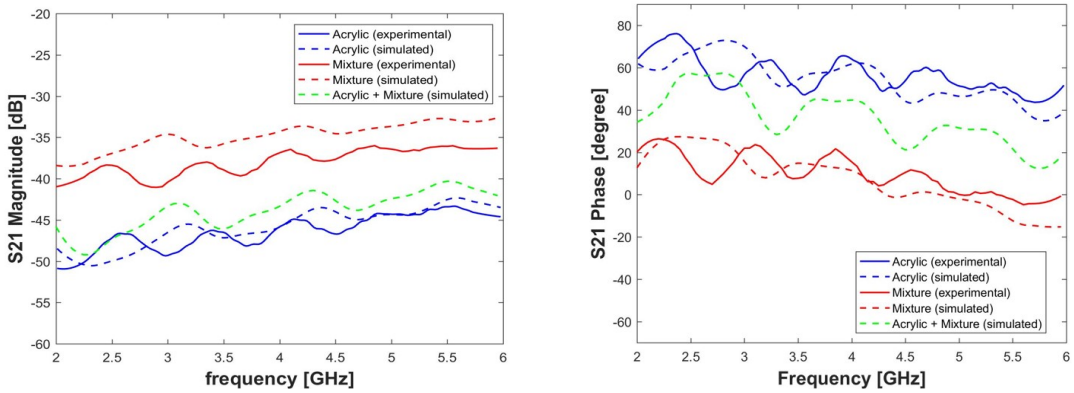

(a) (b)

Figure 3.11: Comparison between experimental (continuous line) and simulated (dashed line) S_{21} obtained when measuring two different permittivity samples. Sample dielectric properties are reported in Fig. 3.10. Propagation distance: d=1.77mm (acrylic case); d=1.62mm (mixture case): (a) Magnitude of transmission coefficient; (b) Phase (unwrapped) of transmission coefficient. Note: phases are plotted after average subtraction.

tion 3.3.3), which could be sliced to enable the measurement of their inner cross-section. Animal LN measurements helped interpret the measurements performed on human ALNs, which is a reasonable approximation as most of the tissue dielectric properties available in the literature [48] are the result of *ex-vivo* animal tissue dielectric measurements. It should also be noted that - despite having different sizes depending on animal species - animal and human LNs have the same anatomy and physiological function. Additionally, some studies in the literature [74; 75] compared human and animal tissues showing good consistency in dielectric properties.

3.3.1 Measurement procedure

The dielectric measurements were performed using the Keysight slim form probe connected to the Keysight E5063A Vector Network Analyser (VNA) through a right angle SMA-connector. With this procedure, the use of cables was avoided, hence excluding

a potential source of uncertainty [76]. The measurements covered the frequency bandwidth of 500 MHz - 8.5 GHz. Prior to measurements, the system was calibrated using the open/short/load method, as it is standard procedure [77]. Deionized water was used as a standard load. A picture of the measurement setup is reported in Fig. 3.12 a. The OECP

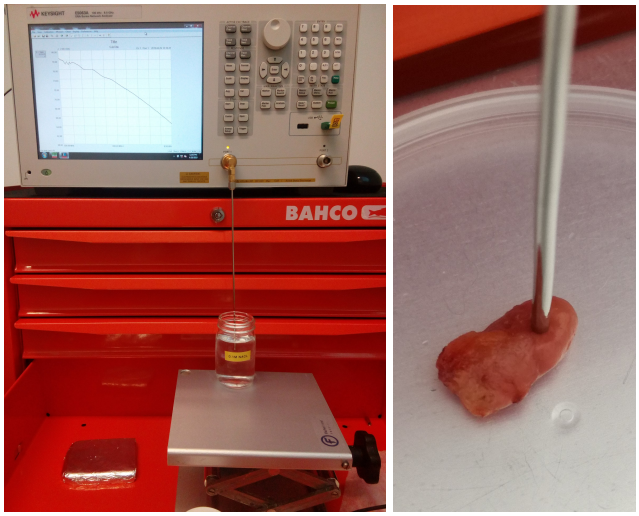

(a) (b)

Figure 3.12: (**a**) Dielectric measurement setup: the open-ended coaxial-probe is connected with a right angle SMA-connector to a vector network analyzer during the measurement of the validation load (0.1 Molar NaCl water solution). (**b**) Detail of a human axillary lymph node measurement.

measurement technique is very sensitive to VNA drift, as well as inappropriate handling of the probe [76; 78]. As a result, an additional measurement was performed to validate the calibration. This measurement was done with a 0.1 Molar Sodium Chloride (0.1M NaCl) solution - with complex permittivity documented in [79] over frequency and temperature - in order to estimate the error of the measurement setup at any given time during a measurement campaign. This validation procedure was firstly proposed in [76], and it is currently accepted by the scientific community to estimate the measurement error and to minimize the uncertainty inherent to measurements. In the present study, the validation measurement was performed immediately after setup calibration (V1, prior to tissue measurements) and

Table 3.1: Dielectric measurement validation: average difference [%], considering all measurement sessions, between the permittivity inferred from the validation measurements and the reference values. Data are separated between pre-measurement validation (V1) and post-measurement validation (V2). The left side of the table refers to human axillary lymph node (ALN) measurements, while the right side of the table refers to animal lymph node (LN) measurements.

	Human ALNs		**Animal LNs**	
	$\Delta\epsilon'$ [%]	$\Delta\sigma$ [%]	$\Delta\epsilon'$ [%]	$\Delta\sigma$ [%]
V1	1.06	2.09	0.93	2.93
V2	2.26	2.92	5.50	2.13

after some sample measurements (V2, usually within 90 min after the calibration). The temperature of the validation solution was recorded to match it to the correct model. When the error was above 10%, the probe calibration and its validation were repeated. Table 3.1 presents the average percentage error (over frequency and over all measurement sessions) of the validation measurements. The maximum average ($\pm$standard deviation) error was $5.50(\pm 2.13)\%$, which is acceptable for the purpose of tissue characterisation.

Regarding tissue measurement, it should be mentioned that the pressure applied with the probe on the tissue can affect the measured dielectric properties [80]; therefore, care was taken in applying approximately the same pressure on the samples. The pressure applied was the least pressure possible, while ensuring full contact between the tip of the probe and the measured tissue, as well as avoiding air gaps between the two.

The Minimum Information for Dielectric Measurements of Biological Tissues (MINDER), proposed in [81], was taken as a guideline to collect experimental data and associated metadata. MINDER specifications indicate a systematic collection of metadata along with dielectric measurement data, in order to support a more informed sharing and re-use of dielectric data. Since measurement confounders (e.g., calibration procedure, calibration drift, validation procedure) and clinical confounders (e.g., tissue origin, animal age and weight, time between excision and measurement, tissue handling procedures, tis-

sue temperature) can impact the measured data [76; 82; 83], reporting confounder-related metadata supports consistent, interpretable, and accurate dielectric data. The measured data and the related metadata will be made available in the MyWAVE open-access online repository [84].

3.3.2 Human axillary lymph node measurements

Eleven ALNs from 9 patients diagnosed with breast cancer were measured. Fig. 3.13 reports five of the human ALNs that were measured in this study. All ALNs were excised by a trained surgeon during SLNB scheduled at the University Hospital Galway (Galway, Ireland) [85] during April and May 2019.

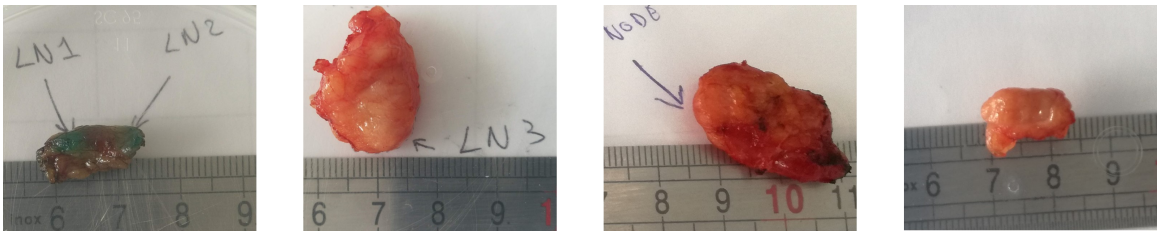

Figure 3.13: Examples of five human axillary lymph nodes (ALNs) measured in the present study. The sample shown in the first figure on the left contains two different ALNs, as indicated by the arrows.

After each ALN excision, the sample was brought to the lab for dielectric property measurement. The sample was measured immediately after receiving it, always within 20 minutes after excision. The temperature of the sample surface was measured at the same time as the dielectric measurement took place, resulting in an average ($\pm$ standard deviation) temperature of 20.9 °C ($\pm$ 2.3 °C). The size of ALNs ranged approximately from 5 mm to 2 cm on their longer axis, and approximately between 4 mm and 7 mm on their shorter axis. These values are greater than the sensing depth of the probe which has been estimated [52; 86] to vary between 2 and 3 mm. The surgeon removed as much fat as possible from the surroundings of the ALNs. It should also be reported that sometimes fat

could not be completely removed, due to the risk of cutting or puncturing the ALN, which would compromise the subsequent histopathological examination. However, the surgeons indicated the best measurement point (i.e., the point on the ALN surface that contained the least fat tissue). Between 3 to 5 points of each of the 11 ALNs (depending on the size of the ALN) were measured placing the probe in contact with the outer surface of the ALN. A total of 45 measurements from all ALNs was collected. The samples were then given to the pathologist for standard histopathological analysis. All the 11 ALNs were diagnosed as "negative", i.e., no tumor cells were found during the histopathological examination, which represents the main shortcoming of this study. Information from metastasised ALNs should be sought in future work. Yet, for the purpose of this thesis, the here acquired measurements are sufficient for phantom development. For each of the 11 ALNs, between 3 to 5 points (depending on the size of the ALN) were measured placing the probe in contact with the outer surface of the ALN. In total, 45 measurements from all ALNs were collected.

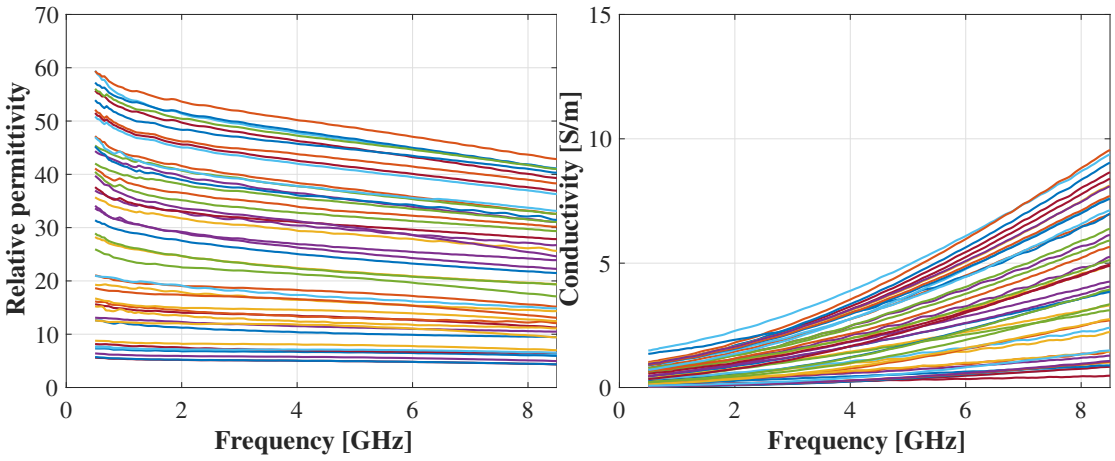

(a) (b)

Figure 3.14: **(a)** Relative permittivity and **(b)** conductivity resulting from 45 measurements conducted on 11 ALNs excised from 9 patients. Data refer to measurements on the outer surface of the ALNs.

Fig. 3.14 illustrates the dielectric properties of all the measured human ALNs. The re-

sults show very high variability of measured ALN dielectric properties, as the relative permittivity ranges from 5.0 to 49.5 and the conductivity from 0.3 S/m to 4.4 S/m at 4.5 GHz. These results are in line with those reported by Cameron *et al.* [43] (Fig. 3.3), confirming that the presence of fat on the outer surface of the ALN sample may have a major influence on the permittivity. Due to their high variability, definite conclusions about the permittivity of the content of ALNs cannot be drawn. However, in order to allow the interpretation of the results, data were separated into three different groups, defined as follows:

- $Group_{1-10}$ included measurements where $\epsilon_r(4.5\ \mathrm{GHz}) \leq 10$;
- $Group_{10-40}$ included measurements where $10 < \epsilon_r(4.5\ \mathrm{GHz}) \leq 40$;
- $Group_{40+}$ included measurements where $\epsilon_r(4.5\ \mathrm{GHz}) > 40$.

The lowest values of relative permittivity (i.e., $\epsilon_r < 10$) are a consequence of the presence of a fat layer on the surface of the ALNs and are not of interest to this study. From the remaining values, it may be concluded that ALNs do have permittivity higher than the fatty content that embeds them, indicating that their detection is possible at microwave frequencies. Furthermore, it should be noted that the ALNs, for which the surgeon was able to remove the largest amount of fat from the surface, corresponded to the measurement of the highest permittivity values ($\epsilon_r > 40$ at 4.5 GHz) and showed high consistency across intra-sample measurements. Considering that consistency is a valid indicator of tissue homogeneity, this suggests that $Group_{40+}$ dielectric values effectively correspond to the dielectric properties of the ALN under test.

Lastly, for $Group_{10-40}$ and $Group_{40+}$, the mean permittivity was fitted to a two-pole Debye model using the Least Squares Method (LSM) [87] to minimise the fitting error, which is a widely-adopted approach to retrieve the 2-pole Debye model parameters [61]. The parameters are reported in Table 3.2. The fitting error, defined as the mean absolute difference (over frequency), between the average measured data and model, was at maximum

Table 3.2: Two-pole Debye parameters fitted to the mean permittivity computed on three different groups of data. The first two rows refer to human axillary lymph node data, divided into two different groups, according to their relative permittivity values. The third row refers to all the data acquired when measuring the inner content of sheep lymph nodes.

	ϵ_∞	σ_s [S/m]	$\Delta\epsilon_1$	τ_1 [s]	$\Delta\epsilon_2$	τ_2 [s]
ALN $Group_{10-40}$	1.0	1.00	34.2	$0.7e^{-9}$	16.2	$1.4e^{-11}$
ALN $Group_{40+}$	1.0	1.2	119.4	$1.0e^{-9}$	38.3	$1.0e^{-11}$
Animal LN (inner content)	9.4	0.04	212.0	$1.7e^{-9}$	46.0	$1.12e^{-11}$

0.4 regarding relative permittivity and 0.1 S/m regarding conductivity, which is negligible for MWI applications.

The high variability observed in the inter-sample analysis (Fig. 3.14) was also observed in the intra-sample analysis. Fig. 3.15 reports the dielectric properties of several points measured on a single ALN (e.g. ALN 1, shown in Fig 3.15a). The high variability of the complex permittivity can be justified by the significant amount of surrounding fat. Indeed, as reported in [52], the dielectric properties of heterogeneous tissues depend on the spatial distribution of each material (ALN and fat in this case) within the sensing volume.

Conversely, Fig. 3.16 shows a case where surgeons were able to better separate the excised ALN (ALN 2 in Fig. 3.16a) from the surrounding fat. In that case, the dielectric properties are more consistent across all the measurement sites, which is a valid indicator of tissue homogeneity. The greater homogeneity of the tissue, together with the higher dielectric properties measured, suggests that the results associated with ALN 2 effectively correspond to the dielectric properties of the node under test.

For the sake of completeness, the results of the dielectric measurements performed on each of the analysed ALN are reported in Appendix B (Fig. B.1).

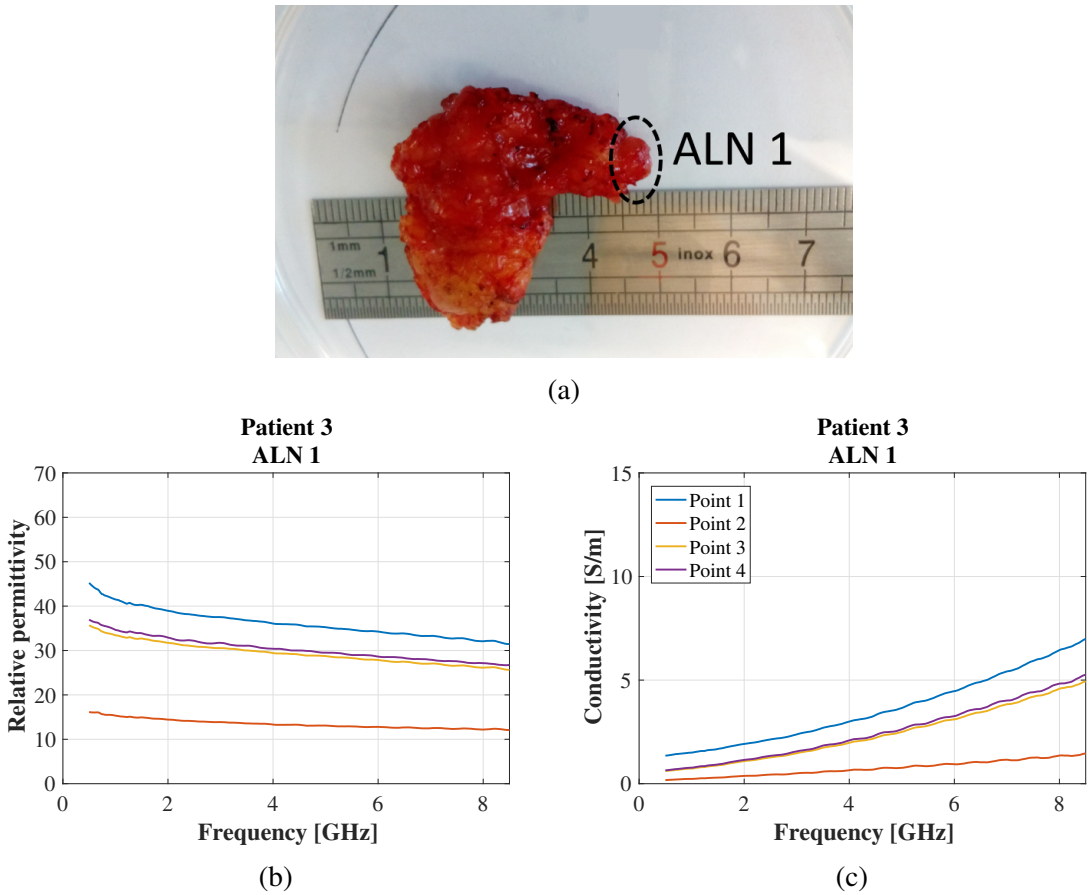

(a) (b) (c)

Figure 3.15: Example of dielectric measurements of a single axillary lymph node (ALN 1). **(a)** picture of the sample (the ALN is circled with a dashed line); **(b)** ALN 1 relative permittivity. **(c)** ALN 1 conductivity. Each line corresponds to a measurement site.

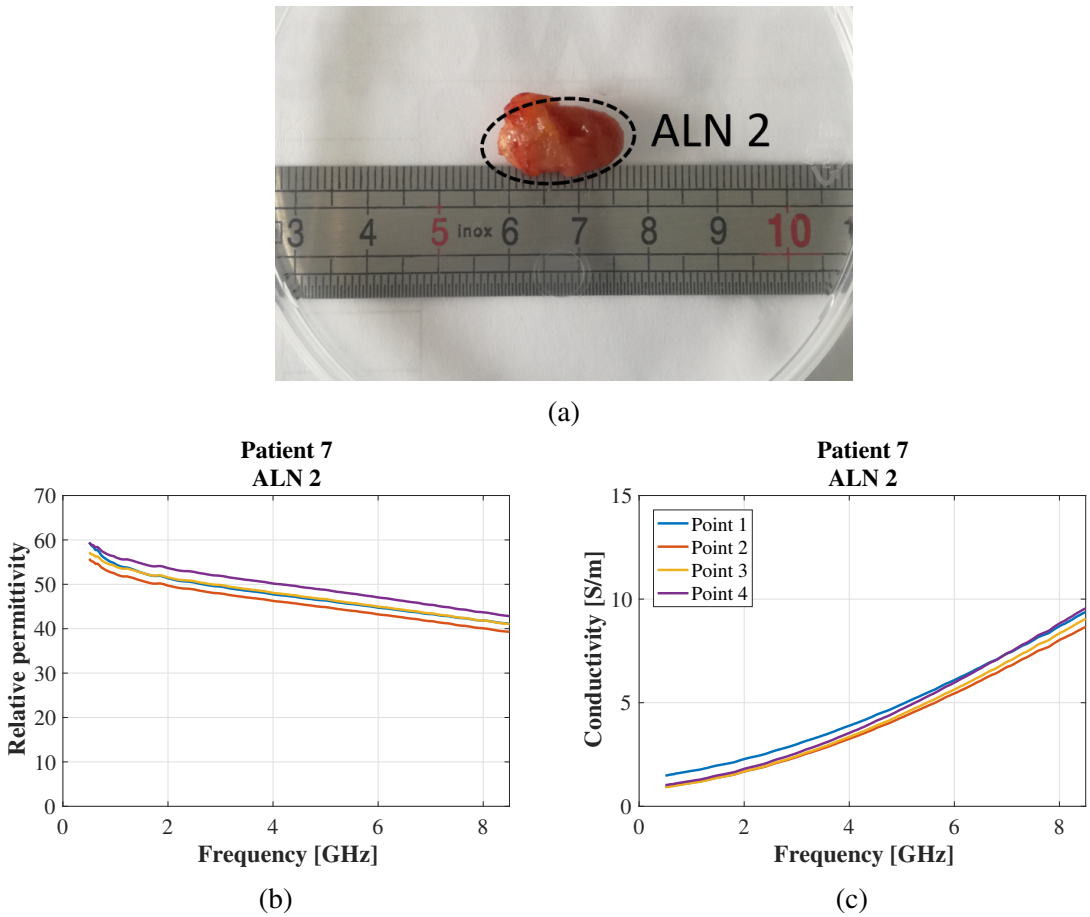

(a) (b) (c)

Figure 3.16: Example of dielectric measurements of a single axillary lymph node (ALN 2). **(a)** picture of the sample (the ALN is circled with a dashed line); **(b)** ALN 2 relative permittivity. **(c)** ALN 2 conductivity. Each line corresponds to a measurement site.

3.3.3 Animal lymph node measurements

To overcome the tissue handling limitations of human ALNs, which affect measurements, animal LNs were measured. *Ex-vivo* animal tissues do not imply handling constraints, such as with human tissues. This allowed collection of data from their inner cross-section and obtain more reliable results.

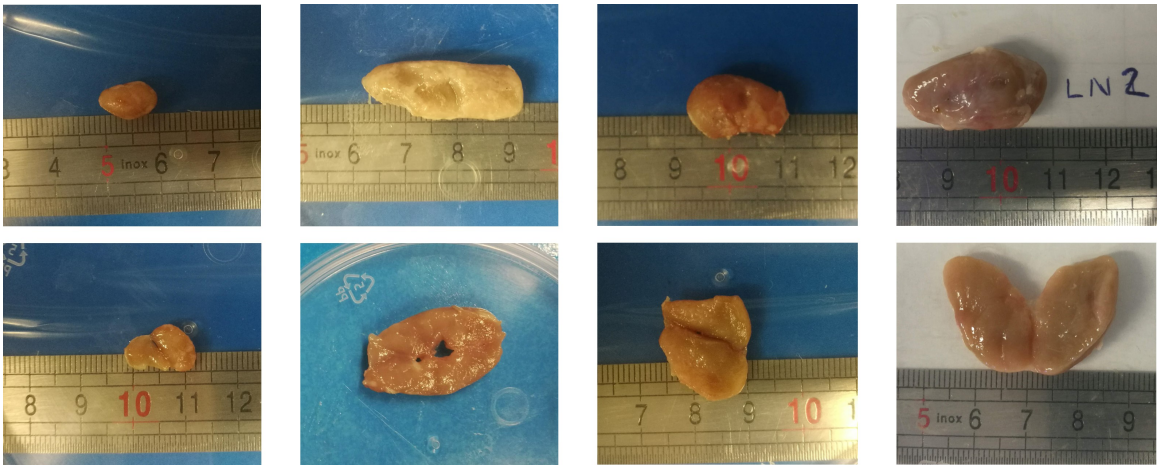

Figure 3.17: Example of four ewe inguinal lymph nodes that were measured. (**Top line**) intact ewe LNs; (**bottom line**) same LNs, sliced in half.

For the purpose of this study, 8 LNs from 2 sheep corpses were measured. The animals were healthy ewes of mass of approximately 70 kg of about 6 years old. The LNs were excised by a trained veterinary surgeon from the inguinal area, approximately 3 to 4 hours after the death of the animal. The surgeon removed as much fat as possible with a scalpel, avoiding puncturing the LN capsule (i.e., a thin layer of connective tissue covering the node [4]). It should be noted that, since there were no handling nor ethical constraints, more fat was removed from around the animal LNs compared to human ALNs. The samples were then placed in a closed container in order to minimise tissue dehydration. No preservatives or additives were used as these could impact the dielectric measurements. Measurements were performed within 20 minutes to 4 hours after tissue excision. It is recognised that,

despite placing the samples in a closed container, tissue outer surface dehydration may have occurred and may have impacted outer surface dielectric measurements.

Firstly, the outer surface of LNs was measured for a direct comparison with human ALNs. The 8 samples were measured in 4 to 6 locations depending on the size of the LN, in a total of 41 measurements, while trying to avoid measurements near regions with residual fat. The average ($\pm$ standard deviation) temperature of the LN surface was 20.6 °C ($\pm$ 1.3 °C). The relative permittivity and conductivity are reported in Fig. 3.18. The maximum permittivity (ϵ_r around 50 at 4.5 GHz) and conductivity (σ around 5 S/m at 4.5 GHz) values are similar to those observed in the case of $Group_{40+}$ of human ALNs (Fig. 3.14). Additionally, similarly to the case of human ALNs, there is a significant variability between measurements which is likely to be due to the presence of residual fat.

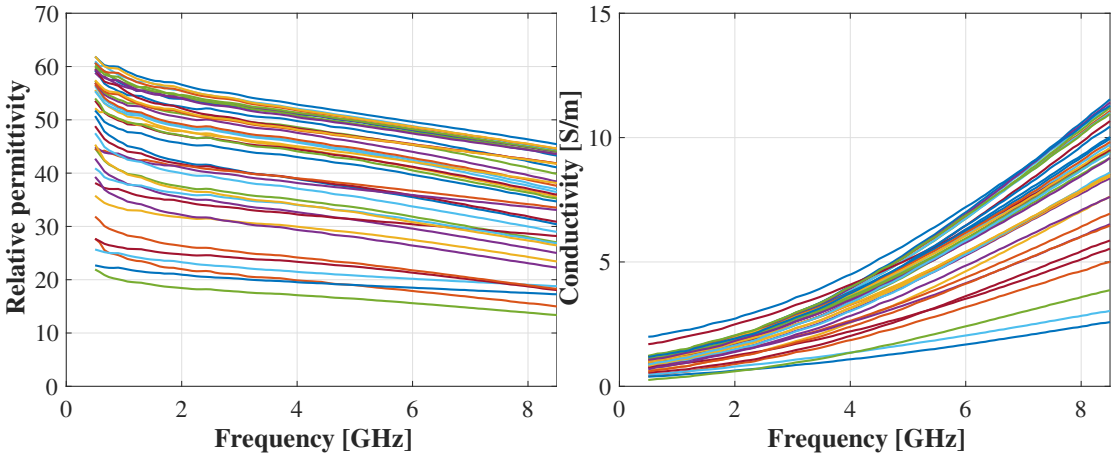

Figure 3.18: Dielectric measurements of sheep inguinal LN external surfaces. **(a)** Relative permittivity and **(b)** conductivity resulted from 41 measurements conducted on 8 LNs excised from 2 sheep.

For each LN, immediately after the outer surface measurement, the LN sample was sliced in half and, straightaway, the probe was placed in contact with the LN cross-section surface. It is emphasized that, in the case of cross-section measurements, the dielectric

properties are expected to be more stable over time, as this area is less exposed to air (therefore less prone to dehydration) than the outer surface [88]. Fig. 3.17 (bottom-line) illustrates 4 ewe LNs after being sliced in half. Again, measurements were taken in 4 to 6 locations for each LN, in a total of 40 measurements. The average ($\pm$ standard deviation) temperature of the sample cross-section surface was 21.8 °C ($\pm$ 0.9 °C). Figure 3.19 shows the permittivity obtained from the cross-section of the animal LNs.

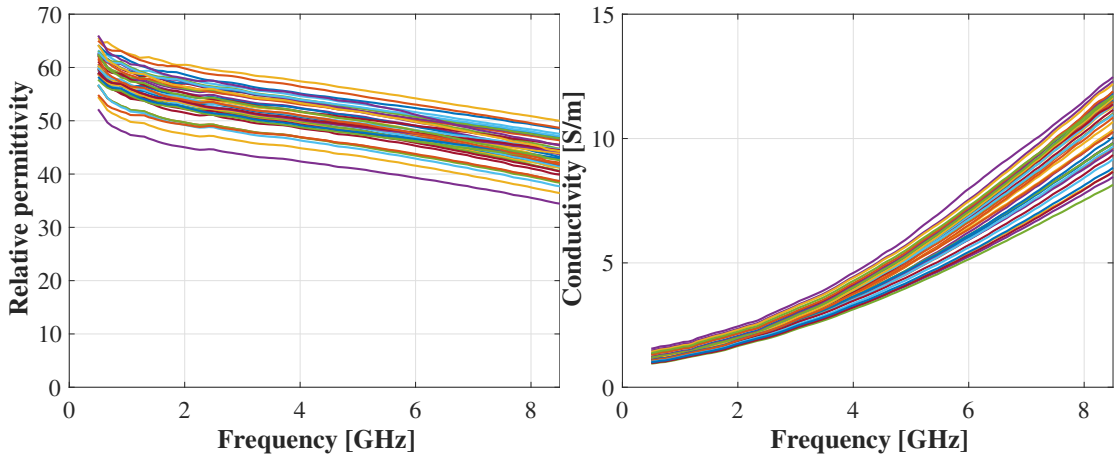

(a) (b)

Figure 3.19: Dielectric measurements on sheep inguinal LN internal cross-section. **(a)** Relative permittivity and **(b)** conductivity resulted from 40 measurements conducted on 8 LNs excised from 2 sheep.

In contrast to the permittivity measured on the LN surface, measurements in the inner cross-section are consistent with each other due to the homogeneity observed in the interior of LNs. Relative permittivity ranges between 41.7 and 56.7 at 4.5 GHz, while conductivity ranges between 3.6 and 5.3 S/m at the same frequency. These values are similar to the highest permittivity values obtained from the surface measurements of both human ALNs and ewe LNs (see Fig. 3.14 and Fig. 3.18, respectively). Such high permittivity values are probably due to the very high water-content of the tissue, which is compatible with the physiological function of the organ [1].

[1]The inner part of ALNs contains lymph and plasma cells, which have high water-content.

The mean permittivity of all the cross-section measurements was fitted to a two-pole Debye model, following the same procedure described in Sec. 3.3.2. The obtained Debye models' parameters are reported in Table 3.2. The absolute fitting error was at maximum 0.3 in relative permittivity and 0.1 S/m in conductivity, demonstrating that the model is a good representation of the measured data.

Lastly, it should be reported that similarly to the inter-sample analysis, also the intra-sample analysis shows high consistency and higher dielectric properties in the cross-section measurements. Fig. 3.20 reports the dielectric properties of several points measured on a single sheep LN. A similar behaviour is observed for all the remaining measured 7 LNs, which are reported in Appendix B (Fig. B.2).

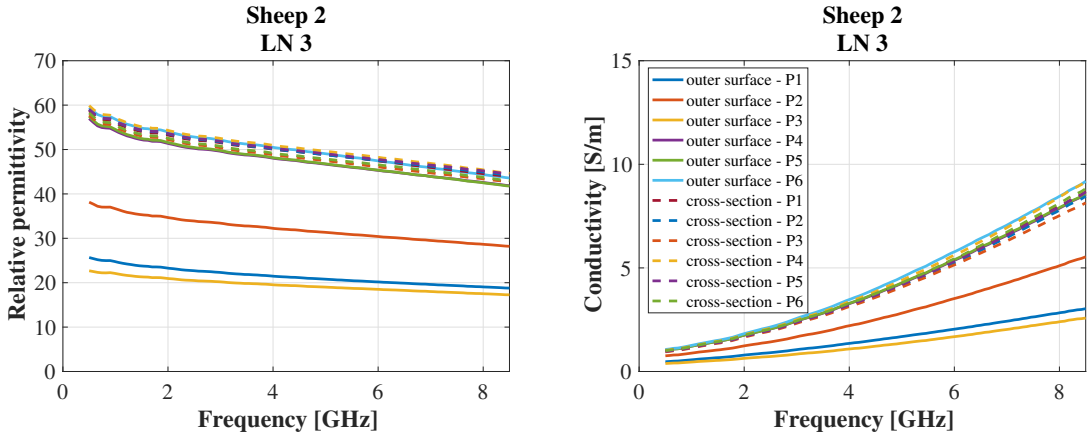

(a) (b)

Figure 3.20: Dielectric measurements on a single sheep inguinal LN: a comparison between outer surface (continuous line) and cross-section (dashed line) measurements. Each line corresponds to a measurement point. **(a)** Relative permittivity and **(b)** conductivity.

3.4 Freezing and defrosting effects on complex permittivity of biological tissues

In order to complement the knowledge on ALN dielectric properties, our research group measured LNs excised from dead animals (cats and dogs) which may have been diagnosed with mammary cancer (outside the scope of this thesis). This work was conducted in collaboration with the Instituto Nacional de Investigacão Agrária e Veterinária (INIAV), Oeiras, Portugal [89], where our group measured LNs of animals - *post-mortem* - that had been previously frozen and defrosted ahead of their autopsy. Therefore, it is important to study whether the freezing and defrosting process can impact the dielectric properties of biological tissue, which is still unknown in the literature. In fact, only very limited number of studies have addressed this subject.

Bengtsson et al. [90] investigated the effect of the freezing process on the dielectric properties of codfish and beef minced meat. In that study, minced meat samples were prepared and frozen at -30 ºC. Samples were defrosted for dielectric measurement after 1-2 days, after 1-2 weeks, and after 1-3 months. Dielectric measurements were taken at two different frequencies (35 MHz and 100 MHz), at two different temperatures, namely -10 ºC and +2 ºC. The authors found no significant effect of frozen storage time for fish dielectric properties, but there was a significant difference for beef at -10 ºC, where both dielectric constant and loss tangent decreased with prolonged frozen storage.

Bodakian et al. [91] studied the changes of chicken (White Rock; aged 3 to 4 months) muscle dielectric properties after freezing storage, using dielectric spectroscopy over the range of 5 Hz – 1 MHz. The researchers divided a chicken breast in two halves: the first one was measured two hours after the animal was slaughtered, while the second one was frozen for four hours, defrosted, and measured. Both samples were measured at 6 ºC. The author noticed that the conductivity substantially increased (approximately 100% increment

- corresponding to 0.3 S/m circa - at 1 KHz) by the freezing and defrosting process.

Ley et al. [92] suggested that the storage time (up to 55 hours) in a commercial fridge does not influence the dielectric properties of porcine liver, muscle, fat, and blood in the frequency range between 0.5 and 7 GHz.

The first two studies did not investigate the frequency range of interest to MWI applications; while the third investigated the influence of the storage time at temperatures above 0 ºC, at which water molecules do not freeze. Hence, in order to enable dielectric measurements on frozen and defrosted ALNs, the gap observed in the literature should first be bridged. To do so, the effect of freezing and defrosting chicken muscle, bovine liver, and bovine fat on their complex permittivity was investigated. Also, the effect of frozen storage time on permittivity was investigated. The study focuses on the 0.5 - 8.5 GHz frequency band, which comprises the frequencies that will be used in ALN-MWI; and it considers frozen storage times up to 14 days, which can be considered a reasonable time for researchers to organise a measurement campaign.

The remainder of the section is as follows: Sec. 3.4.1 illustrates the experimental methodology and evaluation metrics; and Sec. 3.4.2 presents and discusses the results.

3.4.1 Methodology and experimental setup

This section describes the selection and preparation of tissue samples, the methodology, and the experimental setup adopted during the experiments. Sec. 3.4.1.1 illustrates the sample preparation and the experimental plan; Sec. 3.4.1.2 describes the instrumentation, and the measurement technique, including the validation of the measurements; Sec. 3.4.1.3 reports the evaluation metric and the statistical hypotheses tests designed for this investigation.

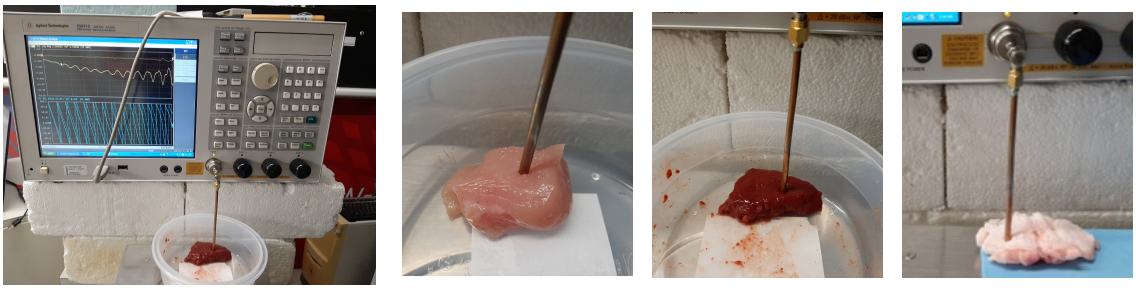

(a) (b) (c) (d)

Figure 3.21: **(a)** Dielectric measurement setup: the open-ended coaxial-probe is connected to a right angle SMA-connector, and a vector network analyzer during a tissue measurement. **(b-d)** Details of three tissue measurements: **(b)** chicken muscle; **(c)** bovine liver; **(d)** bovine fat.

3.4.1.1 Sample preparation and experimental plan

The study was conducted on chicken muscle (one animal specimen), bovine liver (one animal specimen), and bovine fat tissues (two animal specimens). These tissues were chosen due to their homogeneity, thus minimizing the influence of sample heterogeneity, as it acts as a confounder [78]. Additionally, these tissues present relative permittivity of about 4 (fat), 40 (liver), and 50 (muscle) at 4.5 GHz, thus covering a large range of biological tissue properties.

Fresh animal tissues were purchased from a local butcher, less than 24 hours after slaughter. After the time of death, tissues were stored in a fridge (at approximately 5 ºC), and measurement started within 48 hours *post mortem*.

On the first day of measurements (day 0), 10 samples (size approximately 3 x 2 x 1 cm^3) were sliced from each of the 3 tissue types, in a total of 30 samples, which were measured using the OECP technique. It should be noted that the size of the samples is sufficiently large, both with respect to sensing radius and to sensing depth of the probe, according to [52; 86]. Samples were measured once they reached room temperature. The surface temperature of each sample was recorded with an infrared thermometer at the time

Table 3.3: **Column (1, 2)** Measured average temperature of the three tissues under study at day 0, $T_s(0)$, and day d, $T_s(d)$. **Column (3)** average absolute difference, $|\Delta T_s(d)|$.

tissue	$T_s(0)$ [ºC] avg ($\pm$ std)	$T_s(d)$ [ºC] avg ($\pm$ std)	$\|\Delta T_s(d)\|$ [ºC] avg ($\pm$ std)
muscle	20.7($\pm$0.6)	21.3($\pm$1.4)	0.8($\pm$0.9)
liver	20.9($\pm$0.2)	21.8($\pm$0.5)	1.0($\pm$0.5)
fat	20.7($\pm$1.1)	21.9($\pm$1.6)	1.1($\pm$0.8)

of measurement. Within 7 hours after the beginning of the measurements, the samples were wrapped in cling film and stored in a sealed container at a temperature of approximately -18 ºC.

At each subsequent day, one sample of each tissue type was defrosted, and its dielectric properties were measured at approximately the same spot where they had been measured on day 0. Samples were defrosted at room temperature, and measured once they reached the temperature of the measurements on day 0, which is crucial for a fair comparison between dielectric properties in day 0 and day d. After this final measurement, each sample was discarded. For simplicity, the subscript d will be used in the following text to refer to the number of days each sample was frozen for, where d ranges between 1 and 14.

Table 3.3 reports the average ($\pm$ standard deviation) of $|\Delta T_s(d)| = |T_s(d) - T_s(0)|$ for each tissue type, where $T_s(d)$ and $T_s(0)$ are the measured temperatures of sample s on days d and 0, respectively. The average $|\Delta T_s(d)|$ is approximately 1 ºC, which is acceptable, as it has been reported that dielectric properties do not vary more than 2% per Celsius degree [93]. For reproducibility purposes, Table 3.3 also reports the average ($\pm$ standard deviation) $T_s(d)$ and $T_s(0)$, for each tissue type.

3.4.1.2 Instrumentation and measurement technique

Dielectric measurements were performed using an OECP fabricated with an EZ-141 coaxial cable (outer diameter of 3.58 mm). The probe was connected to the vector network analyzer (VNA) with a right angle SMA-connector (Fig. 3.21a), in order to eliminate the uncertainty introduced by the use of cables [76]. Measurements were performed in 801 equally spaced frequency points between 500 MHz and 8.5 GHz. The adopted retrieval algorithm was proposed in [51], which entails calibrating the probe measuring a short-circuit, an open-circuit, and a known load. Deionized water was used as a known load; its average ($\pm$ standard deviation) temperature was 21.7 ($\pm$0.4) ºC.

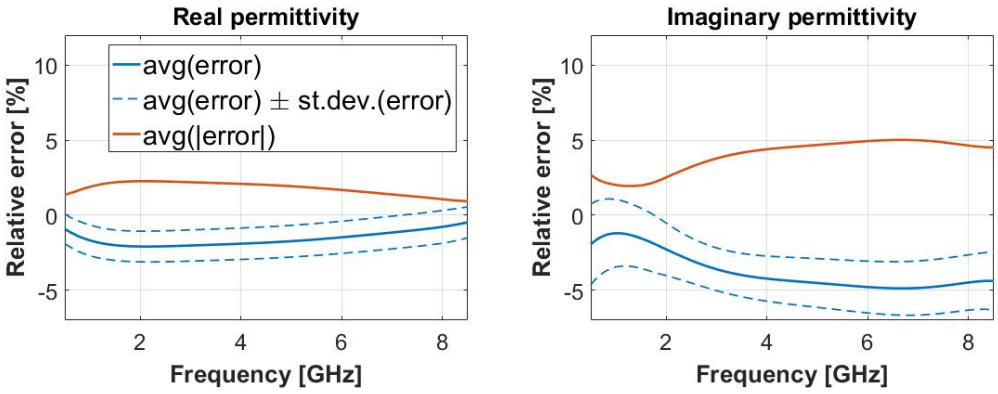

(a) (b)

Figure 3.22: Dielectric measurement uncertainty: average ($\pm$standard deviation) relative error (blue), and average absolute value of the relative error (orange), across all 99 validation measurements. The relative error is computed as the relative [%] difference between the measured and the model (reported in [79]) complex permittivity of the 0.1M NaCl solution. **(a)** Real part, and **(b)** imaginary part of permittivity.

Given the well-known sensitivity of the OECP system to VNA drift and to probe movements [76; 78], the so-called "validation measurements" was performed in order to estimate the error introduced by the measurement setup at any given time during the measurement campaign, as proposed in [76]. The validation measurement was conducted with a 0.1M NaCl solution. Its complex permittivity is documented in [79] over frequency and tempera-

ture. The validation measurement was performed immediately after setup calibration (prior to tissue measurements) and after some sample measurements (usually after each sample measurement or within 15 minutes since the last validation measurement), resulting in a total of 99 validation measurements. The temperature of the 0.1M NaCl solution was also recorded in order to match it to the correct model. The average ($\pm$ standard deviation) temperature of the 0.1M NaCl solution was 22.5 ($\pm$0.5) ºC. Fig. 3.22 reports the average ($\pm$ standard deviation) relative error, and the average absolute value of the relative error, across all validation measurements.

Regarding tissue measurement, in order to cope with intra-sample dielectric properties variability, between 3 to 7 points (one measurement from each point) were measured on the surface of each sample. It is known that the pressure applied with the probe onto the tissue [78; 80] can affect the measured dielectric properties (acting as a "confounder"). As a result, the least pressure possible was applied, while ensuring (i) full contact between the tip of the probe and the measured tissue, and (ii) that there were no air gaps between the probe and the sample. Fig. 3.21(b-d) shows examples of muscle, liver and fat tissue samples while being measured.

3.4.1.3 Evaluation metric and statistical tests

The complex permittivity variation is computed as $\Delta\epsilon'_s(f,d)$ (real part) and $\Delta\epsilon''_s(f,d)$ (imaginary part) as follows:

$$\Delta\epsilon'_s(f,d) = \epsilon'_s(f,d) - \epsilon'_s(f,0) \tag{3.1a}$$

$$\Delta\epsilon''_s(f,d) = \epsilon''_s(f,d) - \epsilon''_s(f,0) \tag{3.1b}$$

where $\epsilon'_s(f,d)$ and $\epsilon'_s(f,0)$ are the de-embedded real part of permittivity of sample s, at frequency f, measured on days d and 0, respectively. A similar metric is used to compute

the variation of the imaginary part of permittivity $\Delta\epsilon_s''(f,d)$.

Finally, the following two hypotheses were investigated:

- Hypothesis 1 (H1): the dielectric properties of defrosted tissues do not correlate with frozen storage time. To evaluate H1, the trend of $\Delta\epsilon_s'(f,d)$ and $\Delta\epsilon_s''(f,d)$ over d is analysed by fitting the data with a linear regression model (slope m). The p-value for m is computed to evaluate its statistical significance, choosing a significance level $\alpha = 0.05$.

- Hypothesis 2 (H2): the process of freezing and defrosting does not significantly affect the dielectric properties of biological tissues, with respect to fresh tissues. To evaluate H2, two sets of paired data are defined: (i) the dielectric properties measured on day 0, and (ii) the dielectric properties measured in the following days (d). For each tissue type, each of the two datasets comprises a total of 10 measurements. The Wilcoxon signed-ranked test (suited for paired samples with non-normally distributed differences) is used to assess whether the two sets of data significantly differ. It should be noted that the investigation of H2 does not take variable d into account, hence this is only possible if H1 is accepted. The sample size (N) was calculated so that the Wilcoxon signed-ranked test could detect, with power[1] 0.8 and significance level $\alpha = 0.05$ (commonly adopted in the literature [94]), a minimum difference of approximately 2-3 in the real part, and 0.8-1.2 in the imaginary part of the permittivity for muscle and liver, and a minimum difference of approximately 1.5 (real part), and 0.4 (imaginary part) in fat tissue. It should be reported that the Effect Size (E) corresponding to the above indicated differences was estimated ≥ 1 (E was defined as per [95; 96]). As a result, it was observed that N = 10 samples was sufficient to assess the sought differences.

[1]Statistical power is defined as $1 - \beta$; β is the TypeII error rate [94].

3.4.2 Results and discussion

This section presents the complex permittivity results and discusses its variability with the freezing process over time. Fig. 3.23 shows the day 0 complex permittivity results of the 3 tissues analysed. The whisker bars in Fig. 3.23 represent the inter-sample variability which is kept below 5% for the three tissues. This is an important indicator of the consistency of the measurements, as it allows to compare the dielectric properties variation measured on different samples. Also, it should be emphasized that the measured dielectric properties are similar to those reported in [97] (for bovine liver), [98] (for chicken muscle), and [83] (for freshly excised human breast fat).

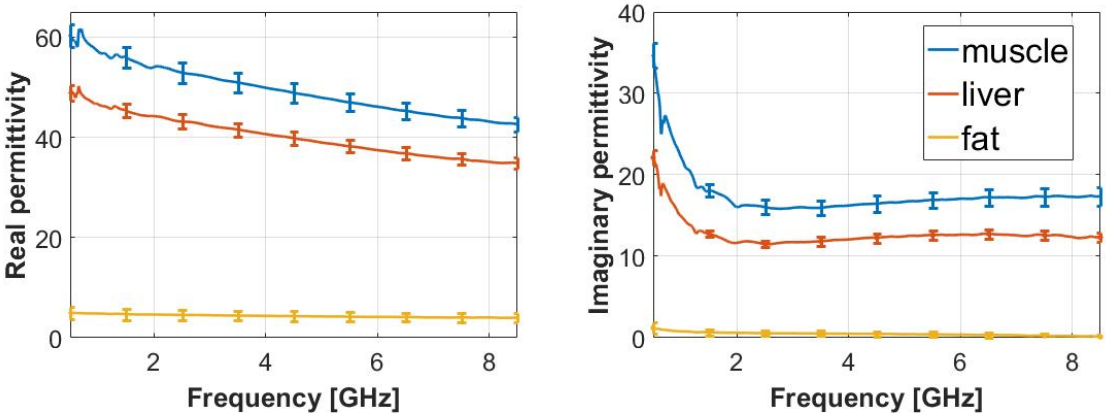

(a) (b)

Figure 3.23: Day 0 average dielectric properties of the three tissues analysed: **(a)** Real part, and **(b)** Imaginary part. The results are obtained by averaging the dielectric properties measured on all the 10 measured samples for each tissue. The standard deviation across the 10 samples is reported with 1 GHz intervals via a whisker plot.

3.4.2.1 Investigation of the dependency of frozen storage time (H1)

Fig. 3.24 reports $\Delta\epsilon'_s(f,d)$ and $\Delta\epsilon''_s(f,d)$, at $f = 2.5, 4.5, 6.5GHz$ over d, computed for all tissues. The graphs are fitted with a linear regression; the slopes m are reported in Fig.3.24. The slope of the linear regression fitted to $\Delta\epsilon'_s(f,d)$ and $\Delta\epsilon''_s(f,d)$ indicates only marginal

increase of the dielectric constant with the increase of frozen storage time d. Additionally, the p-values, also presented in Fig. 3.24, estimated for the slopes (m), are below 0.9 for all the reported cases, indicating that there is no sufficient evidence that a non-zero correlation exists between dielectric properties variation and frozen storage time.

It can be concluded that the dielectric properties of the defrosted tissues do not significantly depend on the frozen storage time (for frozen storage times within 14 days). As such, H2 may be investigated while ignoring any dependency on variable d.

3.4.2.2 Investigation of effect of freezing and defrosting (H2)

Based on the results discussed in Section 3.4.2.1, H2 can be investigated. Fig. 3.25 illustrates $\Delta\epsilon_s'(f)$ and $\Delta\epsilon_s''(f)$, at $f = 2.5,\ 4.5,\ 6.5\,GHz$, in a box-plot. At the centre frequency of $f = 4.5\,GHz$, after the tissue is frozen and defrosted, the real part of permittivity difference increases in the range between +0.8 (first quartile, Q1) and +2.0 (third quartile, Q3) in the case of chicken muscle (which corresponds to a percentage variation between 1.2% and 3.4%); while it varies within Q1 = 0.4 (2.6%) and Q3 = 1.3 (7.7%), in the imaginary part. For bovine liver, the real part varies within Q1 = -0.7 (-1.7%) and Q3 = +1.4 (+3.6%), while the imaginary part varies within Q1 = +0.7 (+5.6%) and Q3 = +1.3 (+10.3%) As for bovine fat, the median real part of permittivity decreases by -0.3 (-7.6%); while the median imaginary part decreases by -0.02, which can be considered negligible. It should be noted that the imaginary part of permittivity exhibits a larger percentage increase than the real part, which can be partially explained by the fact that the imaginary part is more susceptible to error associated to the OECP technique. In order to assess the significance of the observed differences, the Wilcoxon signed-ranked test was used (it was first verified that $\Delta\epsilon_s'(f)$ and $\Delta\epsilon_s''(f)$ do not follow a Normal distribution by applying the Kolmogorov-Smirnov test). The statistical powers, computed *post-hoc*, are reported in Fig. 3.25 for each test.

Significant differences (p-value ≤ 0.05) were found for muscle (both real and imaginary

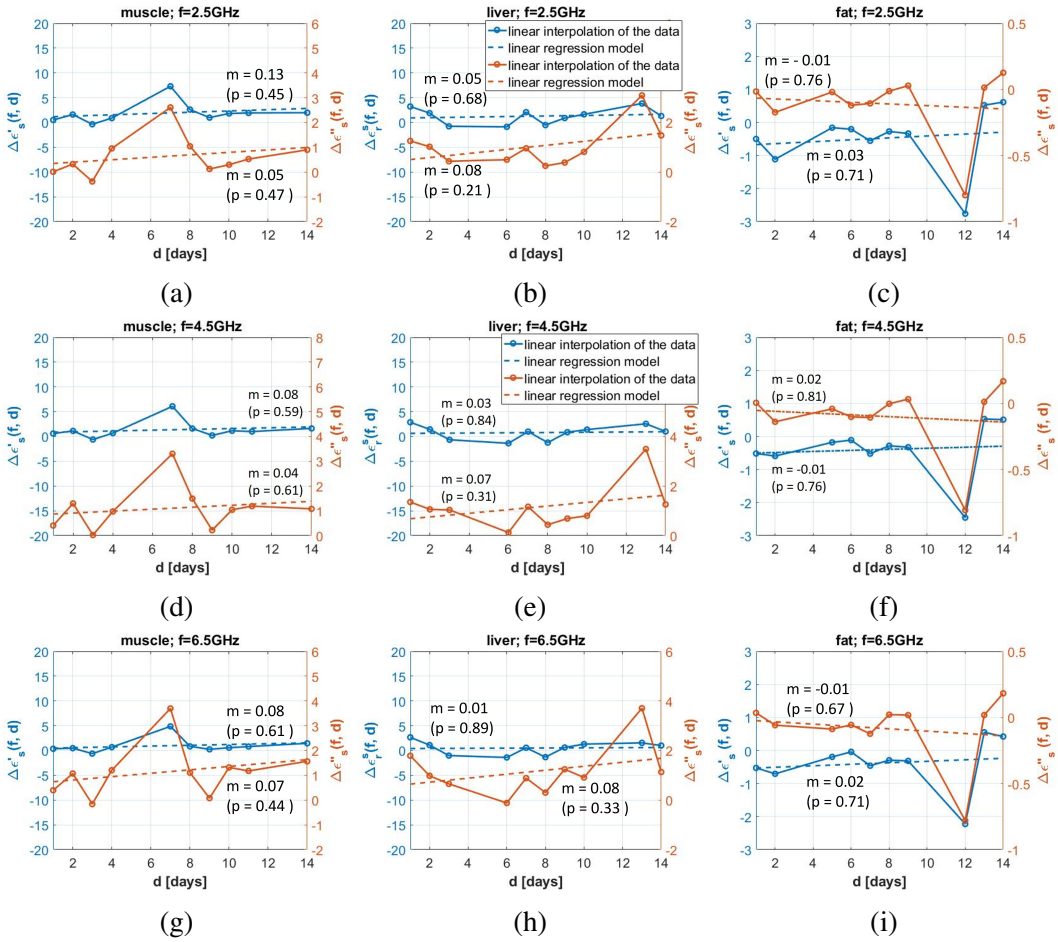

Figure 3.24: Investigation of H1: dielectric properties variation, $\Delta\epsilon'_s(f,d)$ and $\Delta\epsilon''_s(f,d)$, *vs* frozen storage time d, at 2.5, 4.5 and 6.5 GHz. **(a)** muscle, **(b)** liver, and **(c)** fat. Note that each sampling point univocally corresponds to one tissue sample (measured repeatedly both on day 0 and day d). The figure also reports the linear regression models, fitted for each case. The models are defined as $\widehat{\Delta\epsilon'_s}(f,d) = m*d+m_0$, where m is the slope, and m_0 is the vertical intercept. Above each graph, m and the corresponding p-value (in brackets) are reported. (A similar definition holds for $\widehat{\Delta\epsilon''_s}(f,d)$).

parts), for liver imaginary part, and for liver real part at 2.5GHz, as marked by the stars in Fig. 3.25. Regarding the cases where significant differences were not found, it should be emphasized that it may be due to the low power (< 0.8) of the corresponding tests (the observed effect size is considerably lower than the one estimated *a-priori*). This implies

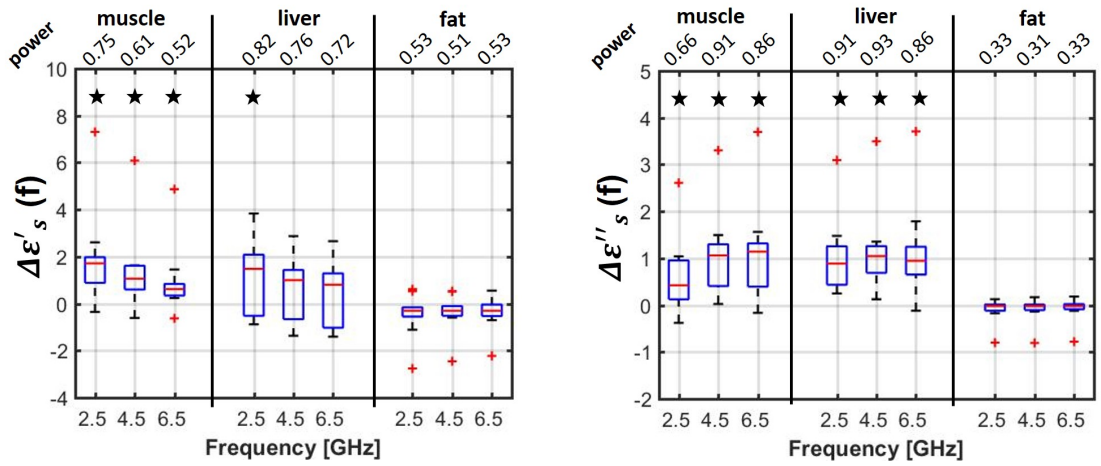

(a) (b)

Figure 3.25: Investigation of H2: distribution (box-plots) of $\Delta\epsilon'_s(f)$ and $\Delta\epsilon''_s(f)$, for each tissue, at 2.5, 4.5, and 6.5 GHz. Red line: median; bottom and top edges of the box: lower and upper quartiles respectively; black whiskers: maximum and minimum values excluding outliers; '+' symbol: outliers (i.e., values that are 1.5 times more than the interquartile range away from the edge of the box). The stars above indicate significant differences according to the Wilcoxon signed-ranked test. The power of the test is computed *post-hoc* and presented at the top.

that if differences existed, their value would be below the threshold that was defined as meaningful. As a result, investigating the significance of such small differences with higher power is not of interest for most of the applications referred above.

The results indicate that the characterization of dielectric properties of biological tissues can be performed on previously frozen low-water-content tissues. Regarding high-water-content tissues, defrosted samples may be used for the estimation of the complex permittivity if one can accept a slight overestimation of the properties, depending on the purpose of the study.

3.5 Conclusions

This chapter addressed the problem of ALN dielectric measurements with three parallel approaches.

First, the feasibility of a transmission-based setup using two open-ended coaxial probes was assessed for the estimation of dielectric properties of biological tissues. Contrarily to the traditional reflection-based coaxial probe, the proposed setup provides deeper sensing volume while keeping acceptable transmitted power, which makes it suitable for measuring heterogeneous tissues such as ALNs.

The transmission coefficient magnitude and electric field spread over the MUT was studied for three probe configurations. It was concluded that the *cut flush* OECPs best fit the requirements of the sensing volume and transmitted power. The setup was fabricated and used to measure two samples with different relative permittivity values. The experimental results showed acceptable match with numerical results, which is quite promising regarding the feasibility of the technique.

The second part of the work consisted in applying the state-of-the-art method for ALNs dielectric measurements. Even if no statistical evidence was carried out, the results indicated an approximation of the dielectric properties of ALNs. For instance, the relative permittivity of healthy ALNs is in the range of 30 to 50 at 4GHz. This is possible since consistency across measurements sites is a valid indicator of the homogeneity of the tissue being measured. Additionally, low dielectric properties are an indicator that fat is present in the sample. Given the limited availability of metastasised ALNs, it was not possible to investigate differences between healthy and pathological ALNs, which is recognized as the main limitation of this study.

The third part of the work consisted in studying the effect of freezing and defrosting processes on biological tissues dielectric properties. This study was motivated by the fact that our research group conducted measurements on previously frozen LNs to complement

the partial conclusions that were drawn after measuring freshly excised tissues. The effect of the freezing and defrosting processes on the dielectric properties of biological tissues was investigated in the 0.5-8.5 GHz frequency band, by measuring chicken muscle, bovine liver and bovine fat (relative permittivity ranging between 4 and 50 at 4.5 GHz), using the OECP technique.

Firstly, the dependency of electrical properties on frozen storage time (up to 14 days) was assessed. The results showed that there is no significant dependency on the frozen storage time. In other words, once the samples are frozen, they may be preserved for at least 14 days without a significant impact on the dielectric properties.

Secondly, the variation of complex permittivity with freezing/defrosting processes was investigated. For high water content tissues, the real part of permittivity (median value at 4.5 GHz) increased by 2.1% and 2.6% for muscle and liver respectively, while the imaginary part of permittivity increased by 6.4% and 8.9%. Regarding fat tissue, the observed variations were -0.3 and -0.02 (median value at 4.5 GHz) in the real and imaginary parts respectively, which are negligible for most applications.

It was concluded that frozen samples may be suitable for high water content tissues (which is the case for LNs) measurements if one accepts a slight overestimation of the properties. Such knowledge will be particularly useful in light of the measurement campaign on defrosted LNs from cats and dogs. Finally, it should be emphasized how important it is to report metadata regarding how samples are prepared and preserved, and hope other researchers will be encouraged to do so.

Chapter 4

Development of an anthropomorphic phantom of the axillary region

A critical step to assess the viability of a MWI device is to test it by means of numerical simulations and experiments on anthropomorphic phantoms. Numerical and physical anthropomorphic phantoms allow researchers to assess the system performance in a controlled and realistic environment.

For proper evaluation of MWI technology, the phantom should (i) be representative of the body anatomy, in terms of morphology and the tissues considered, and (ii) accurately mimic the dielectric properties of the tissues of interest. Additionally, it is useful to make the phantom (iii) re-configurable, so that organ dielectric properties, shape, and position can be adjusted to mimic physiological variability of tissue dielectric properties or morphology among individuals. Lastly, (iv) it is useful to make the shape and the dielectric properties of the physical phantom stable over time, to enable repeatable measurements.

Several authors proposed various alternatives to model anatomical regions for MWI applications. Examples include breast [99; 100; 101; 102; 103; 104; 105; 106; 107; 108], and head phantoms [108; 109; 110]. However, outside our research group, no one has yet

developed an anthropomorphic phantom of the axillary region suitable for MWI evaluation.

This chapter describes the development of an anthropomorphic phantom of the axillary region, suitable for the experimental assessment of MWI for ALN screening. To this end, (Sec.4.1) a thoracic CT scan was segmented and five tissues of interest were identified for realistic representation of the underarm region, given the intended application: fat, muscle, bone, lung, and ALNs. Tissue tissue mimicking materials (TMMs) were then fabricated (Sec.4.2) using the dielectric properties found in the literature [48; 111], and those measured in Sec. 3.3. Liquid TMMs were fabricated and used to fill 3D-printed hollow containers representing fat, muscle, and lung tissues. Solid TMMs were fabricated to mimic the bone, and the ALN tissues. Lastly, (Sec. 4.3) the influence of the polymeric containers on the electric field (E-field) coupled to the phantom was quantified through full-wave simulations. This is an important validation to confirm the 3D-printed phantom is representative of the real axillary region. This is the first realistic phantom of the axillary region for MWI to be proposed for experimental assessment.

The development of the phantom was conducted in collaboration with the Laboratoire de Génie Electrique et Electronique de Paris, at the Sorbonne University (Paris, France), which I visited for two months in the period of October-December 2019, as a planned secondment within EMERALD.

The work developed in the present chapter was published in the following journal paper:

- Savazzi M., Abedi S., Istuk N., Joachimowicz N., Roussel H., Porter E., O'Halloran M., Costa J. R., Fernandes C., Felício J. M., & Conceição R. C. "Development of an Anthropomorphic Phantom of the Axillary Region for Microwave Imaging Assessment". Sensors, vol. 20, no. 17, pp. 49–68, 2020. https://doi.org/10.3390/s20174968

4.1 Axillary phantom design and development

In order to enable access to the axillary region for imaging, the patient arm should be extended along the head, as shown in Fig. 4.1. This positioning allows the antennas to illuminate the axillary region from multiple perspectives, thus maximizing the scattering information that can be collected from the ALNs. The proposed positioning of the patient has significant impact on the phantom development, and this was considered when choosing the reference CT scan to build the phantom.

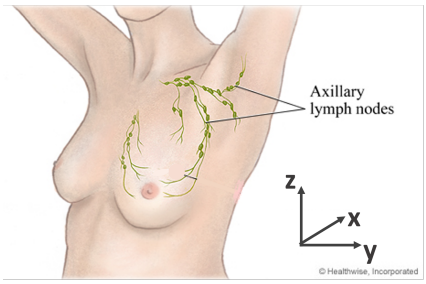

(a)

Figure 4.1: Patient positioning during the axillary region scan. Axillary lymph nodes can be properly illuminated when the patient's arm is extended along the head.

The phantom was developed based on a thoracic CT of a woman who had been diagnosed with breast cancer and was undergoing treatment at the Champalimaud Foundation [112] (Lisbon, Portugal). The CT image was provided by Dr. Durval Costa at Champalimaud Foundation, in compliance with the protocol "MMWave" (approved on 17 October 2018). The patient was 68 years-old, 154 cm tall, and weighed 50 Kg (body mass index[1], BMI = 21.1 kg/m^2).

During the acquisition, the patient was in a supine position, with her arms extended

[1]The body mass index (BMI) of a person is computed as the ratio between his/her weight [Kg] and squared height [m^2]. Commonly accepted BMI ranges are: underweight (under 18.5 kg/m^2), normal weight (18.5 to 24.9 kg/m^2), overweight (25 to 30 kg/m^2), and obese (over 30 kg/m^2) [113].

along the head, which is the standard position for CT breast cancer imaging. Note that such posture meets the model requirements. Also, the CT images provide high and uniform contrast in all the body region, thus enabling accurate segmentation of the tissues.

The CT consists of several transversal planes (i.e., xy-planes in Fig. 4.1). The overall resolution of the scan is 1.17mm x 1.17mm x 2mm in a total of 512 x 512 x 130 voxels. The size of the Region Of Interest (ROI) was limited to a volume of 145mm x 145mm x 180mm, in order to be able to print it with the 3D-printer (Form3, Formlabs [114]) available in our lab. It should be noted that the selection of such a restricted volume does not compromise the application, because the ALN region (i.e., the sub-region where the ALNs are located) extends only for approximately 5 cm below the skin level. Fig. 4.2 (a) shows one axial plane of the CT scan, where the segmented ROI is highlighted. Each colour within the ROI represents a different tissue. There are five tissues of interest, which were subsequently segmented from the CT scan: fat, muscles, bones, lung, and skin.

The segmentation was performed with the aid of 3D Slicer 4.10.2, a free open-source software platform for biomedical imaging research [115; 116], which is widely used in medical additive manufacturing. In order to segment the tissues of interest, a threshold on the voxel Hounsfield unit (HU) was applied, as common practice for segmentation in medical additive manufacturing [117]. For each tissue, the optimal threshold values (upper and lower HU bounds) were manually chosen to allow an accurate segmentation of each organ. It should be noticed that, as reported in [118], the use of manual threshold selection, though subjective, has been proved to be a reliable method for accurate segmentation. The choice of the threshold is relevant, in order to prevent gaps in surfaces (i.e., discontinuities) or structures that are split into separate volumes, which have to be joined ahead of 3D-printing.

After thresholding, morphological closing filtering (with a 3x3x3 voxel cubic structuring-element) was applied to each segment to fill small holes that resulted from the segmentation while preserving the shape of the segments. The remaining holes were then manually filled.

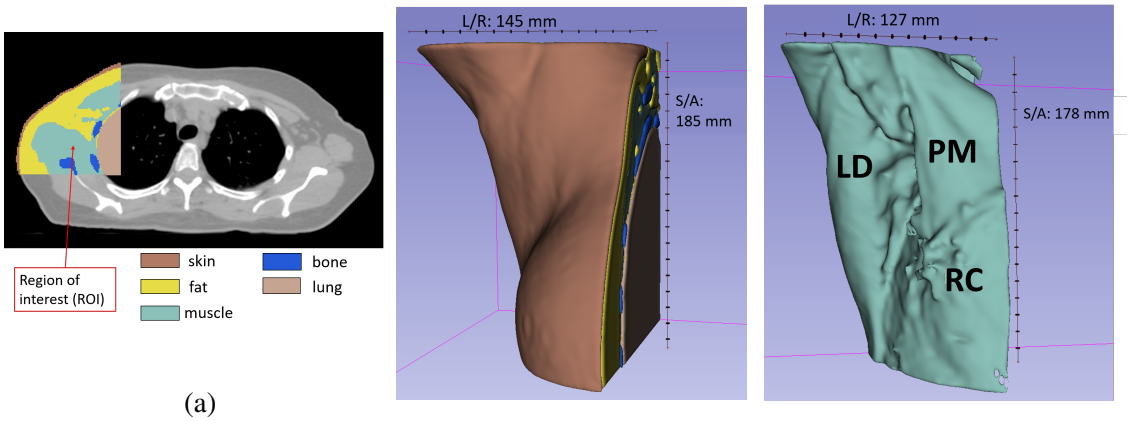

(a) (b) (c)

Figure 4.2: In **(a)**, image of the axial view of the body (XY-plane in Fig. 4.1) at the level of the sternum: the segmented organs are shown on top of the original CT. Each tissue is represented by a different color as detailed in the legend. The red arrow points at the segmented region of interest. In **(b)**, 3D-rendering view in 3D-slicer of the segmented organs. In **(c)**, 3D-rendering view in 3D-slicer of the segmented muscle tissue. Different muscles of the region are indicated: pectoralis major (PM), latissimum dorsi (LD), and rib-cage (RC) muscle. The pectoralis minor (i.e., the fourth muscle belonging to the axillary region) is not visible due to the frontal perspective of the figure. Superior/Anterior (S/A) and Left/Right (L/R) dimensions of the model are reported.

For example, the pulmonary bronchi and alveoli were segmented together with the region of the lung tissue, even though their HU did not originally correspond to the adopted lung HU range. Fig. 4.2 (b) shows the final 3D-rendering of the segmented volume. Fig. 4.2 (c) illustrates the segmented muscle tissue, where different muscle can be identified: pectoralis major, latissimum dorsi, and rib-cage muscle. It should be noted that the pectoralis minor (i.e., the fourth muscle belonging to the axillary region) is not visible due to the frontal perspective of the figure.

The numerical model obtained from the CT presented intricate morphological details due to the intrinsic complexity of the anatomical structures. This can be critical as the representation of fine morphological details can lead to excessive polymer presence in the final 3D-printed phantom, which may influence the electromagnetic (EM) propagation inside the

phantom [119]. For this reason, the complexity of the model was reduced to minimize the amount of polymer in the fabricated phantom. When doing so, it was ensured that the main features of the anatomical region of interest were still present in the final phantom, and only small morphological details were reduced or removed. Firstly, the four main muscles (pectoralis minor, pectoralis major, latissimus dorsi muscle and rib-cage muscles, represented in Fig. 4.2 (c)) were merged in a single structure. This was possible due to their proximity and led to significant reduction of the complexity of the overall structure. Secondly, the rib-cage bones were removed as they are embedded in the pectoralis and rib-cage muscles. It was considered that adding bones would have significantly increased the complexity of the phantom while their effect on the MW signals would have been negligible, due to the high dielectric properties of the surrounding muscles. Additionally, the external surface of all the segmented tissues was smoothed in Meshlab [120], in order to mitigate some irregular or sharp edges that resulted from the segmentation. For each tissue, Laplacian smoothing [121] was first applied to the entire structure and then, locally, to regions which presented particularly rougher surfaces.

The final step in the creation of the phantom was the conversion of the muscle and lung solid structures to closed surface ones (i.e., hollow structures). An aperture on these two surfaces was included in order to enable filling them with the appropriate liquid TMM. Moreover, three slabs were added to the skin model, obtaining a partially-closed hollow structure which can be filled with fat liquid TMM. Both these steps were performed with software Blender [122].

The lung, muscle and fat containers were 3D-printed with 3D-printer Form 3 (Formlabs [114]) using the Grey Resin polymer (Formlabs [114]) and a wall-thickness setting of 1.2 mm. Such a thickness was found to be a good compromise between wall-thickness minimisation and phantom resilience. The bone was printed as a solid part using the Protopasta Conductive PLA [123] with 3D-printer Ultimaker 3 [124] using a layer thickness of 0.2 mm. Fig. 4.4 (a) shows the 3D-printed organs considered in the phantom. Fig. 4.4 (b)

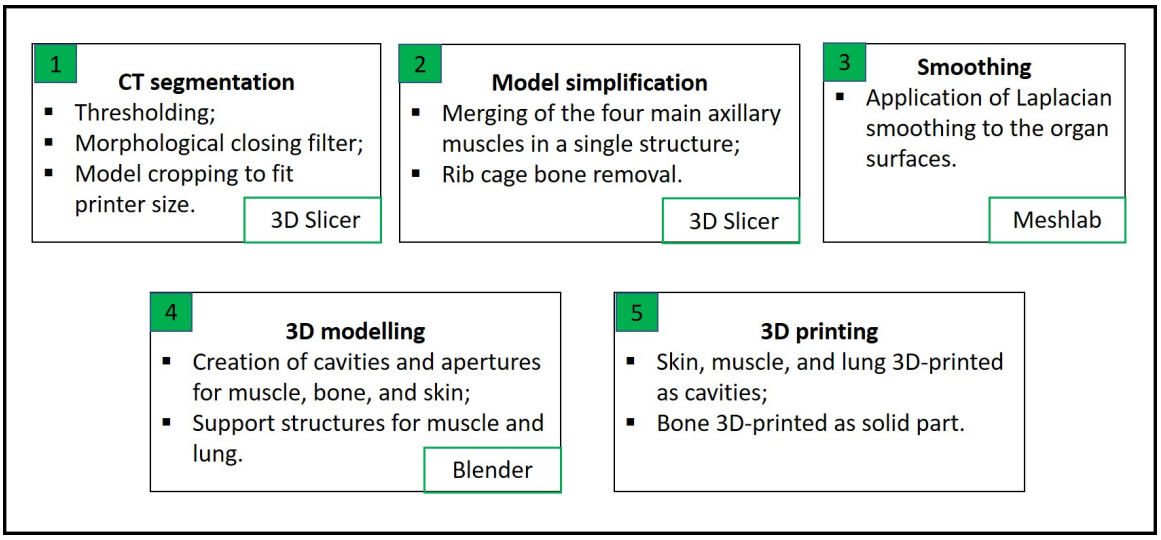

Figure 4.3: Schematic describing the sequence of steps taken to develop the 3D-printed phantom of the axillary region. For each step, the green box indicates the software used.

illustrates the assembled phantom. In the same figure, it is possible to observe extra fixtures that hold the organ compartments statically. Moreover, note that the outer container (i.e., fat container) is open on one side, in order to have easy access to the inside of the phantom. Only the muscle and lung containers include a dedicated aperture to allow filling them with TMMs.

The pipeline (from image segmentation to 3D-printing) that was followed to develop the axillary region phantom is summarised in Fig. 4.3.

Regarding the ALNs, these were manually sculpted as a set of ellipsoids with sizes ranging between 5 mm and 20 mm on their longer axis, which approximates their anatomical shape and size [4]. The modelled ALNs are made of a solid rubber TMM. The solid TMM was chosen because liquid TMM for ALNs would have implied surrounding the targets with plastic barriers, possibly influencing their response when illuminated with MW radiation. Additionally, in our lab, 3D-printed hollow ALNs had been filled with liquid TMM, and my colleague Daniela Godinho reported difficulties in filling them and in ensuring there were no air gaps. The hereby-fabricated ALNs were organized in a small network,

(a) (b) (c)

Figure 4.4: Physical phantom of the axillary region. **(a)** from left to right: 3D-printed torso, muscle, bone and lung are represented. Note that the torso, muscle, and lung compartments are hollow. **(b)** assembled phantom; a fixture which keeps the organs in place can be observed. **(c)** three solid ellipsoidal axillary lymph nodes made of rubber.

by connecting a nylon wire between them. This is possible because of the malleable consistency of rubber, which allowed to perforate the ALNs with a needle. A set of ALNs is represented in Fig. 4.4 (c). With this strategy, a single ALN or a network of ALNs were placed inside the phantom, thus increasing its representativeness of the axillary region. It should be noted that the ALN network may be placed in different positions, allowing for variability of the overall phantom. The ALNs are attached to the muscle structure through a set of small rings using a nylon string (the surface of the muscle container is shown in Fig. 4.4 (a)). The ALN fabrication procedure will be described in Sec. 4.2.2.

4.2 Tissue dielectric properties and tissue mimicking materials

This section firstly reviews the dielectric properties of the axillary tissues (Sec. 4.2.1); secondly, it describes the fabrication of TMMs (Sec. 4.2.2); lastly, it reports the dielectric characterization of the developed TMMs, and it compares their properties with those found

in the literature (Sec. 4.2.3).

4.2.1 Review of axillary tissue dielectric properties

The reference dielectric properties for fat, bone, and lung tissue were taken from [48] (data are available in the IT'IS Foundation database [125]). Specifically, using the same terminology as in [48], the dielectric properties of "breast fat", "cancellous bone", and "inflated lung" were used in this study. Data retrieved from measurements performed on *ex-vivo* bovine muscle tissue [111] were used to assign muscle dielectric properties. These data were acquired following the - state-of-the-art - best practices, as reported in [81][1]. The permittivity of ALNs was taken from the dielectric measurements that were performed during my secondment at the National University of Ireland Galway (Galway, Ireland), described in Sec. 3.3. In particular, the reference ALN permittivity was taken from all the measurements performed on the inner medulla of sheep inguinal LNs, given the relatively low intra- and inter-sample variability of those measurements. The reference dielectric properties of fat, lung, and muscle tissues are reported in Fig. 4.5, while the reference dielectric properties of ALNs are reported in Fig. 4.6. It should be noted that the ALN properties are reported in terms of the upper and the lower bound of the range where - according to Sec. 3.3 - ALN dielectric properties are expected to lie in.

4.2.2 Tissue mimicking material fabrication

Fat, muscle, and lung tissues were mimicked with liquid TMMs, as they are easy to produce and their dielectric properties are stable over time when preserved in a closed container. The bone structure was 3D-printed with a solid conductive polymer, because of its intricate shape. This polymer, known as "Protopasta Conductive PLA" presents dielectric properties

[1]Dielectric properties measured on bovine muscle tissue in [111] were used as these were measured at the National University of Ireland Galway (NUIG), a beneficiary in the EMERALD framework.

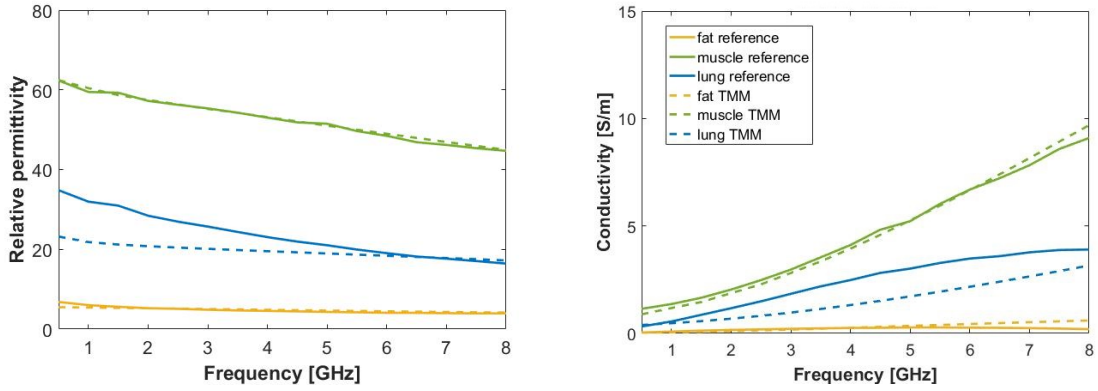

(a) (b)

Figure 4.5: Dielectric properties of the tissues represented by liquid tissue mimicking materials (TMMs). **Solid lines**: reference permittivity of fat, muscle, and lung. **Dashed lines:** measured permittivity of the corresponding liquid TMMs. **(a)** Relative permittivity ϵ', and **(b)** conductivity σ.

similar to those of the cancellous bone tissue for the considered frequency band [126]. ALN were fabricated with solid TMMs.

The liquid TMMs are mixtures composed of a mix of Triton X-100 (TX-100), water, and sodium chloride (NaCl), according to the methodology described in [127]. The left column in Tab. 4.1 reports the quantities of TX-100 and NaCl for each TMM. The solid TMMs are mixtures of different amounts of polyurethane (part A and part B of VytaFlex 20, from Smooth-On, Easton, PA, USA), carbon black (acetylene 50% compressed, 99.9%+ from Alfa-Aera, Ward Hill, MA, USA), graphite (general purpose powder from Fischer Scientific, Loughborough, Leicestershire, United Kingdom), and acetone, as proposed in [106; 107; 110; 128]. As reported in those studies, the mixing of the parts A and B of VytaFlex 20 provides a solid and flexible polyurethane matrix which can be easily used to create various shape and size targets. Carbon black and graphite powders can be added to increase the dielectric properties of the mixtures (the higher the powder mass percentage, the higher the resulting dielectric properties). Regarding acetone, this helps amalgamate the materials in the mixtures, hence it facilitates the blending process; the addition of this

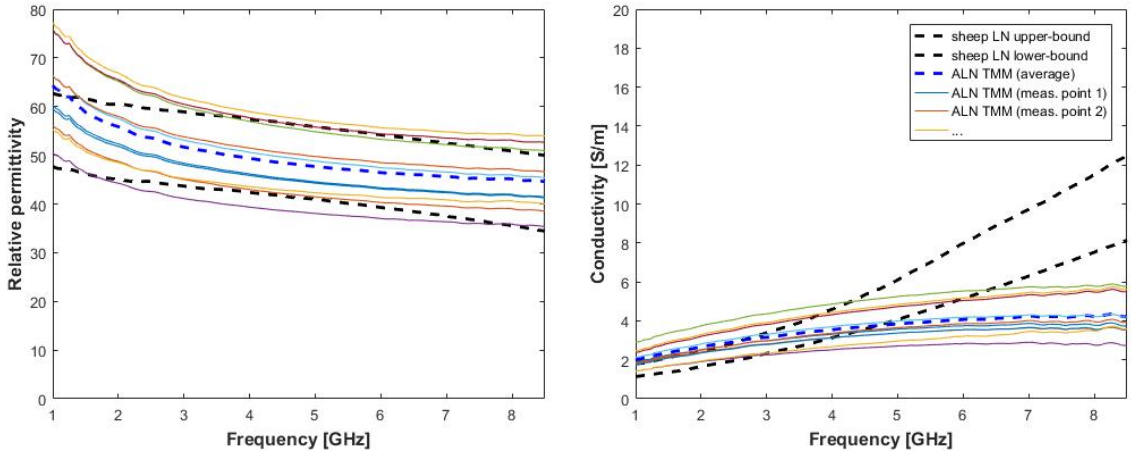

(a) (b)

Figure 4.6: Dielectric properties of sheep lymph nodes (used as reference), and of axillary lymph node (ALN) tissue mimicking material (TMM). **(a)** Relative permittivity ϵ', and **(b)** conductivity σ. **Black dashed lines** correspond to reference dielectric properties of ALNs (the two lines define the range where the dielectric properties of ALNs are expected to lay in). **Thin solid lines** correspond to ALN TMM dielectric properties measured on several adjacent points. **Dashed blue lines:** average measured dielectric properties of the ALN TMMs.

compound is particularly useful to recreate high powder-content mixtures (such as those of ALN TMMs), as the powder makes the blending process more difficult. To recreate solid TMMs, a first base of polyurethane (part A and part B were mixed in equal quantities as per manufacturer instructions) was prepared; then, the required amount of acetone was added into it while mixing. In a separate glass, carbon black and graphite powders were mixed together in order to obtain a homogeneous powder mixture. Immediately after, the powder mixture was slowly added to the polyurethane base while mixing. The blending of the mixture continued for approximately 5 to 10 minutes, aiming to obtain a mixture which was as homogeneous as possible. The methodology proposed in [106], to mimic breast glandular tissue, was used as a starting point to obtain ALN TMM. In order to optimize the mixture ingredients, a first set of 7 mixtures (each mixture weighed approximately 30 g) was pre-

Table 4.1: Liquid tissue mimicking material (TMM) mixture compounds. Muscle, fat, lung, and axillary lymph node liquid TMMs are made of a liquid mixture of TX-100 and salted water. The first column of the table reports, for each liquid TMM, the percentage volume of TX-100 and the concentration of NaCl in deionized water. The second column of the table reports the average (± standard deviation) absolute error, in terms of permittivity and conductivity, computed for each TMM properties with respect to the corresponding target properties.

tissue	**Mixture composition**		**Average (± st.dev) absolute error in TMM dielectric properties**	
	TX-100 [vol%]	NaCl [g/l]	Relative permittivity	Conductivity [S/m]
Muscle	26.5	7.4	0.4 (± 0.3)	0.21 (± 0.13)
Lung	55.0	4.51	4.2 (± 3.7)	0.89 (± 0.43)
Fat	100	0	0.3 (± 0.2)	0.11 (± 0.11)

Table 4.2: Solid tissue mimicking material mixture compounds. ALN TMM is made of a mixture of polyurethane, graphite, carbon black, and acetone. The table reports the mass percentage of polyurethane, graphite, and carbon black included in the mixture; the added quantity of acetone is also reported.

Tissue	**Polyurethane (A+B) [% w/w]**	**Graphite [% w/w]**	**Carbon black [% w/w]**	**Acetone [ml/100g]**
ALN	53	41	6	4

pared; their dielectric properties were measured with the OECP method, and compared to the target properties for ALNs. The resulting properties were used to adapt the recipe of the subsequent set of mixtures. The optimised mix that was finally adopted to mimic ALNs in the proposed phantom is reported in Table 4.2.

4.2.3 Tissue mimicking material dielectric measurements

The TMM dielectric properties were measured with the OECP method. Fig. 4.5 shows the measurement results, and compares the measured properties of the TMMs to the target dielectric properties. The average (± standard deviation) absolute errors in terms of relative permittivity and conductivity (1 GHz to 8 GHz frequency band), are reported for the liquid

TMMs in Table 4.1. Regarding fat and muscle, there is good agreement between the TMM and the respective target tissue, with a mean square error lower than 6.7% in the 1 GHz to 8 GHz frequency band. Regarding lung TMM, the permittivity is 50% to 14% below the adopted reference value, for frequencies between 0.5 GHz and 4.5 GHz. However, lungs are at a greater depth than the muscle, which means that it is the tissue that has the least influence on the E-field coupling in the ALN region, and so the model mismatch will not affect the work presented in this paper (this will be demonstrated in Sec. 4.3).

Regarding the ALN TMM, a more in-depth analysis of their dielectric properties was carried out. Fig. 4.6 reports repeated measurements performed on several measurement points of the ALN TMM. Measurements were performed using a 2.2 mm outer-diameter OECP. The results show very high variability (relative permittivity ranging from 40 to 60 at 4.5 GHz) across different measurement points, suggesting that the TMM is highly heterogeneous at millimeter-scale (the expected sensing radius of the OECP is smaller than 2.3 mm, as reported in [52; 86]). However, it is not expected that the observed mm-scale heterogeneity has a significant effect on the application of MWI to the developed ALN phantoms. Indeed, changes in dielectric properties at mm-scale do not affect the EM propagation at centimeter-scale, which is comparable with wavelengths typically used for MWI.

4.3 Numerical assessment of the phantom

The proposed phantom is composed of multiple polymeric containers which hold the TMMs. However, it is well-known that polymers have a relative permittivity between 2 and 3, which is lower than the permittivity of most tissues. Therefore, this section aims to quantify the effect of the polymeric containers of the phantom through full-wave simulations. All the numerical results presented below were obtained using Computer Simulation Technology (CST) Microwave transient solver [72].

In order to assess the influence of the 3D-printed polymeric containers, two setups were considered. The first setup (*Phantom*) was the numerical representation of the 3D-printed phantom, and hence it included the polymeric walls of the phantom, with a thickness of 1.2 mm. A dielectric constant of 2.5 and a loss tangent of 0.02 were assigned to the polymer. (The dielectric properties of the polymer were measured using the microstrip method proposed in [129].) Fig. 4.7 (a, b) illustrates the model. The grey surfaces represent the polymer. The second setup (*Axilla*) represented the developed numerical model of the axillary region before the polymeric walls were created, including a skin tissue layer of 1.2 mm thickness. The latter is shown in Fig. 4.7 (c). Note that there are no grey surfaces, and an external brown layer mimicking the skin is visible. In both setups, the tissues were assigned the reference complex permittivity values as plotted in Fig. 4.5 and in Fig. 4.6. The procedure in [48] was used to assign the skin tissue properties.

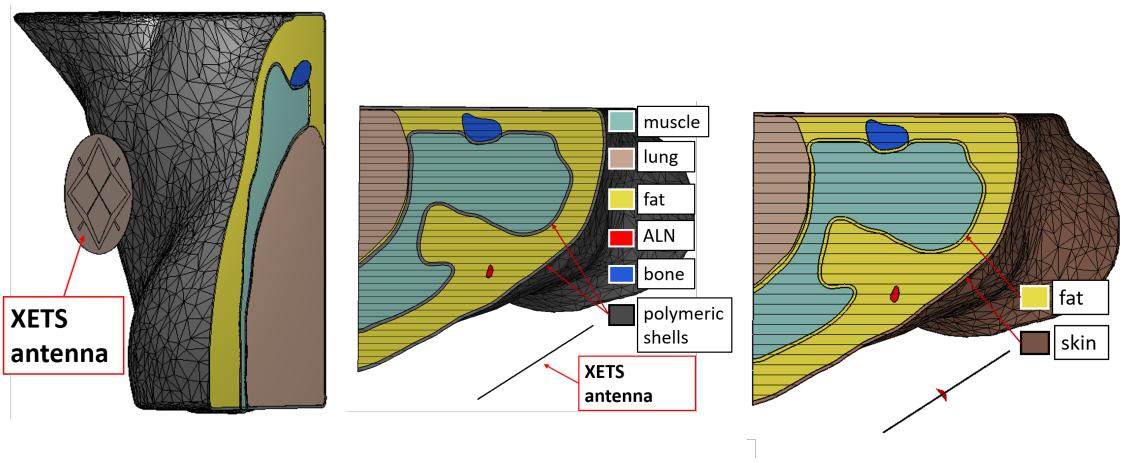

(a) (b) (c)

Figure 4.7: **(a)** 3D-rendering view, and **(b)** axial view (at the level of the sternum) of the numerical model of the developed physical phantom (*Phantom*). **(c)** Numerical model of the realistic axillary region (*Axilla*), in axial view. Each colour represents a different component as detailed in the legend. A crossed Exponentially Tapered Slot (XETS) antenna is placed close to the torso.

As for the EM source, a broadband antenna operating in the 2 GHz - 6 GHz frequency

band was used. The antenna, represented in Fig. 4.8 (a), is a crossed Exponentially Tapered Slot (XETS), which was previously reported in [130; 131]. Study [131] includes the dimensions of the antenna as used in the present chapter. The antenna is suitable for imaging applications, not only for its impedance matching over a broad bandwidth, but also because it presents a stable phase centre along frequency. Fig. 4.8 (b) represents the magnitude of the input reflection coefficient, $|S_{11}|$, of the antenna in free-space, which is below -10 dB, as is common practice in antenna design. The position of the antenna in the two setups is visible in Fig. 4.7.

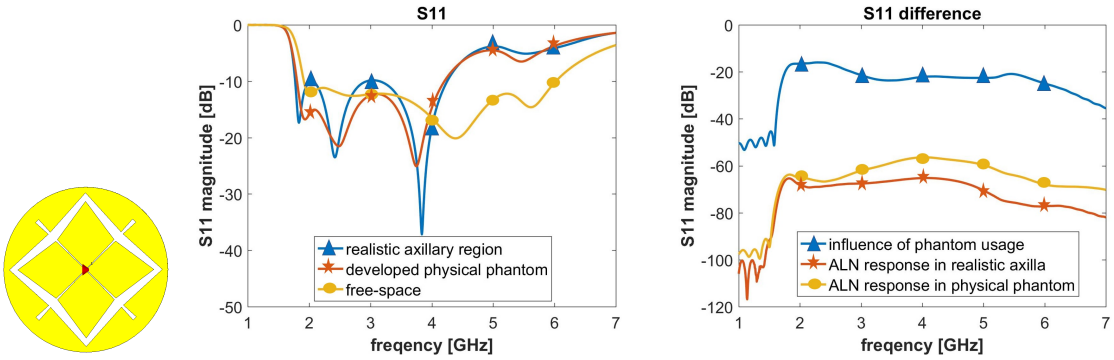

(a) (b) (c)

Figure 4.8: **(a)**: Schematic of the crossed Exponentially Tapered Slot (XETS) antenna. **(b, c)**: influence of the usage of the developed phantom on the reflection coefficient (S_{11}). **(b)** shows the comparison between the S_{11} magnitudes measured by the XETS when stimulating the *realistic axillary region* and the *developed physical phantom*; the S_{11} of the antenna in free-space is also reported. **(c)** shows the impact of the polymer on the S_{11} (difference on the S_{11} between the realistic axilla and phantom), and the response of the axillary lymph node (difference on the S_{11} between the model with the ALN and without the ALN) in the phantom and in the realistic axillary region.

The E-field was computed considering the two setups. The magnitude of the E-fields, $|E^{phantom}(f)|$ and $|E^{axilla}(f)|$, at $f = 4\ GHz$ are plotted in Fig. 4.9 (a) and Fig. 4.9 (b), respectively. The E-field has a magnitude of about 30 V/m to 40 V/m in the ALN region in both scenarios, thus suggesting the polymer has little influence on the results. Moreover, the E-field that couples with the muscle is approximately 20 dB below the E-field

in the region of the ALN (circled in Fig. 4.9). This is a consequence of the losses and the high dielectric contrast between muscle and fat, which causes a very large reflection at the interface between the two tissues. The low magnitude of the E-field coupled with the muscle suggests that the propagation beyond the muscle can be considered negligible. Therefore, the reduced dimensions of the phantom (145mm x 145mm x 180mm) minimally impacts the measurements, and boundary conditions on the back sides of the phantom (non-anatomically realistic flush-cuts) are considered unnecessary.

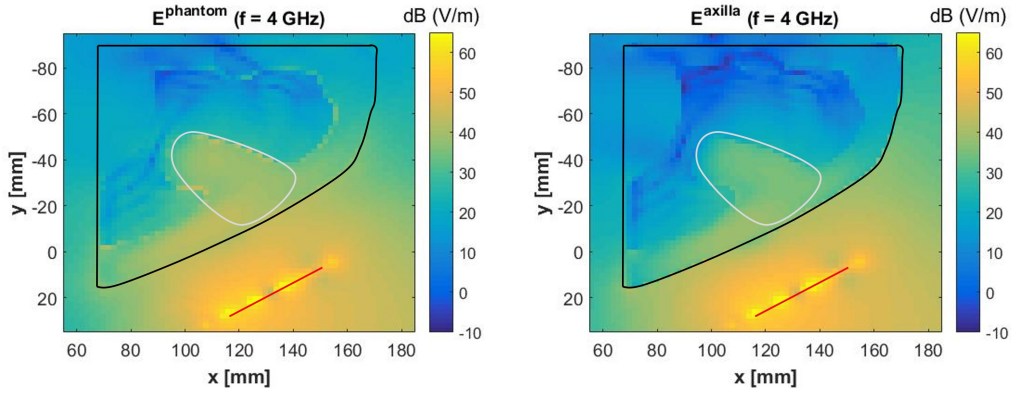

(a) (b)

Figure 4.9: Magnitude of the electric fields ($f = 4GHz$) computed on the XY-plane (reference axes in Fig. 4.7) at the level of the sternum, when considering two different setups. **(a)** $E^{phantom}$, refers to the setup in Fig. 4.7 (b). **(b)** E^{axilla} refers to the setup in Fig. 4.7 (c). The electromagnetic source is the crossed Exponentially Tapered Slot (XETS) antenna. The black line identifies the contour of the axillary region (i.e., polymeric external shell on the left **(a)** and skin on the right **(b)**). The white line identifies the axillary lymph node region. The red line identifies the antenna.

In order to better understand the influence of the polymer on the energy coupled with the body, the E-field difference between the *Axilla* and *Phantom* models was calculated as:

$$E_{dB}^{diff} = 20log_{10}|E^{axilla}| - 20log_{10}|E^{phantom}| \tag{4.1}$$

The E_{dB}^{diff} is computed as the difference of the amplitudes in order to specifically assess

power difference. This is deemed acceptable as it is expected that the phase offset introduced by the polymer is negligible for imaging purposes. Such E-field difference is plotted in Fig. 4.10 at 2 GHz, 4 GHz, and 6 GHz. The results show that E_{dB}^{diff} varies between -2 dB at 2 GHz and -8 dB at 6 GHz, in the volume corresponding to the ALN region. Considering the advantages brought by the use of a 3D-printed phantom, the reported E-field differences can be considered acceptable.

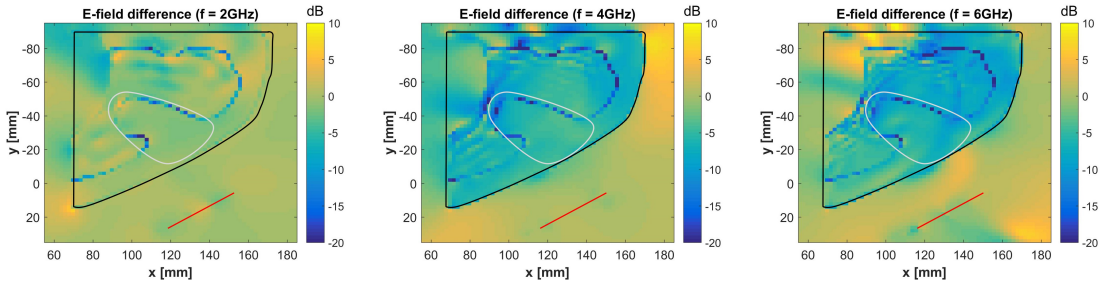

(a) (b) (c)

Figure 4.10: Effect of using the developed phantom (instead of a realistic axillary region) on the energy coupling inside the axillary region tissues. The plot represents the difference between the total field computed in the *Axilla* model (E^{axilla}) and the total field computed in the *Phantom* model ($E^{phantom}$). The electromagnetic source is the XETS antenna. The black line identifies the contour of the axillary region (i.e., the skin or phantom surface in the cross-sectional view). The white line identifies the axillary lymph node region. The red line identifies the antenna. Frequency: **(a)** $f = 2GHz$; **(b)** $f = 4GHz$; **(c)** $f = 6GHz$.

The present analysis was extended to the assessment of the impact of the polymer on the input reflection coefficient of the antenna, S_{11}. To this end, the difference on the S_{11} between the *Axilla* and the *Phantom* was also calculated:

$$S_{11}^{diff} = 20log_{10}\left(\left|S_{11}^{phantom} - S_{11}^{axilla}\right|\right) \tag{4.2}$$

where $S_{11}^{phantom}$ and S_{11}^{axilla} represent the simulated S_{11} with the phantom and the realistic axillary region, respectively. The results are plotted in Fig. 4.8 (c). It can be observed that

the influence of the polymer is lower than -20 dB, thus suggesting that the influence of the polymer is not significant.

Lastly, the ALN response along frequency was analysed when embedding an ALN in the phantom (S_{11}^{ALNph}) and in the realistic axillary region (S_{11}^{ALNax}). The ALN was kidney-shaped and 7 mm long on its longer axis, as shown in Fig. 4.7. Its permittivity was assigned relying on the measurements performed on ALNs in Sec. 3.3. The response of the ALNs was inferred by calculating:

$$S_{11}^{ALNph} = 20log_{10}\left(\left|S_{11}^{phantom} - S_{11}^{phantom+ALN}\right|\right) \tag{4.3}$$

$$S_{11}^{ALNax} = 20log_{10}\left(\left|S_{11}^{axilla} - S_{11}^{axilla+ALN}\right|\right) \tag{4.4}$$

where $S_{11}^{phantom+ALN}$ and $S_{11}^{axilla+ALN}$ are the simulated input reflection coefficients of the phantom with ALN and of the realistic axillary region with ALN, respectively. These results are shown in Fig. 4.8 (c). The response of the ALN is in the order of -60 dB and -70 dB for the physical phantom and for the axilla models, respectively, in the frequency band between 2 GHz and 6 GHz. This response can be considered sufficient for ALN detection, given that commercial VNAs have a dynamic range of a least 90 dB. Additionally, the magnitude of such response is comparable to the one experimentally obtained for breast tumor imaging in [132], where the authors successfully detected the tumour in its correct position.

4.4 Conclusions

In this chapter, an axillary phantom for experimental assessment of MWI for ALN screening was developed. The physical phantom is the 3D-printing of a segmented CT image; therefore, it is anatomically realistic, and it reproduces fine morphological details. The use of polymeric containers allowed to use liquid TMMs, which is a great advantage as

their dielectric properties mimic the axillary tissues with sufficient accuracy for the purpose of MWI. Additionally, liquid TMMs are easy to produce, meaning that their dielectric properties can be easily adjusted to account for the physiological variability of tissue dielectric properties among individuals. Last, the 3D-printed phantom is easily re-configurable, which allows to experimentally study the influence of one single organ on the imaging results by simply removing it from the setup, or by adjusting its position. Also, the physical phantom construction involved a simplification of the original anatomically realistic numerical phantom, which was necessary to address the trade-off between polymer-presence and anatomical-details. As a disadvantage, full-wave simulation showed that the polymer tends to influence the coupling of the E-field inside the phantom. After testing the developed phantom numerically, it was found that the 3D-printed phantom alters the E-field coupling into the tissue by 7 dB at maximum, at the centre frequency ($f = 4$ GHz), which is considered acceptable given the advantages brought by the use of a 3D-printed phantom.

Additionally, the response of a relatively small ALN inside the axillary region was studied. Such response was estimated to be sufficiently large (-60 dB to -70 dB) to be sensed by commercial VNAs, which motivates further studies of ALN MWI.

Chapter 5

Assessment of MWI for axillary lymph node screening

This chapter presents the work developed to assess MWI for the screening of level I ALNs - the ALNs more likely to receive drainage from tumour cells first (see Chapter 1) - using the axillary region model introduced in Chapter 4. Axillary MWI presents challenges that are not commonly posed by other MWI systems intended for biomedical applications. For instance, in breast and brain MWI [60; 106; 132], the antennas are usually placed all around the body part, providing sufficient "angular information" to reconstruct the image. The morphology of the axillary region limits the measurement domain to an arc ($\approx 70° - 90°$ on the transverse plane) around the area of interest, which makes the problem aspect-limited (i.e., the target cannot be probed from all possible angles [133; 134]). Additionally, the concave shape of the axillary region limits the placement of antennas and cables, also restricting the number of probing points in the measurement domain. Finally, level I ALNs are usually located near muscle tissue (with similar dielectric properties) that may have comparable MW response, which poses an additional challenge.

The first approach to ALN MWI (Sec. 5.1) consisted in testing a monostatic radar MWI

setup, with the primary objective of assessing the muscle response. Radar MWI reconstructs qualitative images based on wave reflection caused by dielectric properties discontinuity in the propagation medium.

The second approach to ALN MWI consisted in testing a tomographic imaging setup using the DBIM-TwIST algorithm (illustrated in Chapter 2), which represents the most significant contribution in this chapter. MWT algorithms allow reconstructing quantitative images which could be used to discriminate healthy and metastasised ALNs based on their dielectric properties. Additionally, MWT algorithms explore available prior information, incorporating a guess of the dielectric map of the imaging domain (*initial guess*) into the reconstruction algorithm. This practice has been suggested to significantly improve image quality in breast MWT [135], and can be crucial in axillary MWT given the above mentioned challenges of the application. A general description of the adopted MWT setup is provided in Sec. 5.2, which presents the challenges of the application, and describes axillary models, antennas, immersion liquids, and the imaging algorithm adopted in all different scenarios tested in this chapter. It is worth mentioning that depending on the availability of materials and laboratories involved in this project, slightly different setup design were adopted throughout the research carried out. Nonetheless, an effort was made to align the setup configuration of the numerical investigations with the experimental campaign.

The first study on axillary MWT (Sec. 5.3) consisted in numerically assessing (i) the potential of the application for the detection and dielectric properties estimation of ALNs, and (ii) the robustness of the system to uncertainties/errors in the prior information of surrounding tissues (notably, muscle dielectric properties and its position). The application was assessed using data generated with a 2D MWT system.

Then, numerical studies using data computed with full wave simulations (in CST) are presented. Firstly (Sec. 5.4), the effect of having limited angular view in axillary MWT is assessed. Secondly (Sec. 5.5), a frequency by frequency analysis is carried out over a broad band (0.8-2.5 GHz), with the objective of identifying the optimal probe placement

and operating frequencies. This is a challenging task given the space constrains in the axillary region, which can limit the exploitation of too short wavelengths (lower wavelengths require more probing points in the measurement domain). Additionally, the possibility of acquiring data from different angular perspectives is proposed (Sec. 5.5) as a means to increase the probing points in the measurement domain, which may increase the amount of retrieved information.

An experimental MWT setup for ALN detection is proposed and tested (Sec. 5.6) using the anthropomorphic phantom of the axillary region developed in Chapter 4, with increasing levels of complexity and anatomical details.

The last study developed in this chapter (Sec. 5.7) proposes a method to quantify the data and model mismatch errors (i.e., *modelling errors*), after calibrating the data with the state-of-the-art calibration method. This is an important analysis to validate (i) the capability of the adopted 2D EM-solver to model the axillary MWT actual setup, and (ii) the capability of the adopted calibration method to mitigate *modelling errors*.

Finally, (Sec.5.8) the main conclusions of the chapter are drawn.

The work developed on axillary MWT (Sec. 5.2-5.7 resulted from a collaboration with the Faculty of Natural and Mathematical Sciences, at King's College London (London, UK), who provided the code for the DBIM-TwIST imaging reconstructions; while the experimental data used in Sec. 5.6 were acquired during a one-month visiting period at the Department of Electronics and Telecommunications, at Politecnico di Torino (Turin, Italy) in May 2022.

The work developed using the radar-based MWI setup (Sec. 5.1) was published in the following conference paper:

- Savazzi M., Costa, J. R., Fernandes C. A., Felício J. M., & Conceição R. C. "Numerical Assessment of Microwave Imaging for Axillary Lymph Nodes Screening Using Anthropomorphic Phantom". 2021 15th European Conference on Antennas

and Propagation (*EuCAP*), *Dusseldorf, Germany* (pp. 1-4). https://doi.org/10.23919/EuCAP51087.2021.9410925

The work developed to assess the robustness of the proposed MWT system using prior information with varying levels of accuracy (Sec. 5.3) was published in the following conference paper:

- Savazzi M., Karadima O., Felício J. M., Fernandes C. A., Kosmas P. & Conceição R. C. "Effect of Varying Prior Information in Axillary 2D Microwave Tomography". 2022 16th European Conference on Antennas and Propagation (*EuCAP*), *Madrid, Spain*, (pp. 1-5). https://doi.org/10.23919/EuCAP53622.2022.9769372

Part of the numerical assessment (Sec. 5.4 and Sec. 5.5) and the experimental assessment of axillary MWT (Sec. 5.6) is currently under review as:

- Savazzi M., Rodriguez D. O., Karadima O., Fernandes C. A., Tobon J. V., Vipiana F., Kosmas P., Felício J. M., & Conceição R. C. "Experimental Assessment of Axillary Lymph Node Microwave Tomography using Anthropomorphic Phantoms", IEEE Journal of Electromagnetics, RF and Microwaves in Medicine and Biology. (*Early Access*). https://doi.org/10.1109/JERM.2023.3241777

The assessment of the effects of acquiring data from different angular perspectives (Sec. 5.5) was presented at the 2022 IEEE Conference on Antenna Measurements and Applications (CAMA 2022), with the following title:

- Savazzi M., Rodriguez D. O., Origlia C., Karadima O., Fernandes C. A., Tobon J. V., Vipiana F., Kosmas P., Felício J. M., & Conceição R. C. "Experimental Assessment of the Effects of Increasing Illumination Angles to Maximise Useful Information in Axillary Microwave Tomography", in *2022 Conference on Antenna Measurements and Applications (CAMA 2022)*, Guangzhou, China. (*Accepted abstract*)

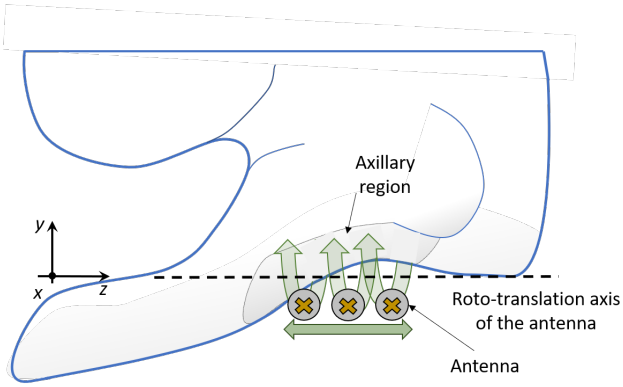

Figure 5.1: Axillary microwave monostatic radar imaging setup: the patient lies in a supine position while the antenna roto-translates along the z-axis, scanning the axillary region. In realistic clinical scenario, a bed with an opening where the patient can insert her arm may be considered. This would allow easy access to the axillary region, while ensuring the patient is stable during the examination.

5.1 Axillary radar microwave imaging

In this section the potential of MWI for the detection of ALNs using a radar monostatic system is assessed. Given the the proximity of ALNs to muscle tissue (with similar dielectric properties), the response of an ALN embedded in fat is first studied calibrating (i.e., subtracting) the response of the muscle. As a second step, the muscle response is considered when reconstructing the image of the phantom. Sec. 5.1.1 illustrates the setup adopted to test radar MWI. Sec. 5.1.2 describes the signal processing used to reconstruct the microwave images. Sec. 5.1.3 presents the imaging results and draws preliminary conclusions on the feasibility of ALN MWI.

5.1.1 Radar microwave imaging setup

This section describes the MWI setup that was adopted to test the application of radar-MWI to detect ALNs, together with the anatomically and dielectrically realistic phantom described in Chapter 4.

The setup was designed to scan the axillary region considering a scenario in which the patient lies in a supine position, with her arm extended along the head. The radar-type setup is monostatic, which employs a single antenna roto-translating around the axillary region. A schematic of the setup is reported in Fig. 5.1. In contrast with the majority of medical MWI setups, in which the part of the body being scanned is immersed in a liquid [136; 137; 138], the envisioned setup is dry and fully contact-less, which represents an advantage both in terms of system design and usability, as well as patient hygiene. Some groups working on medical MWI have demonstrated the feasibility of such a dry approach [132; 139], including the one at Instituto de Telecomunicações (Lisbon, Portugal). In [132], the authors quantified - for the case of breast MWI - the reduction of skin reflection caused by different matching media, and concluded that the adoption of an immersion liquid can mitigate the reflection up to a maximum of 8 dB (1-6 GHz bandwidth). Considering the expected response of an ALN in a dry MWI setup (-60 dB to -70 dB as detailed in Sec. 4.3) and the dynamic range of the VNA (110 dB), an 8 dB power reduction due to skin backscattering is acceptable, and does not preclude proposing a dry imaging setup for ALN MWI.

The probing antenna is a cross-Exponentially Tapered Slot (XETS) antenna, operating in the 2-6 GHz frequency band, originally proposed in [140]. The XETS is suitable for imaging applications not only for its impedance matching over a broad bandwidth but also because it presents a stable phase centre along frequency. In this study, the antenna reflection coefficient is sampled in 667 equally-spaced frequency points between 2 and 6 GHz, covering the whole operating bandwidth of the XETS.

The adopted axillary model is the numerical model of the 3D-printed anthropomorphic phantom (it includes plastic containers) described in Chapter 4. The phantom originates from the segmentation of a patient with body mass index (BMI) equal to $21 kg/m^2$, which is relatively low if compared with the average BMI of patients undergoing sentinel lymph node biopsy (SNLB) [33]. Given the marginal influence that lung and bone organs have

on the electric field (E-field) coupling in the axillary region (Sec. 4.3), the phantom is only composed by fat, muscle, and ALN tissues. The ALN is a spherical shape (radius = 5mm), embedded in fat tissue. It is placed 5mm from the plastic-air interface, and 9mm from the fat-muscle interface. The tissue dielectric properties were defined according to Sec. 4.2.1.

5.1.2 Methodology

The image reconstruction algorithm based on the wave migration was proposed in [141]. The intensity I of each image voxel is computed as follows:

$$I(v) = \sum_{i}^{N_{ant}} \sum_{f_k}^{N_f} s_{ii}(f_k) e^{jk_0(2d_{air}+2d_{fat}n_{fat})} \tag{5.1}$$

where d_{air} is the distance between the XETS antenna and the phantom surface, d_{fat} is the distance between the voxel and the phantom surface, and n_{fat} is the refractive index of fat. S_{ii} is the (calibrated) reflection coefficient measured ar the i^{th} antenna position which has 1xN_f size, where N_f is the number of frequency points. N_{ant} is the number of antenna positions. $k_0 = \frac{2\pi f_k}{c}$ is the wave-number in vacuum, where c is the speed of light in vacuum.

5.1.3 Results

During the S_{ii} acquisition, 10 antenna positions were considered. The antenna positions are spaced by a 6° angular step on a circular trajectory which lies on the same XY-plane (reference system in Fig. 5.1) of the ALN. The sweep radius is 85mm, resulting in a 9mm distance between adjacent antenna positions. The distance between the antenna and the phantom surface ranges between 20mm and 30mm, depending on each antenna position.

Fig. 5.2 shows the reconstructed image in the XY-plane which contains the ALN. Fig. 5.2 (a), shows the reconstructed image, obtained when isolating the response of the

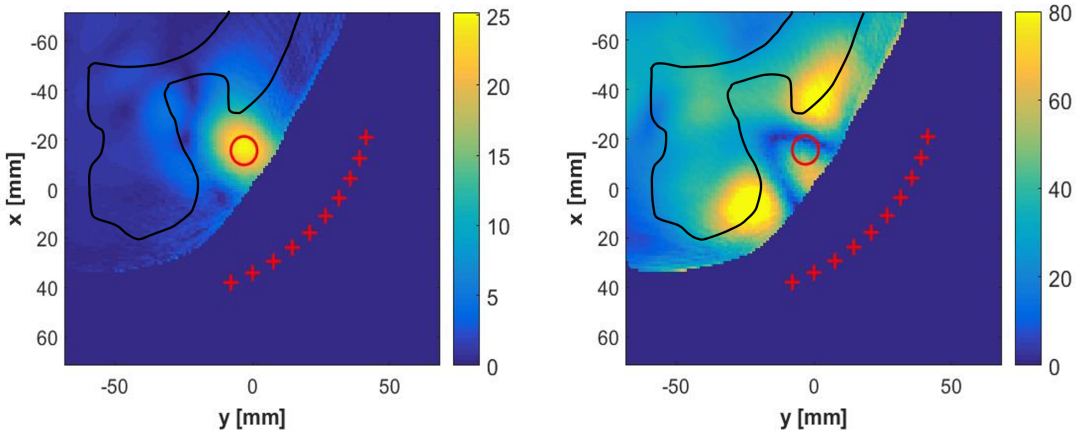

(a) (b)

Figure 5.2: Radar imaging results: reconstructed energy map of the axillary region with one axillary lymph node (ALN). The represented XY-plane corresponds to the plane where the centre of the ALN is placed. The red crosses indicate the antenna positions; the red circle shows the actual position of the ALN; the black line traces the profile of the muscle. In **(a)**, the reflection coefficient (S_{ii}) is calibrated to isolate the ALN response; while in **(b)** the S_{ii} is calibrated to isolate the ALN and the muscle responses.

ALN. To isolate the ALN response, the reflection coefficient (S_{ii}) inputted in Eq. 5.1 was computed as the difference between the reflection coefficient obtained when illuminating the axillary phantom with all its components (polymeric containers, fat, muscle, lung, and ALN) and the reflection coefficient obtained when illuminating the same phantom without ALN (target). The results shows that the ALN is successfully detected in its correct location when isolating its response.

In order to study the influence of the muscle on the imaging results, image reconstruction was performed considering both the response of ALN and muscle. To do so, the S_{ii} inputted in Eq. 5.1 was computed as the difference between the reflection coefficient obtained when illuminating the axillary phantom with all its components (polymeric containers, fat, muscle, lung, and ALN) and the reflection coefficient obtained when illuminating the same phantom without ALN and muscle, which isolates the response of both ALN and muscle.

The results are shown in Fig. 5.2 (b). When comparing Fig. 5.2 (b) to Fig. 5.2 (a), there is an obvious deterioration of the imaging results, as a consequence of the large dielectric contrast between muscle and fat. The two extremities of the muscle that are closer to the skin are detected as the two highest magnitude points in Fig. 5.2 (b). The ALN is detected between those spots. This can be considered a promising result given the large surface of the muscle and its dielectric properties, compared to the much smaller size of the ALN. It should also be emphasized that the detection of the ALN was particularly challenging because of the low BMI of the adopted phantom, where muscles are closer to the skin, causing high reflections.

5.2 Axillary microwave tomographic (MWT) imaging

A generic representation of the MWT system proposed in this thesis is reported in Fig. 5.3. In the proposed configuration, the body is illuminated by N_A antennas placed on a single transverse plane $\bar{z}$, facing the axillary region. For the purpose of this thesis, it was easy to define the reference system with axis corresponding to the three orthogonal edges of the axillary phantom (origin in the crossing point), as indicated in Fig. 5.3 (a). Considering that antennas are placed on a single transverse plane, the problem at hand can be described referring to the 2D-schematic represented in Fig. 5.3 (b), which illustrates a generic representation of the imaging scenario, at an arbitrary $\bar{z}$. The position of the i-*th* antenna can be defined as $A_i(\rho_i, \phi_i)$, referring to the polar coordinates centred in $O_A(x, y, \bar{z})$, illustrated in Fig. 5.3 (b). As a result, the set of probes subtends an angle $\Phi = (N-1)\Delta\phi$, being $\Delta\phi$ the constant angular spacing between adjacent antennas. It is emphasised that Φ is typically limited to $70° - 90°$ given the morphology of the axilla, while $\Delta\phi$ is limited by the size of the antennas. The positioning of the antennas in close proximity to the body is hampered by the concave shape of the axillary region, which represents another challenge of the application. Indeed it has been shown [142] that placing the probes near the imaging

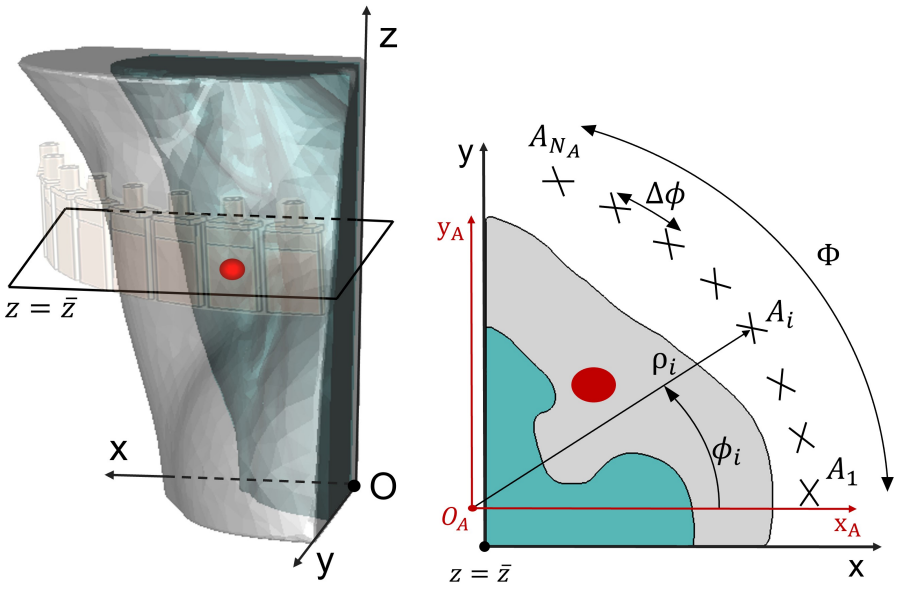

(a) (b)

Figure 5.3: Tomographic system used to assess axillary microwave imaging: N_A antennas, are placed - on a single plane $\bar{z}$ - on an arc subtending an angle Φ, around the axillary region. The schematic also illustrates the main axillary tissues: fat, muscle, and axillary lymph node (ALN). **(a)** Rendering view; **(b)** cross-sectional view of the system.

domain improves reconstruction capabilities in the region close to the border of the imaging domain, which may play a major role in ALN MWT, where the region of interest is only a superficial layer of the body, and not the deeper region occupied by muscle tissue.

The following subsections describe all different parts of the proposed MWT system and the main design constrains.

5.2.1 Axillary models

To assess ALN MWT, axillary models derived from the anthropomorphic phantom developed in Chapter 4 were considered. The adopted axillary models consist of three tissue types: fat, muscle, and ALN; while lung and bone tissues were not considered due to their marginal influence on the E-field coupling inside the axillary region (Sec. 4.3). Three

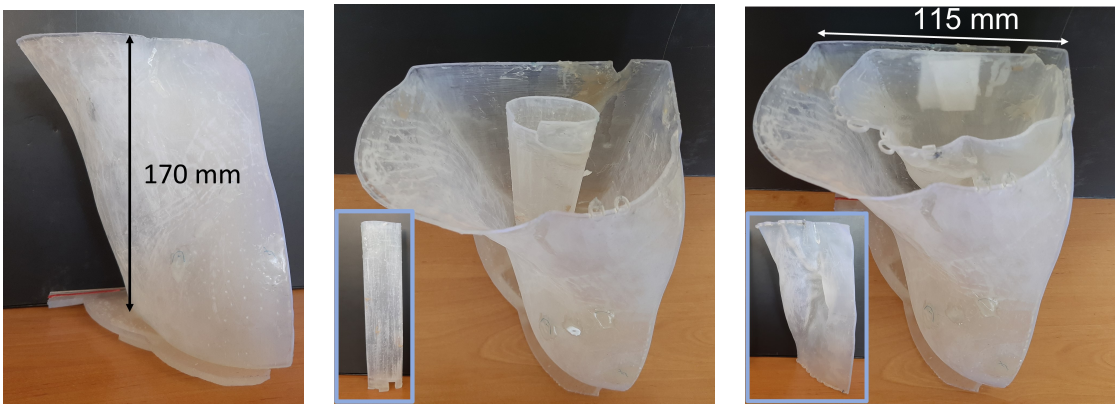

(a) H model (b) MTS model (c) MTA model

Figure 5.4: Representation of the three different axillary models, with increasing level of anatomical fidelity: (a) homogeneous (H) model; (b) multi-tissue simplified (MTS) model, (c) multi-tissue anthropomorphic (MTA) model.

increasing levels of anatomical accuracy were considered: (i) homogeneous (H) model, consisting of fat tissue only; (ii) multi-tissue simplified (MTS) model, where the muscle was modeled as an elliptic cylinder ($axis_1 = 38mm$; $axis_2 = 12mm$); (iii) multi-tissue anthropomorphic (MTA) model, which is an accurate representation of axillary anatomy, composed of fat and anthropomorphic muscle tissues. Fig. 5.4 reports pictures of the H, MTS and MTA axillary phantoms used in this chapter.

5.2.2 Immersion liquids and frequency range

As this chapter represents a first approach to ALN MWT, an immersion liquid was used despite its hygienic and handling issues. The use of an immersion liquid was found important (i) to reduce the size of the antennas, (ii) to increase the system resolution, and (iii) to moderate the mismatch between the system and its model in the imaging algorithm [143]. However, increasing losses in the immersion liquid can cause excessive signal attenuation and deteriorate the reconstruction quality [56]. Additionally, wavelength reduction is associated to higher degree of non-linearity which hampers the inversion, and requires an

increase of the number of probing points in the measurement domain in order not to loose potential information.

Glycerol-water mixtures are widely adopted in the literature as matching media for MWT systems [58; 59; 60; 144]. In this work, 90% glycerol + 10% water ($\epsilon_r \approx 14 - 13j$ at 1.5 GHz) solution, and pure glycerol ($\epsilon_r \approx 9 - 7j$ at 1.5 GHz) were used to test the developed MWT system. The two liquids will be hereafter referred as *Glycerol 90* and *Glycerol 100* respectively. The adoption of two different immersion liquids is justified in light of the different antennas that were available to us during the project. In particular, as reported in the following section, different antennas were adopted when collaborating either with Politecnico di Torino or King's College London. Due to space constraints in the axillary region, larger antennas (i.e., *Monopole A*, referring to Sec. 5.2.3) must be positioned further from the body, which makes the adoption of less lossy liquids (Glycerol 100 instead of Glycerol 90) necessary to minimise signal attenuation.

Regarding the choice of the frequency bandwidth, previous numerical studies [56] for breast MWT showed that reconstruction accuracy and stability are enhanced when performing a low-frequency reconstruction (e.g., 0.5 GHz) as a prior step to reconstructing data at higher frequencies. The studies presented in this chapter are conducted in the wide band between 0.5 and 2.5 GHz.

The choice of the smaller frequency is related to the minimum acceptable resolution (i.e., $\lambda/4 \approx 33mm$ in *Glycerol 90* and $\lambda/4 \approx 37mm$ in *Glycerol 100*, at 0.5 GHz), while the choice of the maximum frequency is constrained by the maximum number of antennas that could face the axillary region: the canonically used antenna spacing to maximise the amount of retrievable information without redundancies is $\overline{A_i A_{i+1}} = \lambda/2$. This topic will be further discussed in Sec. 5.5.

5.2.3 Antennas available to the study

Monopole antennas were tested due to their omnidirectional radiation patterns (in the plane orthogonal to the antenna plane), which represent an advantage as they are best modeled by point sources as the ones used in the forward model adopted in this thesis. The following antennas were tested due to their availability in the laboratory at the time of the assessment:

Monopole A is a wideband monopole antenna, which has already been tested for brain stroke detection at Politecnico di Torino [144]. The antenna (Fig. 5.5 (a)) is printed on a standard FR4 dielectric substrate (size 1.6mm x 30mm x 38mm). The top side of the antenna consists of a transmission line with a double-stub matching circuit and a triangular shaped radiating part. The bottom side is made of a ground plane that terminates close to the beginning of the radiating triangle. This antenna was tested in *Glycerol 100* for the numerical assessments presented in Sec. 5.4 and Sec. 5.5, and for the experimental assessment of the application presented in Sec. 5.6. Its reflection coefficient, measured in *Glycerol 100* is reported in Fig. 5.5 (b): the matching is always below -10 dB in the 1.1-3.0 GHz frequency band, even though it was used at 0.8 GHz. Additionally it has been shown that working outside the main resonance of the antenna (i.e., in an almost "flat region" of the $S11$ plot in Fig. 5.5 (b)) can aid tomographic reconstruction [144]. It is also reported that the oscillations of the measured $S11$ are due to the presence of a connector that was placed between the two coaxial cables, used in series to connect the antenna to the VNA (given the presence of the immersion liquid, the use of two cables allows to protect the electronic equipment and to ease VNA calibration).

Monopole B is a wideband pear-shaped patch monopole antenna, which was originally proposed in [145], and has been experimentally tested in King's College London for brain MWT [60], providing good results in brain stroke detection and classification. The antenna (represented in Fig. 5.6 (a)) is printed on an FR4 substrate with size 18.3mm x 28.4mm.

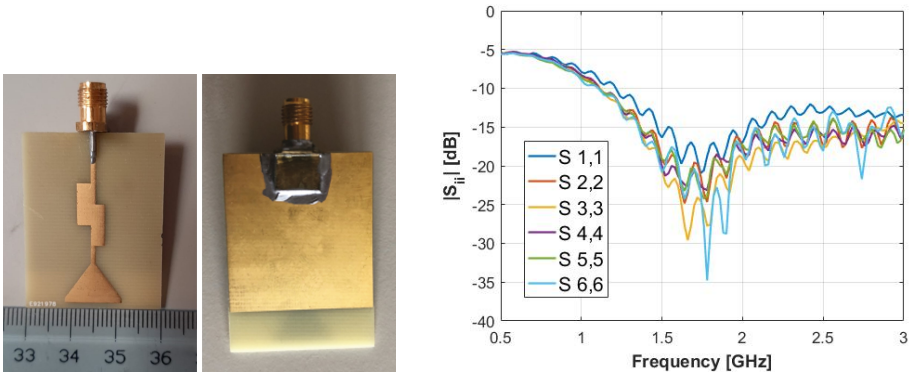

(a) (b)

Figure 5.5: *Monopole A*: first wideband monopole antenna used to test axillary MWT. **(a)** Front (left) and rear (right) view of the antenna. **(b)** S_{11} of 6 *Monopole A* antennas measured in pure glycerol. The antenna was originally proposed for medical MWT applications in [144].

The antenna was tested in *Glycerol 90*, and adopted for the numerical analyses in Sec. 5.7. Its reflection coefficient (simulated in *Glycerol 90*) is reported in Fig. 5.6 (b): the matching is always below -10 dB over the 0.8-2.5 GHz frequency band.

5.2.4 Imaging algorithm

To solve the nonlinear inverse ElectroMagnetic (EM) scattering problem, the general framework of the Distorted Born Iterative Method (DBIM) [54] (for a comprehensive description, see Sec. 2.2.1), combined with the Two-step Iterative Shrinkage/Thresholding (TwIST) algorithm [65] was adopted. The DBIM-TwIST framework was originally proposed for 2D breast MWI [56], and experimentally tested in [58; 60].

To solve the forward problem, a 2D implementation of the Finite-Difference Time-Domain (FDTD) EM-solver with a Convolutional Perfectly Matched Layer (CPML) boundary condition was used at each DBIM iteration. The 2D-FDTD simulation is excited by point sources with a wideband Gaussian pulse in a Transverse Magnetic (TM) modes (i.e.,

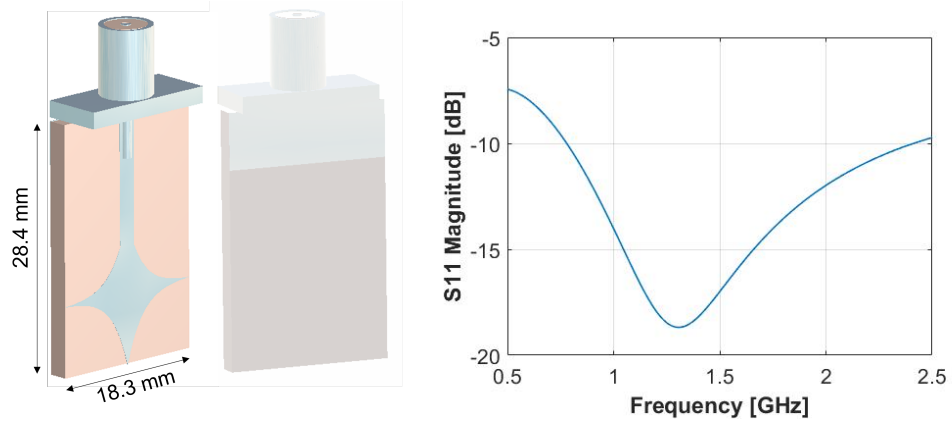

(a) (b)

Figure 5.6: *Monopole B*: second wideband monopole antenna used to test axillary microwave tomography. **(a)** Front (left) and rear (right) rendering views of the antenna. **(b)** S_{11} of the antenna simulated in 90% glycerol-water mixture. The antenna was originally proposed in [145]

the E-field is parallel to $\bar{z}$), centered at the resonance frequency of the antenna. Hence, only one component of E-field (E_z) is modeled. The 2D-FDTD algorithm implementation is described in [62].

The data calibration was performed using the methodology proposed in [66] (described in Sec. 2.2.1.4), considering - in most of the cases - the axillary model without any ALN as a reference object for calibration. The adoption of such calibration object would be unfeasible in real practice, but it was found convenient as a first approach. Additionally, it must be noted that the calibration object used in [66] is very similar to the imaged object, which justifies the adoption of an anatomically complex reference object for this work. The stability of DBIM to changes in the shape of the calibration objects is discussed in Sec. 5.7.

5.3 Effect of varying prior information in axillary 2D microwave tomography

In this section, the imaging performance of MWT for the detection and dielectric properties estimation of ALNs was assessed using a 2D version of the MWT system proposed in Sec. 5.2. In particular, the present section aims to: (i) study if DBIM can detect and estimate the dielectric properties of an ALN when prior knowledge of surrounding tissues is available; (ii) study the robustness of the algorithm to uncertainties/errors in the prior information of surrounding tissues, particularly muscle dielectric properties and its position. It is noted that a similar study was performed in [146] to quantify the impact of errors in prior information on image quality in the case of breast MWT.

As this is the first assessment of the application, the study was conducted in ideal conditions, i.e., using the same 2D-FDTD EM-solver for the generation of the data ("measurements") and for the resolution of the forward problem in the imaging algorithm ("modelling"), hence minimizing the measurement and modelling mismatches.

5.3.1 Methodology

In this study, a 2D MWT simulation scenario was considered to collect data (S-parameters) illuminating an axial slice of the anthropomorphic axillary model (MTA model referring to Sec. 5.2). A circular ALN (radius of 5mm) was included in the model. The anatomy and the dielectric properties (at 1.5 GHz) of the axillary model are shown in Fig. 5.7.

The setup is represented in Fig. 5.7, and considers eight antennas facing the axillary region in a quarter-circular array configuration. Antennas are point sources that generate wide-band Gaussian pulses centered at 1.5 GHz in a TM configuration (i.e. the E-field is perpendicular to the 2D axillary model), and are immersed in *Glycerol 90*, with complex permittivity $\epsilon_r = 14.3 - 13.2j$ at 1.5 GHz. Simulation data were produced using the finite-

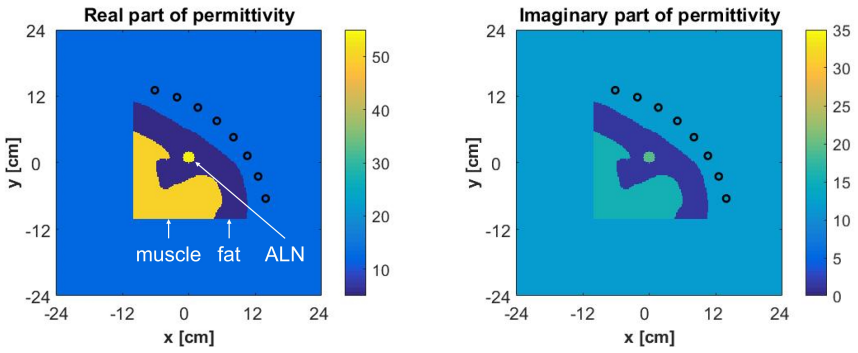

(a) (b)

Figure 5.7: 2D tomographic setup used to assess axillary microwave tomography: 8 point-source antennas (black circles) are placed in a quarter-circle configuration around the axillary region, which is composed of three tissues: fat, muscle, and axillary lymph node (ALN). The figure colors indicate the complex permittivity of axillary tissues at 1.5 GHz. **(a)** Real part of permittivity, **(b)** imaginary part of permittivity.

difference time-domain (FDTD) EM-solver with a Convolutional Perfectly Matched Layer (CPML) boundary condition, using a 0.5mm x 0.5mm mesh size. The E-field was sampled at the antenna locations in 11 equally-spaced frequency points covering the 0.5-2.5 GHz frequency band.

To solve the nonlinear inverse EM scattering problem, the DBIM-TwIST was adopted. The EM-solver used by the inversion algorithm is the same FDTD implementation used for the generation of the data. It should be noted that, to avoid the so called "inverse crime", a 2mm x 2mm mesh size was used, which differs from the size of the mesh used for data generation. Data were calibrated, as proposed in [66] (Sec. 2.2.1.4), considering the axillary model without any ALN as a reference scenario for calibration.

A frequency hopping approach was used for image reconstruction. Six equally-spaced frequency points between 0.5 and 1.5 GHz were considered, and 50 DBIM-TwIST iterations were performed at each frequency. In order to study the impact of varying prior information on imaging results, different heterogeneous dielectric maps were assigned as the *initial guess* of the DBIM algorithm at 0.5 GHz.

The performances of DBIM-TwIST in detecting ALNs were assessed by analysing its robustness to errors in the prior information. Firstly, it was investigated if DBIM can detect and estimate the ALN position and properties. To do so, the *initial guess* was defined as an heterogeneous dielectric map, representing the investigated model without the target. This case represents the ideal case, where all the axillary tissues (except the target) are known *a priori*. Secondly, the robustness to errors in the *initial guess* was evaluated introducing errors in the initial estimation of (i) dielectric properties of the axillary tissues (Sec. 5.3.2.1), (ii) muscle/fat interface position (Sec. 5.3.2.2), and (iii) both dielectric properties and muscle/fat interface position.

5.3.2 Results

Fig. 5.8 presents the imaging results for the benchmark case, where the *initial guess* represents the exact anatomy and dielectric properties of the tissues surrounding the ALN. It can be observed that the ALN is detected in its correct position, with good estimation of the real part of permittivity, and a slight underestimation of the imaginary part of permittivity.

5.3.2.1 Robustness to errors in dielectric properties

In order to study the effect of errors in the initial estimation of the background dielectric properties, the dielectric properties of fat were perturbed in the range between -30% and +100%, and the dielectric properties of muscle were perturbed by $\pm$30%. It should be noted that errors were not introduced in the permittivity of the immersion liquid, as this is not patient-dependent. Fig. 5.9 (a, b) reports the reconstruction results for the case where the dielectric properties of both fat and muscle are overestimated by +30%. The images show that, despite the introduced error in the dielectric properties prior knowledge, the ALN is detected in its correct position, and no noticeable differences are visible when comparing these results with the results obtained in the ideal case (Fig. 5.8), where there are

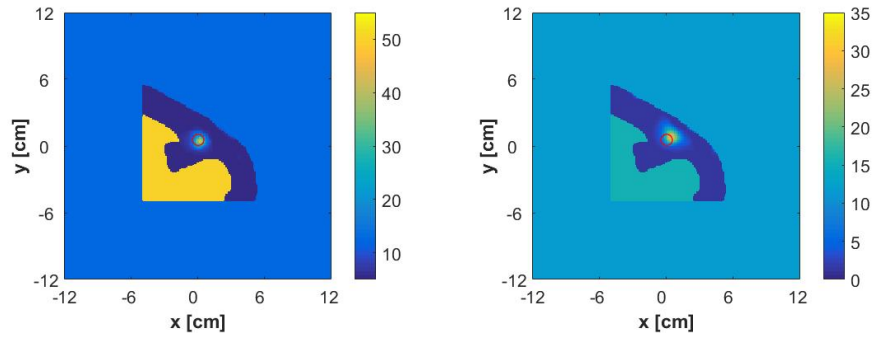

(a) (b)

Figure 5.8: Ideal case: reconstructed complex permittivity at frequency = 1.5 GHz for the case where the *initial guess* represents the exact anatomy and dielectric properties of the tissues surrounding the ALN. The inner red circle shows the actual position of the ALN. **(a)** Real part of permittivity; **(b)** Imaginary part of permittivity. Reconstruction strategy: frequency hopping between 0.5, 0.7, 0.9, 1.1, 1.3 and 1.5 GHz.

no errors in the *initial guess*. Similar results were observed when initially underestimating the dielectric properties of fat and muscle tissue by -30% (data not shown).

To further investigate the robustness of the algorithm to errors in the prior estimation of dielectric properties, the dielectric properties of fat were overestimated by +100%, and the dielectric properties of muscle were underestimated by -30%. Fig. 5.9 (c, d) reports the reconstruction results. The images show that the ALN is detected in its correct position, but with a reduced contrast compared to the true one, which is particularly evident in the imaginary part of the permittivity. Similar results were obtained when introducing a +100% error in fat and a +30% error in muscle dielectric properties. These can be considered good results as it is reasonable to assume the last two described cases as “worst case scenarios”. In light of the physiological variability of dielectric properties of biological tissues among individuals, errors in dielectric properties higher than 100% for fat and 30% for muscle tissues are not expected.

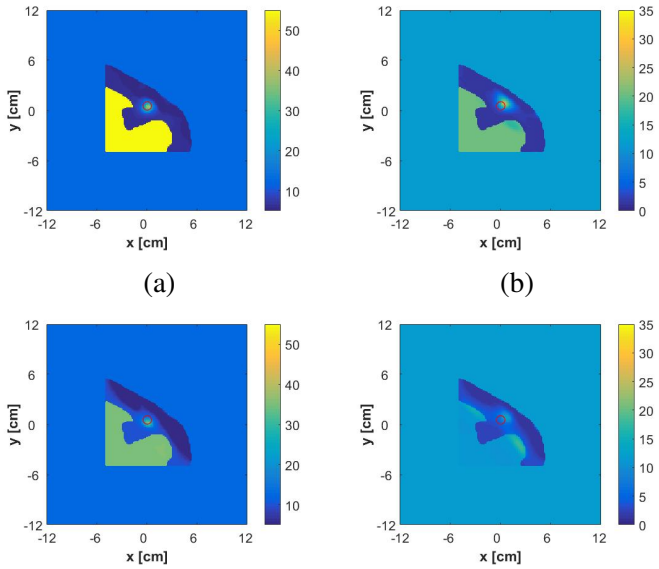

Figure 5.9: Reconstructed complex permittivity at frequency 1.5 GHz for the cases where errors are introduced in the *initial guess* of the dielectric properties of fat and muscle tissues. The error in the initial estimation of dielectric properties is **(a, b)** +30% for both fat and muscle; **(c, d):** -30% for muscle and +100% for fat. The red circle shows the actual position of the ALN. **Left column:** Real part of permittivity; **Right column:** Imaginary part of permittivity. Reconstruction strategy: frequency hopping between 0.5, 0.7, 0.9, 1.1, 1.3 and 1.5 GHz.

5.3.2.2 Robustness to errors in fat/muscle interface

In order to study the effect of errors in the initial estimation of the position of fat/muscle interface, the interface was translated along the vectors represented in Fig. 5.10 (left side). As a result, four different *initial guesses* were considered, corresponding to the following translation vectors with respect to the true position of the muscle: -14mm, -7mm, +7mm, +14mm; where a negative translation indicates a movement towards lower x and y coordinates in Fig. 5.10 (larger fat region in the *initial guess*), and a positive translation indicates a movement towards larger x and y coordinates in Fig. 5.10 (smaller fat region in the *initial guess*).

Fig. 5.10 reports the results for the four cases. Fig. 5.10 (c,d) and Fig. 5.10 (e,f) suggest that the detection of the ALN is still clear when translating the fat/muscle interface by $\pm 7mm$. The image quality deteriorates when the error in prior information is $\pm 14mm$. Fig 5.10 (a, b) show that the ALN can be obscured by the muscle - based on the imaginary part - when the *initial guess* of the fat/muscle interface is translated by -14mm with respect to its true position. Fig. 5.10 (g,h) show that the ALN position is not well estimated in the case where the fat/muscle interface is initially translated by +14mm with respect to its true position.

5.3.2.3 Robustness to errors in both dielectric properties and fat/muscle interface

As a final test, the effect of errors in the initial estimation of the position of fat/muscle interface was studied when an error in the initial estimation of dielectric properties simultaneously occurs. To do so, the same four cases studied in Fig. 5.10 were considered, and a +30% error to the initial estimation of dielectric proprieties was added. As in the previous paragraph, the following translations were applied to the *initial guess* of the fat/muscle interface with the respect to its true position: -14mm, -7mm, +7mm, +14mm. Fig. 5.11 reports the results for the four cases. If comparing Fig. 5.11 to Fig. 5.10, it can be noticed that no significant differences is observed when adding a +30% error in the initial estimation of dielectric properties. Similar results were observed for the cases where a -30% error was introduced in the *initial guess* of dielectric properties. These results suggest that - even when errors in fat/muscle interface occur - errors in prior estimation dielectric properties ($\pm 30\%$) do not affect the overall quality of the reconstructed image.

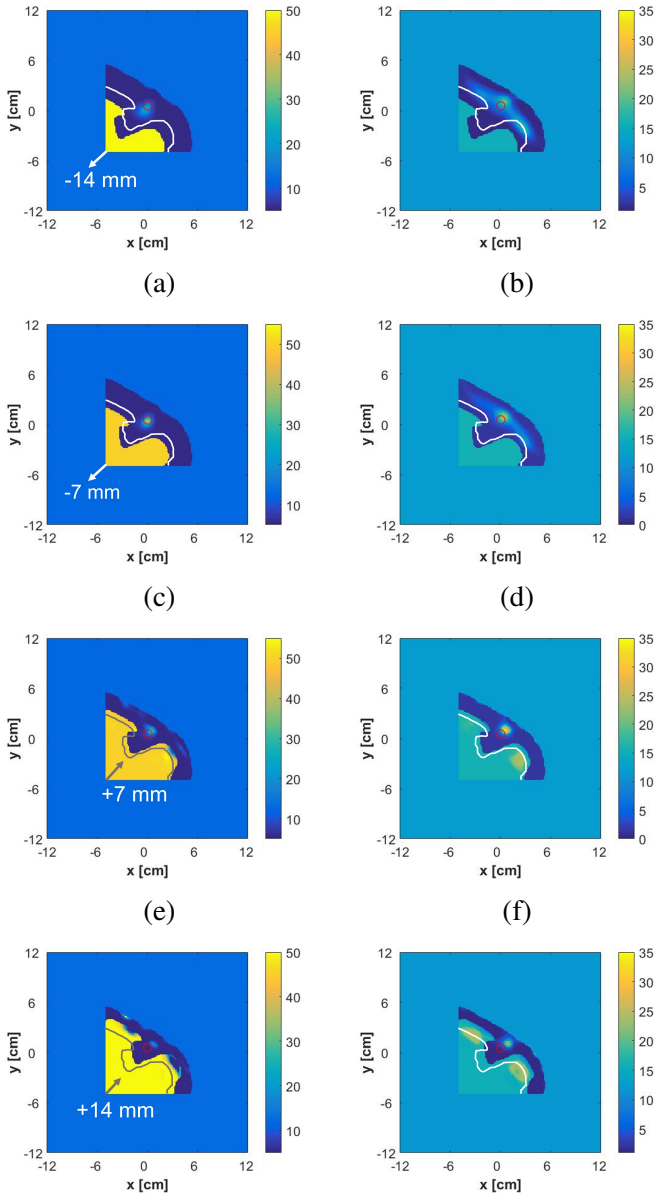

Figure 5.10: Reconstructed complex permittivity at 1.5 GHz for the cases where the position of the *initial guess* of the fat/muscle interface is translated with respect to its true position. **Left:** real part of permittivity; **right:** imaginary part of permittivity. The translation vector is indicated by the arrow. The direction of the translation vector bisects the first and third quadrants of the reference system. The modulus of the translation vector is: **(a), (b)** -14mm, **(c), (d)** -7mm; **(e), (f)** +7mm; **(g), (h)** +14mm. The white/grey line traces the true fat/muscle interface. The red circle shows the actual position of the ALN. Reconstruction strategy: frequency hopping between 0.5, 0.7, 0.9, 1.1, 1.3 and 1.5 GHz.

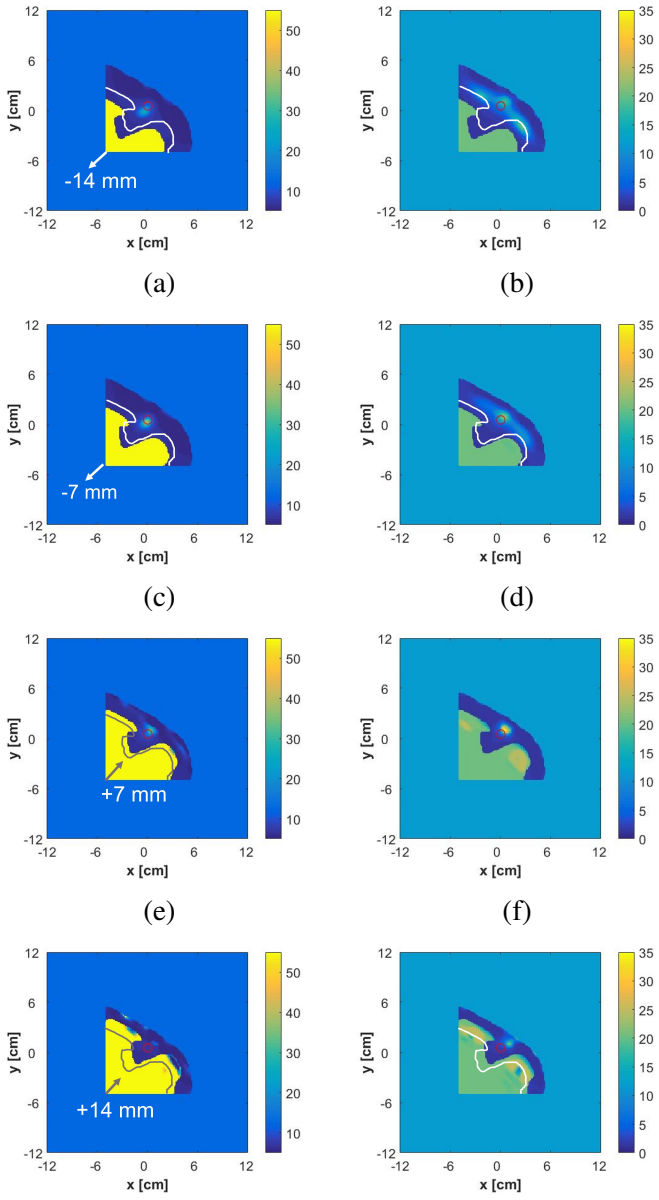

Figure 5.11: Reconstructed complex permittivity at frequency = 1.5 GHz for the cases where the errors in the *initial guess* involve both the dielectric properties of fat and muscle tissues and the position of the fat/muscle interface (translation with respect to its true position). The error in dielectric properties is a +30% overestimation for all cases. The error in fat/muscle interface position is indicated (for each case) by the translation vector on the left side of the image; the modulus of the translation vector is: **a, b** -14mm, **c, d** -7mm; **e, f** +7mm; **g, h** +14mm. The white/grey line traces the true fat/muscle interface. The red circle shows the actual position of the ALN. **Left:** real part of permittivity; **right:** imaginary part of permittivity. Reconstruction strategy: frequency hopping between 0.5, 0.7, 0.9, 1.1, 1.3 and 1.5 GHz.

5.4 Effect of limited angular view in axillary MWT

This section focuses on one of the main challenges posed by ALN MWI, namely the limited angular view available for probe placement when imaging the axillary region.

5.4.1 Methodology

In this study, the numerical homogeneous (H) axillary model (defined in Sec. 5.2.1) was considered, and a spherical ALN (radius = 8mm) was embedded in fat tissue. The model was immersed in *Glycerol 100*, and surrounded with 12 *Monopole A* probes (Sec. 5.2.3), as shown in Fig. 5.12. $N_A = 6$ probes (probes 1-6) were placed on the anatomically accessible side of the model (i.e., in front of the axillary region), while an extra set of 6 probes (probes 7-12) was intentionally placed facing the two flat back-sides of the model, aiming to obtain a benchmark result to qualitatively assess the effects of having limited angular domain, which is a major constraint in ALN MWI. The position of probes 1-6 is given by: $O_A(-21mm, -1mm, \bar{z})$; $\rho = [136, 136, 136, 136, 136, 136, 136]$; $\Delta\phi = 15°$. The resulting distance between adjacent antennas is $\overline{A_i A_{i+1}} = 36mm$. The average ($\pm$ standard deviation) antenna-body distance is 23*mm* ($\pm 6mm$), for antennas 1-6. Probes 7-12 are spaced 36*mm*, with constant antenna-phantom distance equal to 23*mm*.

Data (i.e., scattering parameters) were computed in the 0.8-2.5 GHz frequency band, using full wave simulation in CST software, discretising the space using an hexaedral mesh, ensuring that each voxel side size was at maximum $\lambda/20$.

Prior knowledge about the morphology and position of torso (fat tissue) was assumed to be available. According to this information, the *initial guess* (i.e., the first estimate of the background given as input to the DBIM algorithm) was defined as a 2D cross-section of the homogeneous fatty axillary region. The reconstruction of the dielectric profile was limited to the voxels contained in the body (at $z = \bar{z}$).

Two different subsets of antennas were alternatively used for image reconstruction: (i)

antennas 1-12 (i.e., all the antennas), and (ii) antennas 1-6 (i.e., only those on the anatomically accessible side of the axillary model).

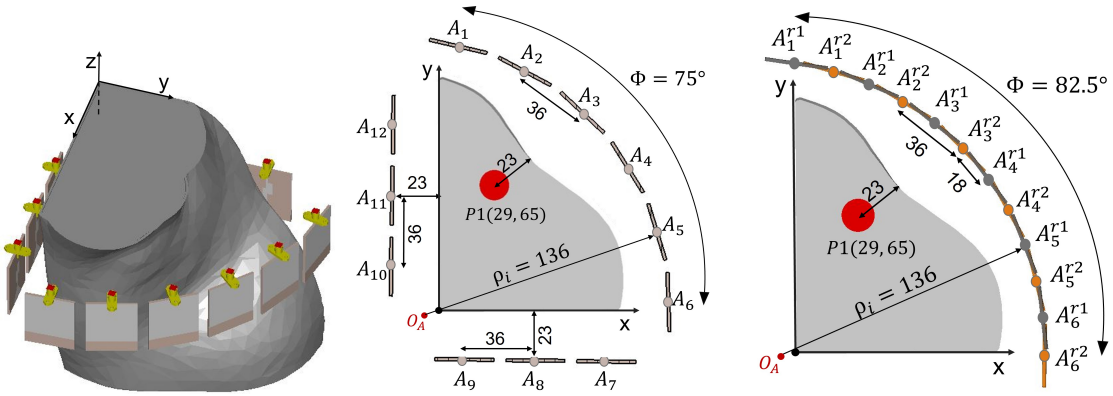

(a) (b) (c)

Figure 5.12: **(a, b)** Setup used (Sec. 5.4) to assess the influence of having limited angular view in axillary MWT: 12 monopole antennas are placed around the homogeneous (H) axillary model. The probes are placed not only in front of the axillary region, but also - in a non-realistic manner - on the back side of the phantom, enlarging the imaging domain. **(a)** Rendering view of the setup. **(b)** Cross-sectional view of the setup at the level of the target. **(c)** Setup used (Sec. 5.5) to assess the effect of performing two-step angular measurements: the representation shows the 12 probing points in front of the axilla, obtained as a results of the two rotational position assumed by the 6-antenna set. The apices *r1* and *r2* indicate the two rotational positions assumed by the antennas. Distances are reported in millimeters.

5.4.2 Results

Images were reconstructed using frequency hopping between 0.8, 0.9 and 1.0 GHz (the dielectric map reconstructed at the first frequency is used as the *initial guess* to the second frequency and so on), with 25 DBIM iterations per frequency point, in a total of 75 iterations. The choice of the hopping frequencies is later justified in light of the experimental results obtained in Sec. 5.6.

Fig. 5.13 reports the images reconstructed at the last hopping frequency (1.0 GHz) for the two analysed cases. It can be observed that the target is detected in its correct position

in both real and imaginary parts of the permittivity, when the signals collected by all the 12 antennas are used. The target detection is more challenging in the case where only the 6 antennas facing the axillary region were considered. As expected, limiting the illumination angle (and the number of probes) affects target detection, which highlights the challenges of the application.

It is worth noticing that the proposed algorithm fails to estimate the target dielectric properties within acceptable error (in the real part, the estimated target permittivity is approximately 1.05 times higher than fat permittivity, while it should be approximately 10 times higher). It is noted that, a good ALN permittivity estimation was obtained (Sec. 5.3) when using the same 2D-FDTD in the simulation (data generation) and imaging algorithm, which suggests that the failure to estimate ALN properties may be due to the *modelling errors*. It is also reported that in experimental studies on brain MWT [60], the same DBIM-TwIST algorithm was able to differentiate targets with different dielectric properties. It is hence suspected that the *modelling errors* in axillary MWT are due to: (i) the small size of the target over the z-axis which - after calibration - may result in a reduced response of the target with respect to other organs, translating in an underestimation of the permittivity; (ii) the non-invariant shape of the axilla over the z-axis (as is almost the case for the brain).

5.5 Measurement domain sampling in axillary MWT

This section proposes a method to maximise the useful retrievable information in axillary MWT, taking into account the practical constraints given by the morphology of the axillary region (limited space for probe and cable placement) and by the instrumentation available for experimental assessment (6-port VNA). The method presented in this section relies on increasing the number of probing points in the measurement domain by performing consecutive measurements, varying the angular position of the antenna set.

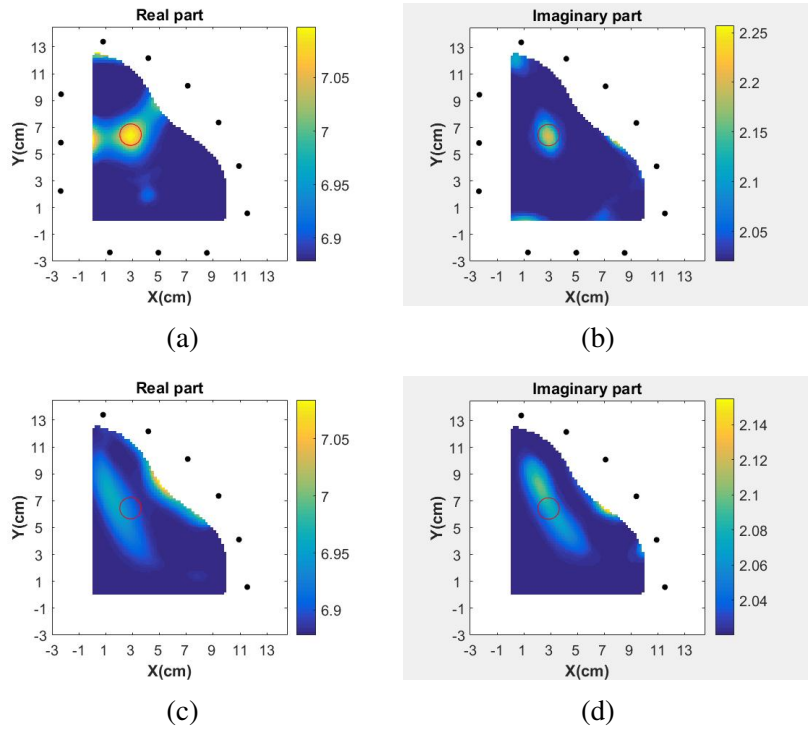

Figure 5.13: The effect of having limited angular view in axillary microwave tomography: comparison between imaging results obtained considering data retrieved with **(a, b)** 12 antennas, placed all around the model, and **(c, d)** only the 6 antennas, facing the axillary region. **(Left)** Real part, and **(right)** imaginary part of relative permittivity. Black dots represent the probes. Reconstruction strategy: frequency hopping between 0.8, 0.9 and 1.0 GHz.

5.5.1 Methodology

To pursue such investigation, the same setup used in Sec. 5.4 (Fig. 5.12) was adopted - antennas 7-12 were excluded. In summary, the setup consists of the H phantom (with a spherical 8mm radius ALN), immersed in *Glycerol 100*, and surrounded by 6 *Monopole A* probes spaced by 30mm from each other, facing the axillary region.

Two dataset were generated in the 0.8-2.5 GHz frequency band, using full wave simulation (CST):

1. the first dataset is a 6-by-6 scattering matrix, computed at the 6 probing points indi-

cated by antennas 1-6 in Fig. 5.12;

2. the second dataset comprises the measurements collected in two consecutive steps, i.e., rotating the 6-antenna set by $\Delta\phi/2$ between subsequent measurements. The resulting 12 probing points (6-antenna set in 2 rotational positions) are illustrated in Fig. 5.12 (c), which highlights (different colors) the two rotational positions assumed by the 6-antenna set. As a result, two 6-by-6 scattering matrices were obtained and merged in a single 12-by-12 matrix which - for each frequency - is defined as:

$$S(i,j) = \begin{cases} 0, & \text{if } i+j \text{ is odd} \\ S^{Ang1}(\frac{i+1}{2}, \frac{j+1}{2}), & \text{if } i \text{ and } j \text{ are odd} \\ S^{Ang2}(\frac{i}{2}, \frac{j}{2}), & \text{if } i \text{ and } j \text{ are even} \end{cases}$$

where $i \in \{1, 2, ..., 12\}$, $j \in \{1, 2, ..., 12\}$; $S^{Ang_1}(i,j)$ and $S^{Ang_2}(i,j)$ are the 6-by-6 scattering matrices measured when illuminating the axillary model with the antenna set in the first and second angular position respectively.

Prior knowledge about the morphology and position of torso (fat tissue) was assumed to be available, meaning that the *initial guess* was defined as a 2D cross-section of the homogeneous fatty axillary region. The imaging domain included only the voxels contained in the body (at $z = \bar{z}$), and no immersion liquid.

5.5.2 Results

Fig. 5.14 presents the imaging results obtained for both dataset, using independent frequency reconstruction at 9 equally spaced frequency points between 0.8 and 2.4 GHz, with 25 DBIM-TwIST iterations per frequency point. Fig. 5.14 (a-b) presents the results for the dataset obtained with one illumination angle; while Fig. 5.14 (c-d) presents the results for the dataset obtained with two illumination angles.

The results can be analysed considering three different frequency bands: (i) in the 0.8-1.0 GHz band, the target is detected in its correct position when considering either one or two illumination angles for data acquisition; a slight improvement in the spatial resolution is observed when considering two illumination angles; it should also be noted that the target localisation is worse in the imaginary part compared to the real part of permittivity; (ii) in the 1.1-1.9 GHz band, the target detection is masked by the presence of clutters, for both dataset; (iii) in the 2.0-2.5 GHz band, the target is detected in its correct position when performing measurements from two different illumination angles, with a better estimation of the position in the real part compared to the imaginary part of the permittivity; when considering only one illumination angle, artifacts arise, hampering the target detection.

These results should be interpreted in light of the spacing between antennas (equal to 36*mm*) which corresponds to the commonly used $\lambda/2$ antenna spacing at 1.7 GHz. Hence, it is expected that increasing the number of probing points in the measurement domain aids the reconstruction for $f > 1.7GHz$, which is confirmed by the noticeable improvement in the results obtained in the 2.0-2.5 GHz band. Regarding the 0.8-1.0 GHz frequency band, the improvement in the imaging results can be justified considering that the optimal probe spacing depends on several factors, including the extension of the measurement domain [147], which is limited to an 82.5° angle (considering two rotational positions of the antennas). Regarding the 1.1-1.9 GHz band, it can be concluded that such band is not suitable for imaging with the current setup configuration. This result can be due to the fact that the model employed by the imaging algorithm (i.e., the 2D-FDTD solver that runs at each DBIM iteration) does not accurately replicate the antenna radiation pattern in the neighborhood of its resonance frequency (approximately 1.7 GHz), as antennas are modeled as point sources. Difficulties in modelling the antenna's behaviour around the resonance frequency were also indicated as a cause of worse reconstruction results in [144].

Besides a single frequency analysis, this section also reports the imaging results obtained using frequency hopping between 0.8, 0.9, and 1.0 GHz (Fig. 5.15), with 25 DBIM

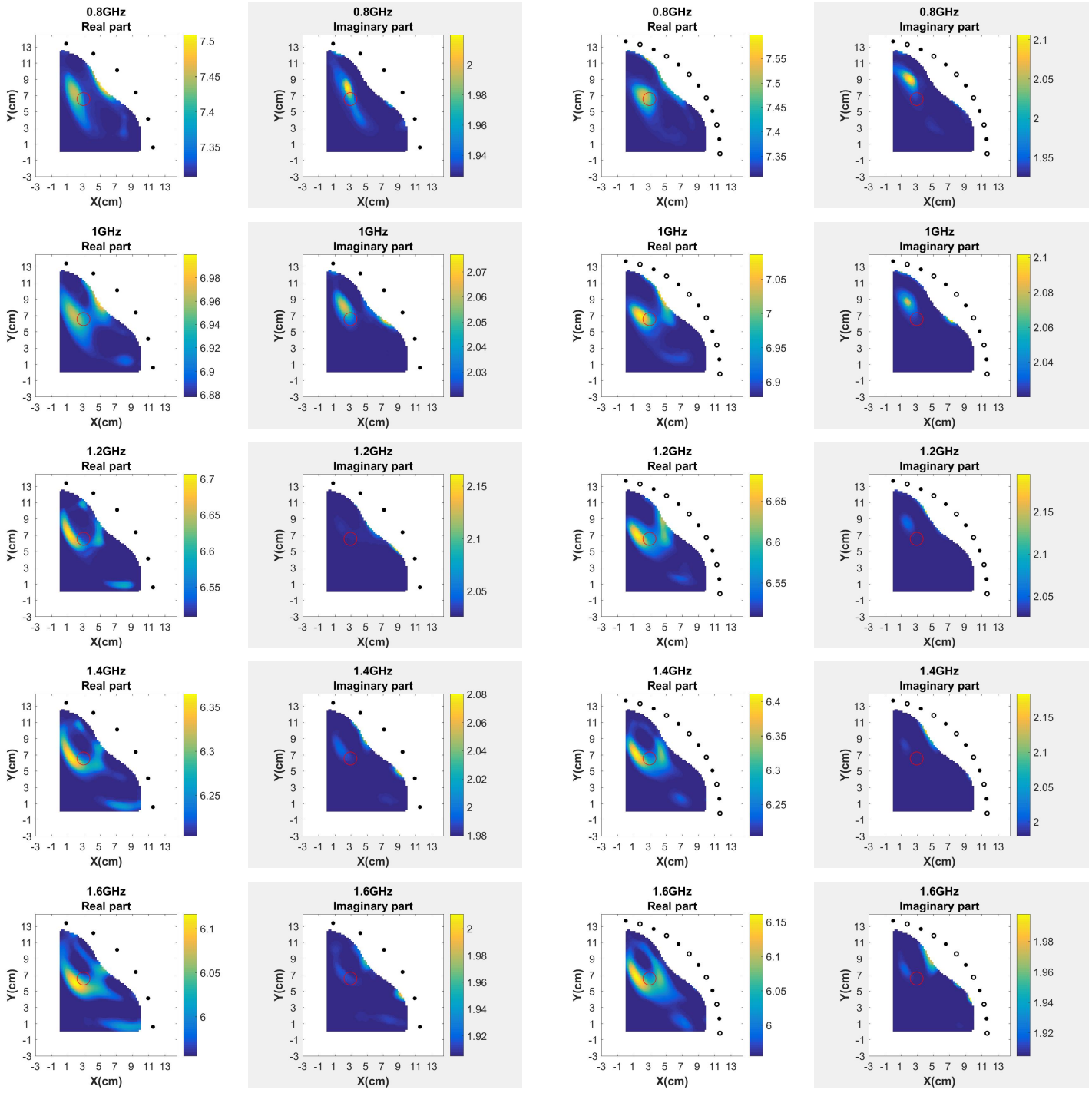

(a) (b) (c) (d)

Figure 5.14: The effect of increasing the number of probing points in the measurement domain by performing two-steps angular measurements. A comparison between complex permittivities reconstructed using: **(a-b)** 6 antennas in a single angular position; **(c-d)** 6 antennas in two different angular position (in a total of 12 angular positions). Reconstruction approach: independent frequencies reconstruction.

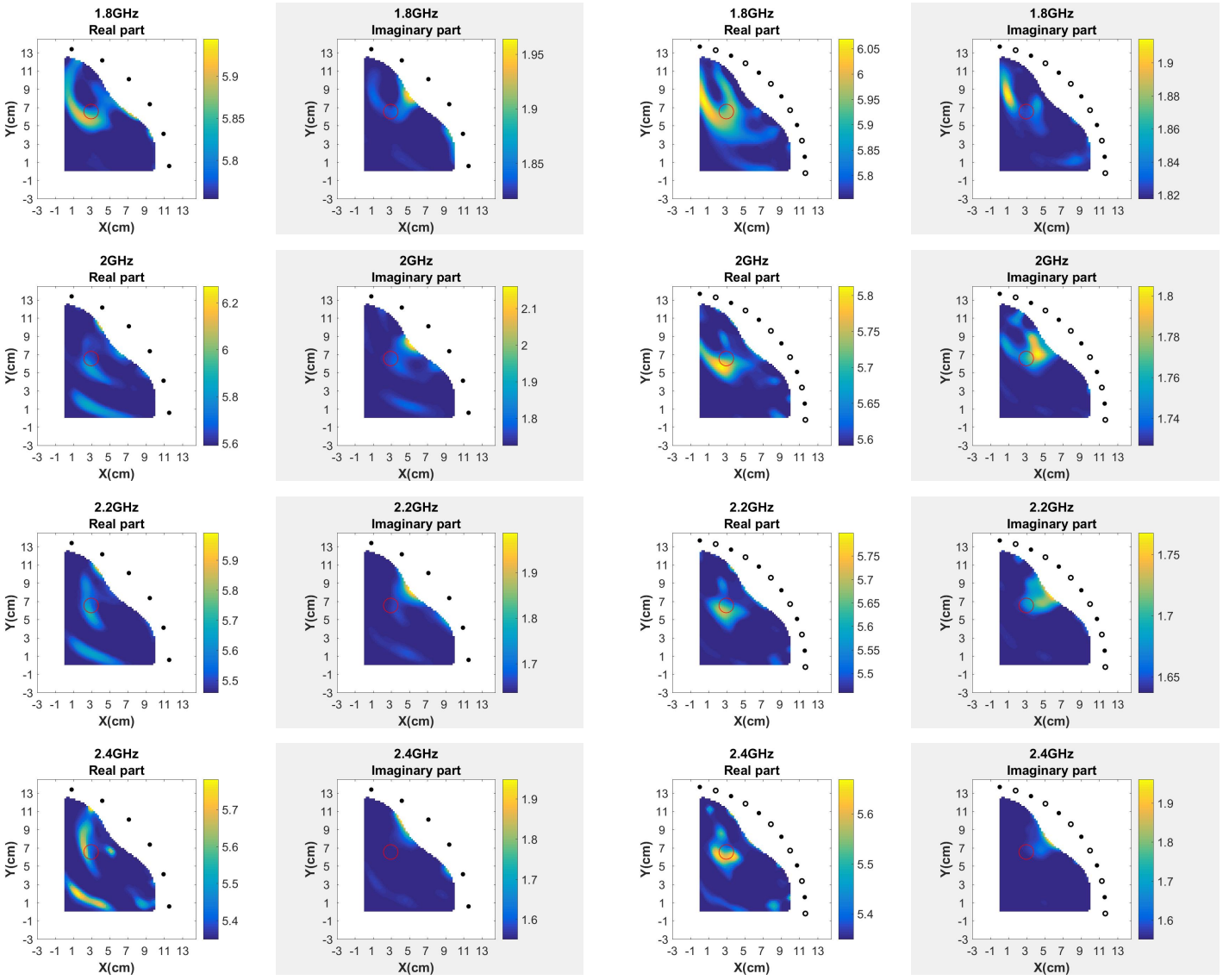

(e) (f) (g) (h)

Figure 5.14: (*Continued*) The effect of increasing the number of probing points in the measurement domain by performing two-steps angular measurements. A comparison between complex permittivities reconstructed using: **(a-b)** 6 antennas in a single angular position; **(c-d)** 6 antennas in two different angular position (in a total of 12 angular positions). Reconstruction approach: independent frequencies reconstruction.

iterations per frequency point, with the same approach used in Sec. 5.4. The reconstructed images show that - when acquiring data in two consecutive steps, rotating the antennas - the target detection significantly improves in the real part of permittivity, while a localization error (LE) of 26mm is observed in the imaginary part of permittivity (Fig. 5.15 (d)). Such error is probably part of the inaccuracies of the inversion process due to the mismatch between the model and the true system. Additionally, a comparison between Fig. 5.15 (d) and Fig. 5.13 (b) suggests that the LE may be due to the limited angular view. It is also reported that other studies in the literature [60] encountered more difficulties in reconstructing the imaginary part rather than the real part of permittivity. Regarding the significance of the LE, it is emphasised that LE = 26mm is deemed acceptable since 26mm (i) corresponds to 0.23 wavelengths (λ=123mm at 1.0 GHz, in fat tissue), and (ii) is comparable to the ALN diameter (16mm) in the analysed plane. In conclusion, these results suggest that performing measurements at two different angular positions of the antenna set is a good strategy to mitigate space limitations posed by axillary MWT, which motivated the adoption of such approach during the experimental assessment, presented in the following section.

5.6 Experimental assessment of axillary MWT

This section describes the experimental measurement campaign performed to test the axillary MWT system proposed in this thesis (generic description provided in Sec. 5.2), using anthropomorphic phantoms (main development described in Chapter 4) with increasing level of anatomical detail.

5.6.1 Methodology

The proposed experimental setup is illustrated in Fig. 5.16, and consists of a cylindrical acrylic tank (diameter $d = 400mm$) filled with *Glycerol 100*, where the axillary region

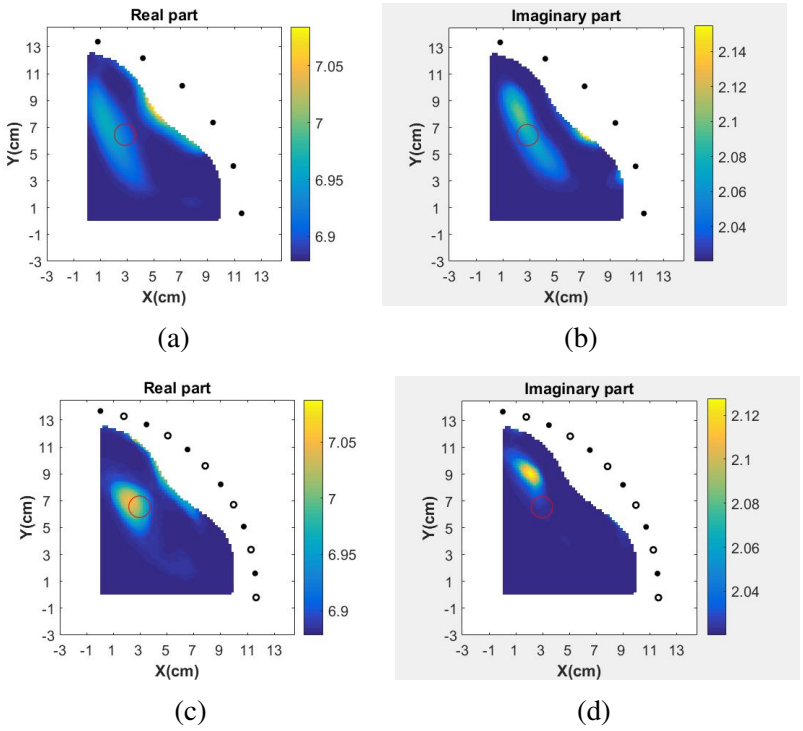

Figure 5.15: The effect of increasing the number of probing points in the measurement domain by performing two-steps angular measurements. A comparison between complex permittivities reconstructed using: **(a-b)** 6 antennas in a single angular position; **(c-d)** 6 antennas in two different angular position. Reconstruction approach: frequency hopping between 0.8, 0.9 and 1.0 GHz.

phantom was immersed, and surrounded by 6 *Monopole A* antennas. As mentioned in Sec. 5.5, given the practical issues related with the the use of more antennas (i.e., limited space in the axillary region, antenna size, and number of ports in the VNA) only 6 probes were used. Referring to the 2D polar coordinates defined in Sec. 5.2 (Fig. 5.3), the position of the antennas in $\bar{z}$ is given by: $O_A = (0, 0, \bar{z})$, $\rho = [135, 125, 115, 120, 125, 120]mm$ and $\Delta\phi = 15°$. Given the space constrains, efforts were made to minimize the antenna-body distance and to keep it as uniform as possible, across all antennas. The average ($\pm$ standard deviation) distance from the antennas to the phantom (at $z = \bar{z}$) is 21($\pm$3)mm (computed on 12 distances, as a result of the two illumination angles).

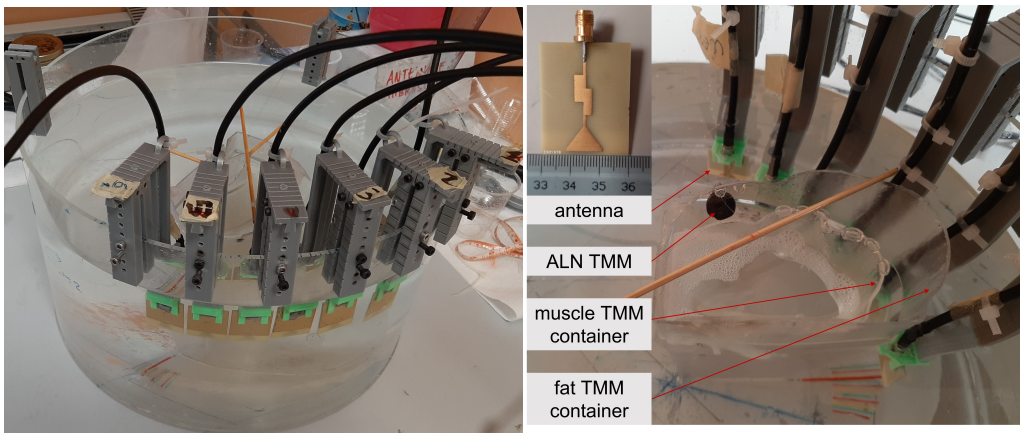

(a) (b)

Figure 5.16: Experimental setup used to assess axillary microwave tomography: in an acrylic tank, filled with *Glycerol 100*, 6 monopole antennas face the axillary region phantom, covering an angle $\Phi = 75\,\mathrm{deg}$. (a) External view of the tank and bottom side of the antennas, held in position with the 3D-printed supports; **(b)** multi-tissue-anthropomorphic (MTA) phantom surrounded by the antennas. The phantom is composed of three tissues: fat and muscle are containers filled with liquid tissue mimicking materials (TMMs), while the axillary lymph node (ALN) is made of a solid rubber TMM.

The physical phantoms tested in this study are 3D-printed version of the homogeneous (H), multi-tissue-simplified (MTS) and multi-tissue-anthropomorphic (MTA) models described in Sec. 5.2.1, filled with liquid tissue mimicking materials (TMMs) made of water, Triton X-100 and NaCl mixtures, as detailed in Sec. 4.2. As for the ALN TMM, this is made of a solidified mixture of polyurethane, carbon black, graphite, and acetone (fabrication described in Sec. 4.2). The ALN phantom was modeled as a spheroid target, with an equatorial diameter of 16mm and a polar diameter of 12mm, and was held in a stable position inside the fat TMM using a system of nylon wires tied on specific supports of the 3D-printed phantom parts. An ALN phantom and its supports are represented in Fig. 5.16 (b). Different ALN positions were combined with different levels of anatomical complexity, which resulted in five different phantom configurations:

1. H-P1: H-phantom with target in position $P1(29, 65, \bar{z})$, i.e. the same model used for

the numerical assessment in Sec. 5.4 and Sec. 5.5;

2. H-P2: H-phantom with target in position $P2(63, 44, \bar{z})$
3. MTS-P1: MTS-phantom with target in position $P1$
4. MTA-P1: MTA-phantom with target in position $P1$
5. MTA-P3: MTA-phantom with target in position $P3(56, 58, \bar{z})$

Data were acquired in the 0.8-2.5 GHz frequency band, using a Keysight M9804A VNA (maximum nominal dynamic range of 140 dB at 10 Hz IF bandwidth), with 50 Hz IF bandwidth and 13 dBm output power, which allowed for an effective dynamic range large enough to sense the target.

Prior knowledge about the morphology and position of torso and muscle was assumed to be available. The *initial guess* was defined as a 2D cross-section of the axillary region with all organs except the target. The imaging domain included only the voxels contained in the body (at $z = \bar{z}$).

5.6.2 Results

The response of ALN for the H-P1 phantom is reported in Fig. 5.17. The results show that the response of the ALN transmitted by the i-*th* probe to the j-*th* probe is approximately between -120dB and -100dB, which justifies the choice of a low IFBW (50 Hz) for the present experimental campaign.

Regarding imaging, single-frequency reconstructions were initially performed for all phantom configurations to assess the potential of each frequency, and compare the results with those obtained in then numerical assessment (Sec. 5.5). Once the best operating frequencies were identified, the results were computed using frequency hopping within the best-operating frequency band.

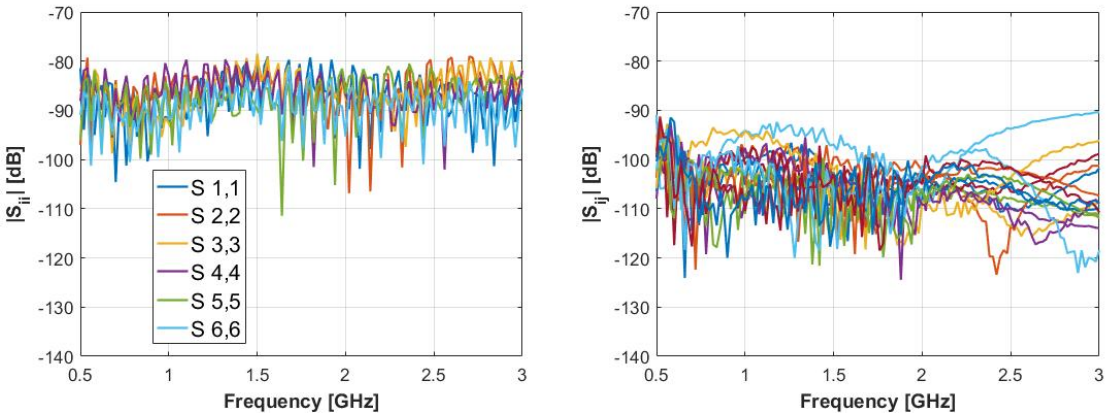

(a) (b)

Figure 5.17: Target response, computed as the difference between S-parameters measured in the presence and in the absence of the target, for the 6 antennas. Data refers to the phantom filled only with fat TMM. **(a)** Response in reflection; **(b)** response in transmission.

Fig. 5.18 presents single-frequency reconstructed images for the H-P1 phantom, at the following frequencies: [0.8, 0.9, 1.0, 1.1, 1.4, 1.7, 2.0, 2.3] GHz. It is observed that the ALN is detected between 0.8 and 1.0 GHz, while for frequencies higher than 1.0 GHz, the detection is hindered by clutter presence. These results are consistent with the corresponding numerical results (Fig. 5.14 (c-d)) in the 0.8-1.0 GHz band, but not in the 2.0-2.5 GHz band, which can be explained as image reconstruction is more unstable (hence more susceptible to noise presence) at higher frequencies [56]. It is also noticed that the real part is better reconstructed than the imaginary part, which had also been observed in previous studies that adopted the same DBIM-TwIST algorithm [60].

Once the optimum frequency range (0.8-1.0 GHz) is identified, image reconstruction was attempted using the information from multiple frequencies within that range. Images were reconstructed using a frequency hopping approach between 0.8, 0.9 and 1.0 GHz, with 25 DBIM-TwIST iterations at each frequency, in a total of 75 iterations. Fig. 5.19 presents the imaging results at the last hopping frequency (1.0 GHz) for the five phantom configurations tested. Regarding the H-P1 phantom, it is observed that the ALN is detected

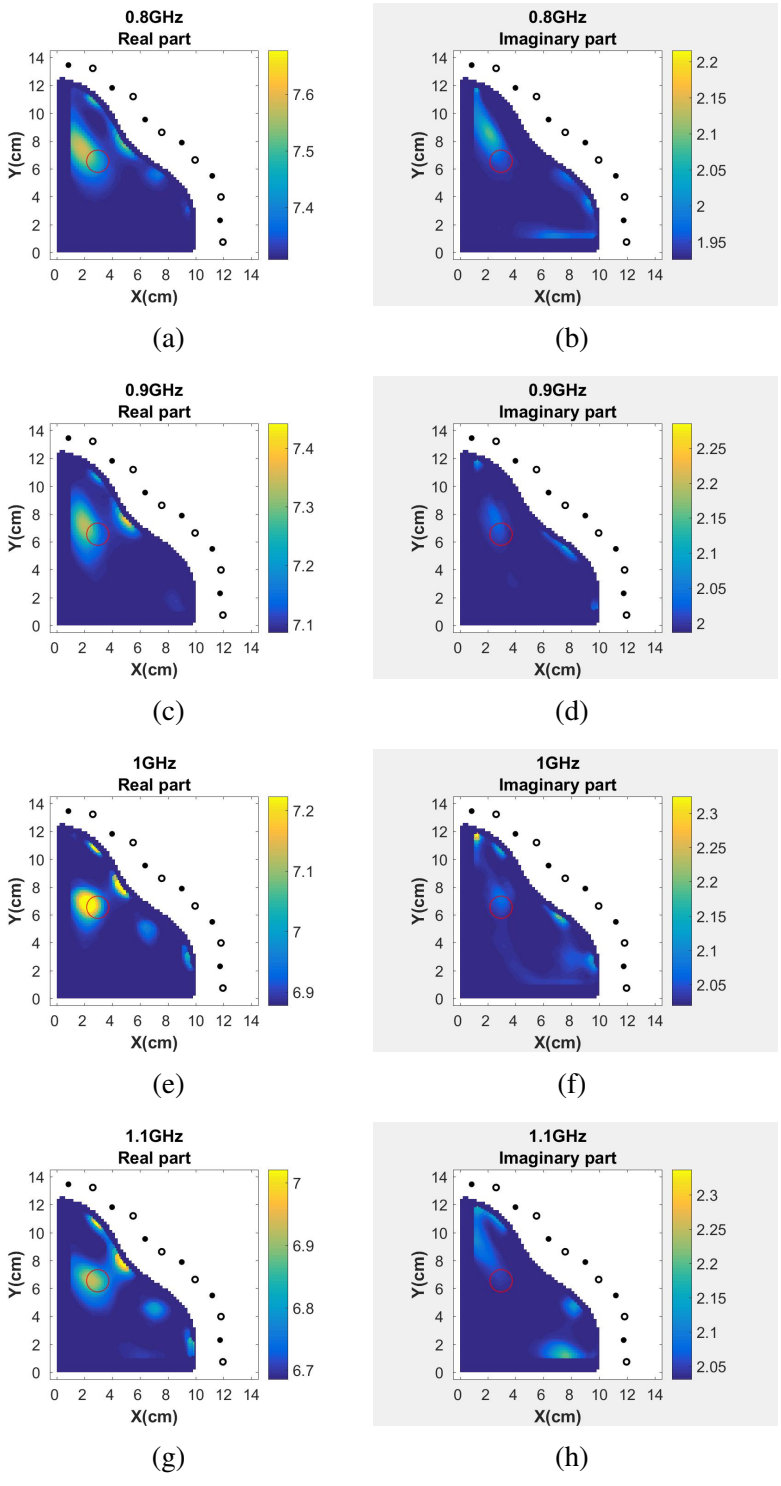

Figure 5.18: Experimental results obtained reconstructing images at different (independent) frequencies, using the homogeneous phantom whit target in position P1 (H-P1 phantom). **(a, b)** 0.8 GHz, **(c, d)** 0.9 GHz, **(e, f)** 1.0 GHz, **(e, f)** 1.1 GHz, **(g, h)**.

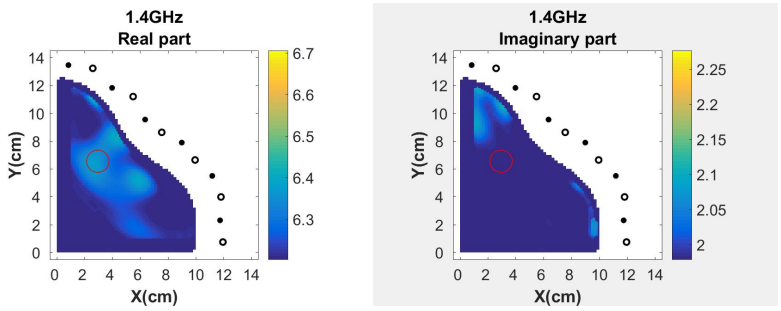

(i)

(j)

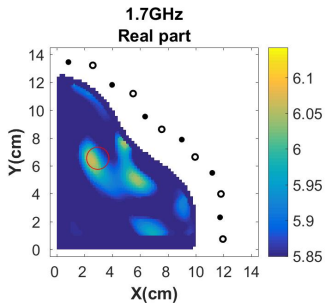

(k)

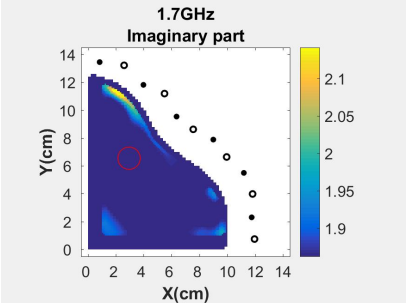

(l)

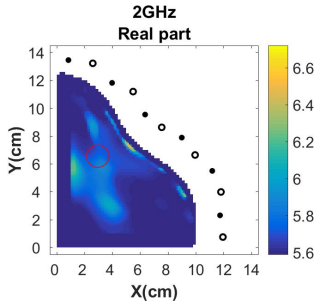

(m)

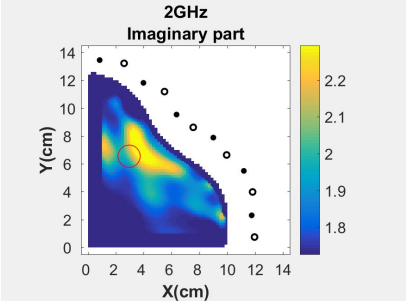

(n)

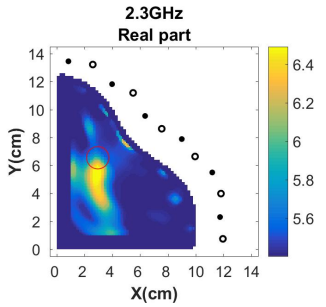

(o)

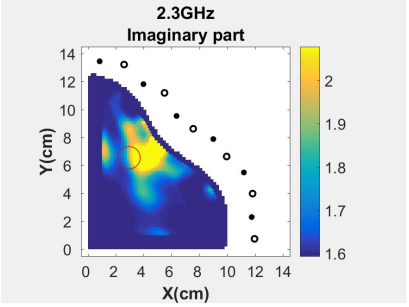

(p)

Figure 5.18: *(Continued)* Experimental results obtained reconstructing images at different (independent) frequencies, using the homogeneous phantom whit target in position P1 (H-P1 phantom). **(g, h)** 1.4 GHz, **(i, j)** 1.7 GHz, **(k, l)** 2.0 GHz, **(m, n)** 2.3 GHz.

in its correct position, with improved detection when compared to single frequency reconstructions. Similar results were obtained for the H-P2 phantom, which indicates robustness of the algorithm to varying target position. The target is detected also when a second known scatterer (muscle) disturbs the propagation inside the axillary region (MTS-P1, MTA-P1, MTA-P3 phantoms), which is a promising result.

It is also reported frequency hopping led to better target detection (compared to single frequency reconstructions), not only in the case of the H-P1 phantom, but also in the other phantom configurations tested, suggesting that hopping between frequencies is a valid way to improve imaging results as it explores multiple-frequency information.

The LE was quantified for each image, and it was found that in the worst-case-scenario (imaginary part of permittivity of the MTA-P1 phantom, in Fig. 5.19 (b)), LE = 24mm, which is deemed acceptable considering the discussion presented in Sec. 5.5.2.

It should be noted that these results were obtained using a reference object for calibration that corresponds to the "no-target axillary model", which is likely to lead to a successful data calibration [66], but would not be feasible in real practice. It is important to understand how results would change if a more realistic reference object for data calibration is used. This topic is addressed in Sec.5.7.

5.7 Quantification of MWT modelling error, after data calibration

The differences between the modelled setup and the actual setup are a critical source of error in MWT algorithms. For this reason, data calibration is a fundamental step as it aims to tune the E-field measured at the sources (more specifically, S-parameters) with the E-field computed by the *forward solver* used by the tomographic algorithm, which reduces the impact of *modelling errors* on imaging. This section aims to quantify the modelling

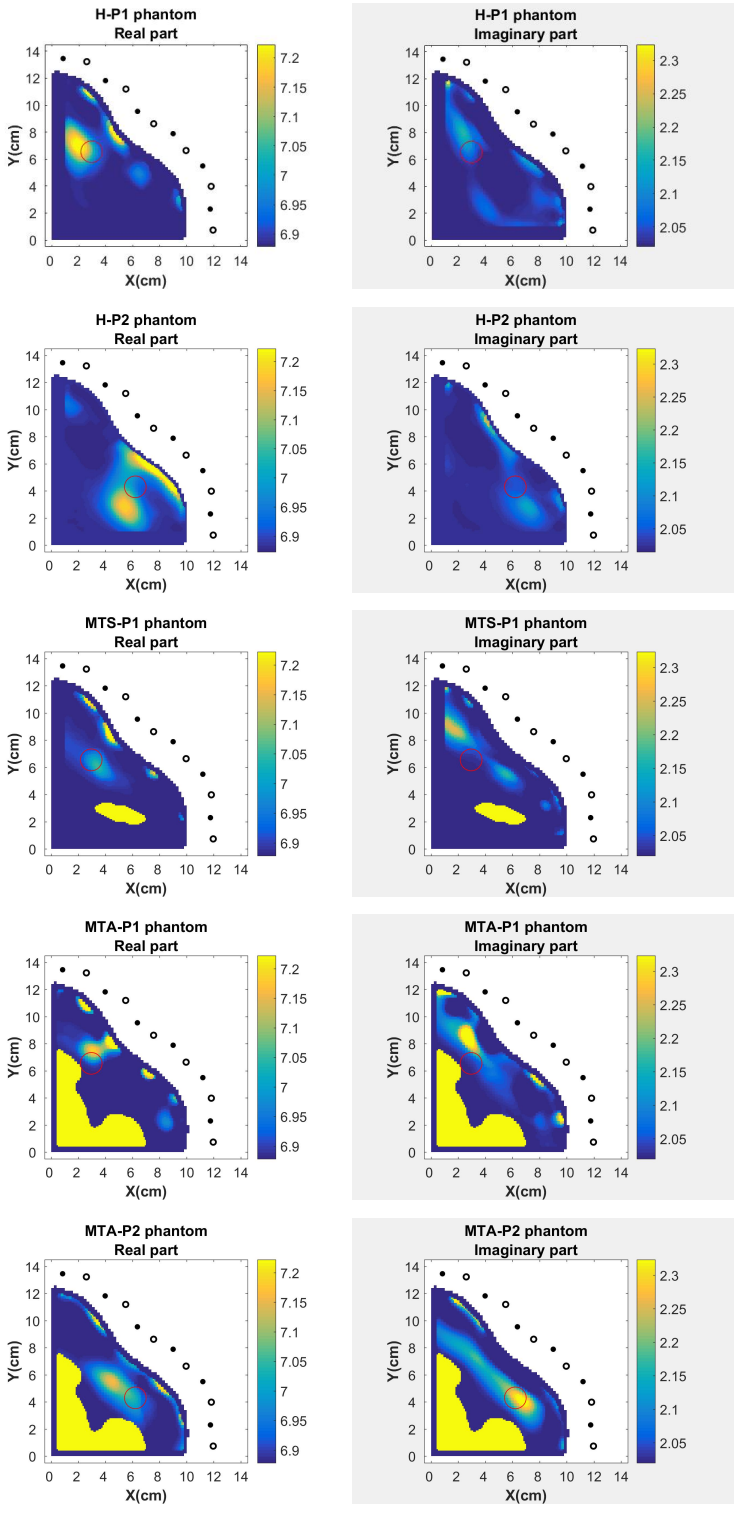

(a) (b)

Figure 5.19: Experimental imaging results obtained with frequency hopping approach, hopping between 0.8, 0.9 and 1.0 GHZ, for 5 different phantoms: H-P1, H-P2, MTS-P1, MTA-P1, MTA-P3. **(a)** Real part, and **(b)** imaginary part of relative permittivity.

error - in the case of axillary MWT - after calibrating the data with the state-of-the-art method [66], widely adopted in various medical MWT studies [60; 148]. The second aim of the section is to investigate if such error is robust to changes in the reference object adopted for calibration. From an imaging perspective, this study aims to understand if the use of different reference objects for calibration can provide similar results to those obtained when the ideal "no-target" calibration is performed. This is an important step to validate axillary MWT since the "no-target" measurement is not possible in real practice.

5.7.1 Methodology

In this study, the numerical multi-tissue simplified (MTS) axillary model (defined in Sec. 5.2.1) was considered, and a spherical ALN (radius = 8mm) was embedded in fat tissue. The model was immersed in *Glycerol 90*, and $N_A = 6$ *Monopole B* probes (Sec. 5.2.3) were placed in front of the axillary region, as shown in Fig. 5.20. The position of probes is given by: $O_A(-3mm, -9mm, \bar{z})$; $\rho = [128, 128, 128, 128, 128, 128, 128, 128]$; $\Delta\phi = 10°$. The resulting distance between adjacent antennas was $\overline{A_i A_{i+1}} = 21mm$. The average ($\pm$ standard deviation) antenna-body distance was 17*mm* ($\pm 3mm$). The position of the ALN was $P1(29, 65, \bar{z})$.

The S-parameters at the sources $S_T^{setup}(\mathbf{r}_m, \mathbf{r}_n)$ (i.e., the data) were computed in the 0.5-2.5 GHz frequency band, using full-wave simulations in the CST software. The data were then calibrated to tune them with the model using the method proposed in [66] (a detailed description of the calibration method can be found in Sec. 2.2.1.4):

$$\mathbf{E}_T^{setup,cal}(\mathbf{r}_m, \mathbf{r}_n) = \mathbf{S}_T^{setup}(\mathbf{r}_m, \mathbf{r}_n) * C(\mathbf{r}_m, \mathbf{r}_n) \tag{5.2}$$

where the computation of $C(\mathbf{r}_m, \mathbf{r}_n)$ was performed as per Eq. 2.9 and requires measuring a known reference object. Firstly, $C(\mathbf{r}_m, \mathbf{r}_n)$ was computed adopting the "no-target axillary model" as a reference setup for calibration, which represents the ideal case. Secondly, to

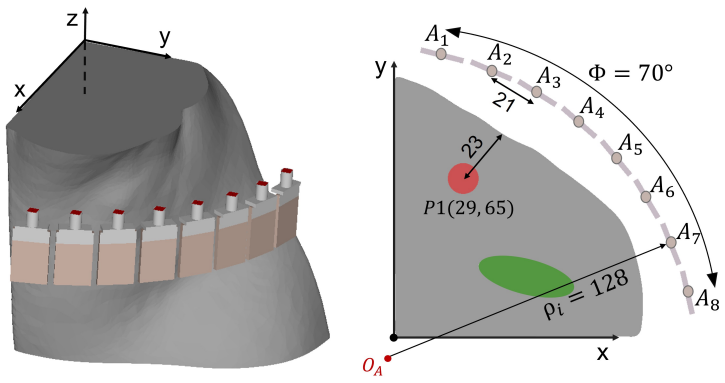

(a) (b)

Figure 5.20: Setup used to investigate the effect on varying the calibration reference object on imaging results: 8 monopole antennas are placed around the multi-tissue simplified (MTS) axillary model. **(a)** Rendering view of the setup. **(b)** Cross-sectional view of the setup at the level of the target. Distances are reported in millimeters.

assess if the modelling error and the imaging results are robust to changes in the reference object used for calibration, $C(\mathbf{r}_m, \mathbf{r}_n)$ was computed considering two other reference objects: the first consisted of the axillary phantom filled with fat, where a cylindrical object made of perfect electric conductor (PEC) was inserted; the second consisted of the axillary phantom filled only with fat. These two phantoms will be referred as *Cylindrical PEC* and *Fat only* reference objects respectively. The three reference objects adopted in this Section are illustrated in Fig. 5.21.

To quantify the modelling error after calibration, the following metric was defined:

$$error_{cal}(\mathbf{r}_m, \mathbf{r}_n) = E_T^{setup,cal}(\mathbf{r}_m, \mathbf{r}_n) - E_T^{model}(\mathbf{r}_m, \mathbf{r}_n) \tag{5.3}$$

where $E_T^{model}(\mathbf{r}_m, \mathbf{r}_n)$ is the total E-field at the sources computed using a 2D-FDTD solver with CPML boundary condition (the same model was used in Sec. 5.3-5.6 as a *forward solver*). It should be noted that $error_{cal}(\mathbf{r}_m, \mathbf{r}_n)$ is not sufficient to infer conclusions on the goodness of the calibration as this metric is data-dependent. Indeed, to evaluate if

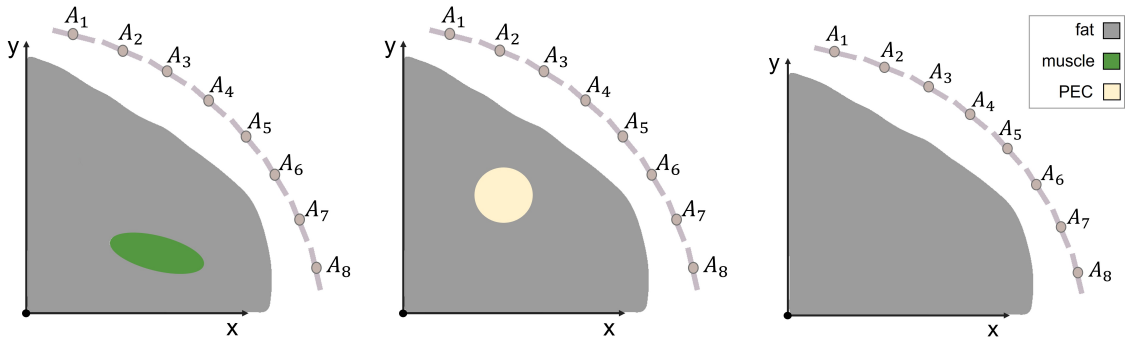

(a) Benchmark (b) *Cylindrical PEC* (c) *Fat only*

Figure 5.21: Three different reference axillary models adopted for data calibration. **(a)** Benchmark: axillary model without the ALN. **(b)** *Cylindrical PEC*: homogeneus axillary model, where a perfect electric conductor (PEC) cylinder is inserted. **(c)** *Fat only*: axillary model filled only with fat.

the modelling error is sufficiently low for the purpose of the target detection, it should be compared to the E-field scattered by the target, which is ultimately the information used by the MWT algorithm for image reconstruction. Hence, a complementary evaluation metric, Signal to Error Ratio (SER), was defined as the ratio between the scattered field in the model domain and the modelling error:

$$SER_{cal}(\mathbf{r}_m, \mathbf{r}_n) = \frac{||E_T^{model}(\mathbf{r}_m, \mathbf{r}_n) - E_B^{model}(\mathbf{r}_m, \mathbf{r}_n)||_2}{||error_{cal}(\mathbf{r}_m, \mathbf{r}_n)||_2} \tag{5.4}$$

where $E_B^{model}(\mathbf{r}_m, \mathbf{r}_n)$ is the E-field computed by the *forward model* on the "no-target axillary model"; and where $||\cdot||_2 = \sqrt{\sum|\cdot|^2}$ is the notation for the L^2 norm. One should note that $SER_{cal}(\mathbf{r}_m, \mathbf{r}_n) \to \infty$, in the case where the "inverse crime" is committed.

5.7.2 Results

Fig. 5.22 reports the magnitude of $error_{cal}(\mathbf{r}_m, \mathbf{r}_n)$ at 1.5 GHz, for the three reference setups used for data calibration. The average (across antenna pairs) $error_{cal}(\mathbf{r}_m, \mathbf{r}_n)$ is

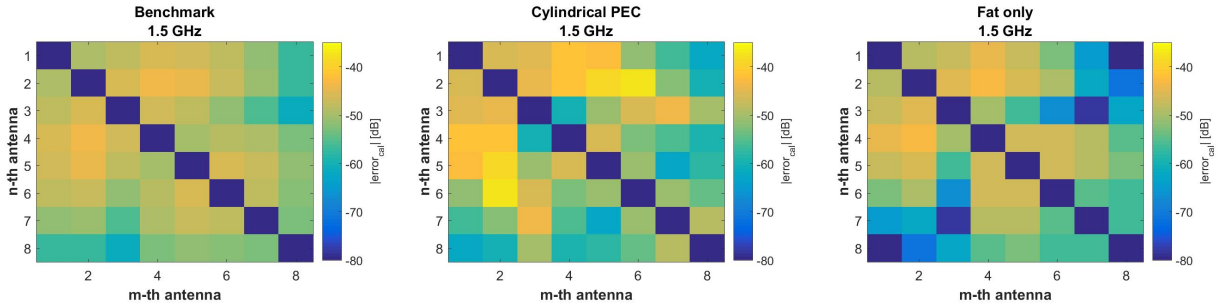

(a) (b) (c)

Figure 5.22: Magnitude of the error introduced by the calibration: the figure reports $|Error_{cal}(\mathbf{r}_m, \mathbf{r}_n)|$ for the setup reported in Fig. 5.21, when calibrating data with 3 different reference scenarios: **(a)** Benchmark ("no-target axillary model"); **(b)** *Cylindrical PEC*; **(c)** *Fat only*. Frequency = 1.5 GHz.

-50 dB for the case of the benchmark calibration setup, while it is -54dB and -50dB for the cases of *Cylindrical PEC* and *Fat only* calibration models, respectively.

Fig. 5.23 reports the SER in the 0.5-2.5 GHz frequency band for the three calibration scenarios. For the benchmark case, the average SER (across antenna pairs) is 0.5 dB. This means that the power of the modelling error is comparable to the power of the response of the target, which is expected as the calibration coefficient takes into account all the axillary tissues except for the target. Regarding the two other reference objects tested for calibration, the average SER is -4.5 dB and -3.7 dB for the cases of *Cylindrical PEC* and *Fat only* reference objects respectively. This means that the power of the modelling error is considerably higher than the power of the response of the target. Additionally, the SER for *Cylindrical PEC* and *Fat only* are lower if compared to the ideal reference object ("no-target axillary model"), which suggests that the calibration is sensitive to deviations in the shape of the reference object with respect to the ideal case.

Finally, Fig. 5.24 reports imaging results obtained when reconstructing images after calibrating data varying the reference object for calibration. Image are reconstructed hopping between 8 equally spaced frequency points between 0.5 and 1.7 GHz, with 25 DBIM-

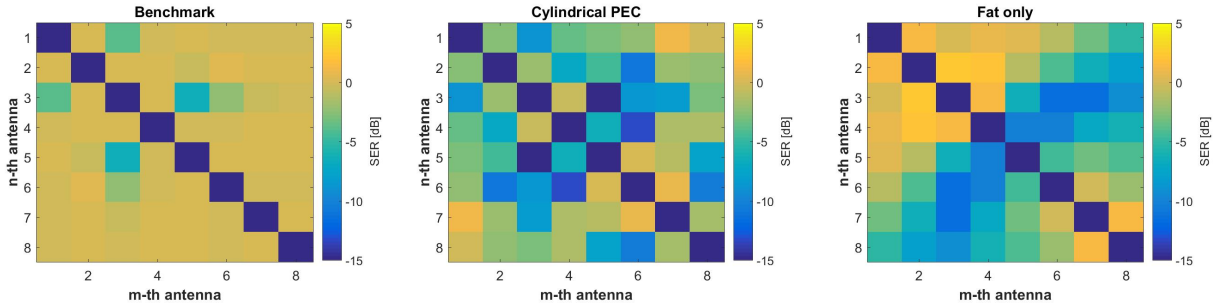

(a) (b) (c)

Figure 5.23: Signal to Error Ratio (SER) due to the modelling error, after data calibration. The figure reports $SER_{cal}(\mathbf{r}_m, \mathbf{r}_n)$ obtained after calibrating the data with three different reference objects. The setups (each with a different reference object) used for calibration are illustrated in Fig. 5.21. **(a)** benchmark; **(b)** *Cylindrical PEC*; **(c)** *Fat only*. Frequency band: 0.5-2.5 GHz.

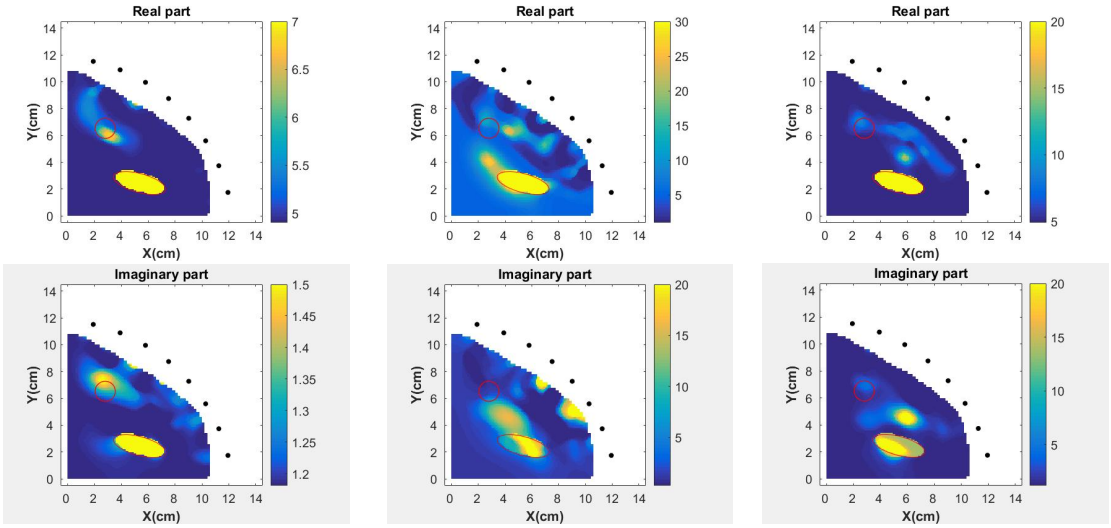

(a) Benchmark (b) *Cylindrical PEC* (c) *Fat Only*

Figure 5.24: The effect of varying reference object for data calibration on imaging results. Images are reconstructed at 1.7 GHz, when calibrating data with 3 different reference scenarios: **(a)** Ideal case ("no-target axillary model"); **(b)** *Cylindrical PEC*; **(c)** *Fat only*. Reconstruction strategy: frequency hopping between 7 equally space frequency points in the 0.5-1.7 GHz frequency band. **(Top)**: real part of permittivity; **(bottom)**: imaginary part of permittivity

TwIST iterations per frequency point. The results show that the proposed algorithm correctly detects the target when the "no-target axillary model" is used as reference object for data calibration (in line with results obtained in Sec. 5.6), but it fails in detecting the target when different reference objects (i.e., *Cylindrical PEC* or *Fat only*) are used. The results show that the proposed algorithm is not robust to changes in the reference object used for calibration, and suggest that the SER is a valid metric for modelling error assessment, which seems to correlate with imaging results.

5.8 Conclusions

This chapter assessed the feasibility of MWI for ALN detection using an anatomically realistic phantom of the axillary region.

As a first approach, a radar-based MWI setup was proposed and tested. Despite the challenges posed by the limited angular sweep of the antenna, it was found that the radar-system can detect a 5mm radius ALN embedded in fat. Additionally, the results showed that when considering the strong reflection of the nearby muscle tissue, both the muscle and the ALN are detected.

As a second approach, a MWT setup was proposed with the aim of employing available prior information on axillary anatomy to aid image reconstruction: the setup was tested in the 0.5-2.5 GHz frequency band, and consisted of an anthropomorphic phantom, immersed in glycerol-water mixtures, surrounded by monopole antennas, placed on a single transverse plane of the body.

The first investigation - performed with a simplified 2D version of the proposed setup - assessed the robustness of the DBIM algorithm to errors in prior information of axillary tissues surrounding the ALN. The results showed that, when prior knowledge of the muscle position is available, the ALN is detected in its correct position, with a good estimation of the real part of permittivity, and a slight overestimation of the imaginary part of permittiv-

ity. Additionally, results do not significantly changed when a $\pm 20\%$ error occurred in the initial estimation of the dielectric properties of the axillary tissues surrounding the target. This is considered a good result, as it suggests robustness of the DBIM algorithm to errors in the initial estimation of the dielectric properties. Regarding the robustness of the algorithm to errors in the estimation of the muscle position, for a positioning error of ± 7mm, the detection of the ALN is still acceptable; while for a ± 14mm error, the image quality deteriorates even if the ALN can still be perceived. In a nutshell, prior knowledge of muscle position is fundamental for the detection and dielectric properties estimation of ALNs. It should be noted that these results were obtained in ideal conditions, i.e. not considering the modelling error which cannot be avoided in real practice.

As further step, a numerical assessment of the application was performed using a realistic MWT prototype with 6 monopole antennas (impedance matched in the 1.1-3.5GHz band). Firstly, the challenges related with the limited angle ($70° - 90°$) available for probe placement were demonstrated: it was shown that imaging results deteriorate when removing antennas from the - not anatomically accessible - flat back-sides of the axillary model. Secondly, given the limited space available for probe placement near the axillary region, it was proposed a method that performs measurements in two subsequent steps, changing the relative angular position of antennas and phantom, to increase the amount of retrievable information. Imaging results indicated the effectiveness of such method, which was then adopted for the experimental assessment of the application.

An experimental assessment was then performed using the developed prototype. The results showed that the DBIM-TwIST can detect ALNs in different position in the axillary region, when using simplified (homogeneous) or anthropomorphic (multi-tissue) phantoms, which encourages further studies of the application.

However, it was reported that the proposed algorithm fails to estimate the dielectric properties of ALNs, probably due to the difficulties of the 2D-FDTD model in modelling the propagation of the E-field in the axillary region. For future developments of the appli-

cation, the possibility of using full-wave modelling as a forward solver is suggested.

The last study presented in this chapter proposed a new set of metrics to quantify the modelling errors which may be useful to evaluate both the capability of the model to represent the actual setup and the effectiveness of different type of calibration methods. Here, the proposed metrics were used to investigate the robustness of the calibration when varying the reference scenario with respect to the ideal case of the "no-target axillary model". The results suggested that the modelling error considerably increases when adopting more realistic reference setups for calibration, which confirms that having the possibility to measure the "no-target axillary model" is fundamental in MWT. To avoid the need for such measurement, a solution may reside in adopting the data calibration method proposed in [149], which is based on the measurement of the point spread function of the system, using an electrically very small scatterer in the known background medium.

It is recognised that the immersion liquid handling is not practical to operate in the axillary region, but - as a first approach to axillary MWT - it was important to reduce antenna size, which is critical to operate in the axillary region. For future researches, it is suggested to test an air-based setup (as our research group is already doing for a radar MWI system [35]), or to consider a wearable band where the antennas may be embedded in a semi-flexible material with known dielectric properties - a similar solution was proposed in [150].

Future work on axillary MWI should also focus on understanding how knowledge of muscle shape and position can be inferred *a priori*, bearing in mind that errors in the initial estimation of muscle/fat interface should be minimised. One strategy may reside in using radar-MWI algorithms to firstly estimate the muscle position (Sec. 5.1 suggests that this may be feasible), and then integrate this information into MWT reconstruction - an analogous approach has been proposed in the literature for breast MWI [151]. A second strategy may be to use patient-specific information (e.g., BMI) which correlates with the amount of fat laying between skin and muscle surface.

Chapter 6

Conclusions and perspectives

The work presented in this thesis focused on the assessment of MWI for the detection of ALNs. The thesis is composed of three main parts which trace the first three milestones to be reached for the development of an axillary MWI device: the first is the assessment of ALN dielectric properties; the second is the development of an anthropomorphic model and a physical phantom of the axillary region to test the intended application; the third is the development of a MWI setup and the testing of MWI algorithms.

Regarding the first part of the thesis, the dielectric properties of freshly excised animal LNs and human ALNs were measured, increasing the knowledge in this topic. It was shown that the relative permittivity of healthy ALNs is in the range between 30 and 50 at 4.5 GHz, which contrasts well with the surrounding fat tissue that has low dielectric properties, potentially enabling the detection of ALN with MWI. However, it was not possible to investigate the differences between healthy and metastasized ALNs, which is recognised as a limitation of the study. The results were published in [37]. A review on ALN dielectric properties was published in [41].

Given the challenges faced in measuring LN dielectric properties, a transmission-based dielectric measurement method was developed for measuring heterogeneous tissue such as LNs. It was shown that the setup allows propagation through 5 mm to 10 mm samples (which is sufficient for the measurements of axillary lymph nodes), while confining the

sensing volume to the region of interest. The results were published in [32].

A third approach to ALN dielectric characterization would be measuring animal LNs which underwent freezing and defrosting. To enable such measurements, the effect of freezing and defrosting biological tissues on dielectric properties was studied. It was observed that the permittivity of high water content tissues (muscle and liver) slightly increases after the samples undergo freezing and defrosting. Such variation was below +2.6% (median value at 4.5 GHz) in the real part and below +8.9% in the imaginary part, which may be considered acceptable for most applications. Regarding the low water content tissue that was studied (fat), the observed variations can be considered negligible. The results of this study were published in [152].

Regarding the second part of the thesis, an anatomically realistic axillary phantom was developed for experimental assessment of MWI for ALN screening. The phantom is made of polymeric containers and filled with liquid TMMs, which is advantageous since liquid TMMs are easy to produce and their dielectric properties can mimic the axillary tissues for the purpose of MWI. As a further investigation, the influence of the polymer on the coupling of the E-field inside the phantom was studied. It was found that the 3D-printed containers alter the E-field coupling into the tissues by 7 dB at maximum, at 4GHz. The anthropomorphic axillary region phantom was described in [37].

Regarding the last part of the thesis, axillary MWI was assessed both numerically and experimentally, using the developed anthropomorphic model. A preliminary study showed that a radar-based system can successfully detect a 5mm radius ALN embedded in a homogeneous fatty medium. Additionally, it was shown that despite the strong reflection of the muscle - caused by the high dielectric contrast between fat and muscle - a radar based system is able to distinguish an ALN from the background. This study was published in [34].

As an alternative to radar, an axillary MWT setup was proposed and tested using the DBIM for image reconstruction, with the aim to explore available prior information of

axillary anatomical information. A first approach of the algorithm was tested in a 2D configuration. It was shown that - when prior knowledge of fat-muscle interface is available - the ALN is detected with a good estimate of its dielectric properties. In addition, the robustness of the algorithm to errors in the prior estimation of fat-muscle interface was assessed: it was found that a $\pm 7mm$ positioning error does not significantly affect the ALN detection, while a $\pm 14mm$ error causes artifacts. These results were presented in [153].

A second - more realistic - approach, DBIM-based MWT, was tested considering modelling errors, generating data either with full wave simulations or experimentally. The numerical results demonstrated the challenges related with the limited angular view, which characterizes axillary MWI. Additionally, ALN MWT was tested over a broad band (0.8-2.5 GHz), considering the challenges related to the limited space available for probe placement. The possibility of performing measurement from different illumination angles was proposed as a means to increase the number of probing points in the imaging domain, and it was demonstrated to be effective in increasing the amount of retrievable information, leading to better imaging results. As a final step, an experimental assessment of the application was performed using anthropomorphic phantoms with increasing level of complexity. It was shown that the proposed system can detect ALNs in different positions in the axillary region, when using homogeneous, or multi-tissue phantoms, which is considered a promising result. It was also found that, due to modelling errors, the algorithm fails in estimating the dielectric properties of the target with an acceptable error. Both the numerical and experimental assessment on axillary MWT were published in [40].

The last study on axillary MWI focused on assessing the robustness of the data calibration method to changes in the reference scenario used for calibration. It was shown that having the possibility to measure the "no-target scenario" is fundamental to minimize the modelling error and hence to obtain reliable imaging results. As future work, a data calibration method based on the measurement of the point spread function of the system [149] may be adopted as a potential way to overcome the need for the "no-target scenario" mea-

surement, which would be crucial to assess the clinical feasibility of the application.

Appendix A

Measurement protocol for the transmission-based T$_x$OECP

Before describing the measurement protocol in detail, it is worth recalling the setup. The setup is illustrated in Fig. A.1 and consists of the following components:

- one VNA with 2 ports;
- two flexible coaxial-cables and adapters;
- two (semi-rigid) OECPs;
- one 3D-printed PLA structure that served as (i) holder for the OECPs and (ii) support table for the MUT. This structure fixes one probe, and allows the other one to move on its z-axis, while ensuring the two probes are perfectly aligned.
- one caliper to measure the MUT thickness (i.e., distance d between the two probe tips).

The T$_x$OECP measurement protocol consists of the following steps: (i) setup preparation and VNA calibration; (ii) pre-measurement validation; (iii) tissue/phantom measurements; (iv) post-measurements validation. The following paragraphs detail these steps.

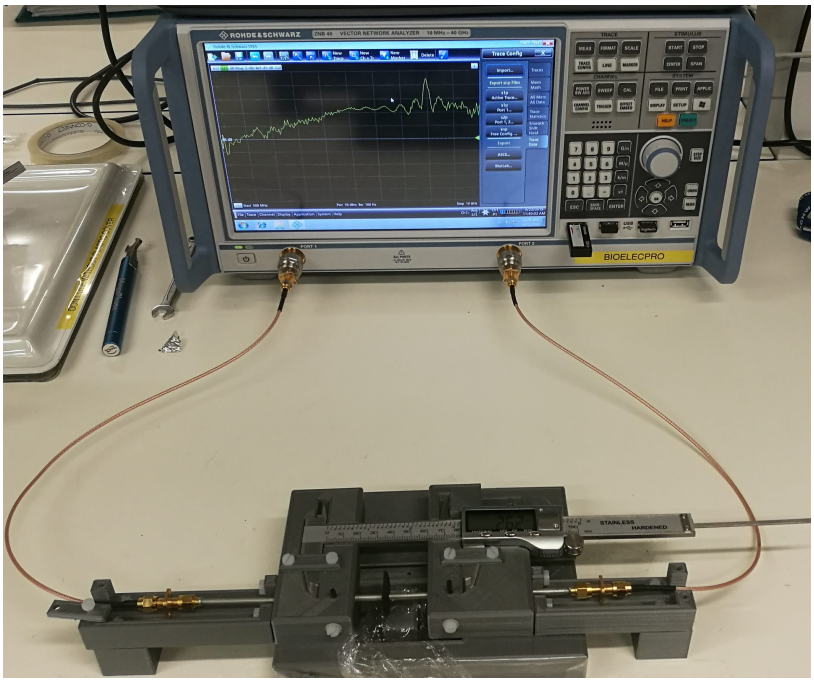

Figure A.1: Experimental setup used for transmission-based dielectric measurements. All the assembled components are present: the Vector Network Analyzer (VNA) is connected by the cables to the two Open-Ended Coaxial-Probes (OECPs), which are placed in the plastic support.

Setup preparation and VNA calibration: in this phase, the components listed in Sec. 3.2.2 are assembled and the resulting structure is fixed on a stable support in order to minimize any movement as this could affect the measurements. During the assembling procedure, the VNA is calibrated with the aid of the Electronic Calibration (E-Cal) module: the VNA calibration is performed connecting the flexible coaxial-cables to the E-Cal, when the OECPs are still not connected. Fig. A.2 illustrates how the flexible coaxial-cables should be connected to the E-Cal. This procedure moves the plane of the calibration to the tips of the flexible coaxial-cables. The OECPs (and required adapters) are excluded from the E-Cal. The wave path along these components is compensated in post-processing.

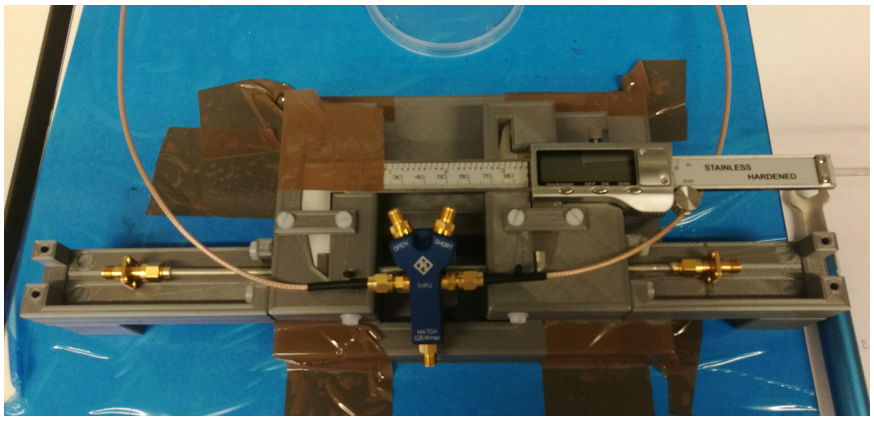

Figure A.2: Electronic calibration of the Vector Network Analyzer (VNA). The VNA is calibrated using the E-Cal module, which is connected to both flexible coaxial-cables. The VNA software guides the use of the E-Cal: the module is connected to the flexible coaxial-cables in different configurations (e.g., open-circuit, short-circuit, load). Note that the two Open-Ended Coaxial-Probes are excluded from the electronic calibration: the E-Cal module calibrates the setup up to the flexible coaxial-cable tips.

Pre-measurement validation: after calibration, a validation measurement is performed to confirm that the E-Cal was successful and to enable the calculation of the remaining uncertainties in the measurement system. The validation measurements are conducted on a set of three known phantoms, which will be referred to as "standard phantoms". The standard phantoms are made of acrylic ($\epsilon' \simeq 2.1$, over the frequency bandwidth of 0.5 GHz to 14 GHz), chosen for its homogeneity and for its stable properties over time, which ensured repeatability of the validation measurements. The dimensions of the standard phantoms are:

- Standard phantom 1: 15mm x 15mm x 2.77mm
- Standard phantom 2: 15mm x 15mm x 5.53mm
- Standard phantom 3: 15mm x 15mm x 8.25mm

For each of the standard phantoms, the following procedure is repeated: the phantom is placed on the PLA support-table; the probes are moved until they are in contact with the

sample (the sample should be slightly compressed in order to ensure good contact to the probe tips); the S_{21} is acquired averaging 25 sequential acquisitions in order to reduce noise.

MUT (tissue/phantom) measurement: the actual measurements on the MUT are performed in this phase. Similarly to the standard phantoms, the MUT is placed on the PLA support-table; the probes are moved until they touch the sample (the sample should be slightly compressed in order to ensure a good contact to the probe tips); the S_{21} is acquired averaging 25 sequential acquisitions in order to reduce noise.

When possible (i.e., when the sample is large enough), the S_{21} is measured at different probe separation-distances in order to follow the procedure proposed by Meaney et al. in [45] [1]. In order to use the equations proposed in [45], the S_{21} should be recorded considering several separation-distances. In the present work, at least 5 different separation-distances were considered). In practice, the sample is either "squeezed'" with more or less pressure (depending on the compressibiliy of the MUT and measured in different points.

Post-measurement validation: after measurement completion, the validation measurements are repeated. This procedure corresponds exactly to the one described in Pre-Measurement Validation section above. This is done to ensure that the calibration has been maintained across all the measurements. In those cases where the post-measurement validation differs significantly from the Pre-Measurement Validation, the equipment should be re-calibrated and the measurement procedure should be restarted again from the Pre-Measurement Validation phase.

[1] In Meaney's work, the analytic formulation for complex permittivity calculation requires the measurement of the S_{21} at several probe separation-distances.

Appendix B

Lymph node dielectric measurement

This appendix reports the results of all the dielectric measurements of human ALNs and sheep LNs.

Fig. B.1 reports the measurement performed on 11 human ALNs, excised from 9 patients. Each row of the figure refers to a single ALN, separating permittivity and conductivity; each graph within the same figure corresponds to the measurement of a different point on the same ALN. All the ALNs were diagnosed as "negative" after histopathological examination, i.e. no metastasis were found.

Fig. B.2 reports the measurements performed on 8 inguinal LNs, excised from 2 sheeps. Each row refers to a single LN, separating permittivity and conductivity; each graph within the same figure corresponds to the measurement of a different point on the same LN. Solid lines correspond to measurements performed on the external surface of the LN, while dashed lines correspond to measurement performed on the inner cross-section of the LN. Histopathological examination was not performed on sheep LN, however, due to their relatively young age (approximately 6 years), it is assumed that the sheeps did not develop cancer.

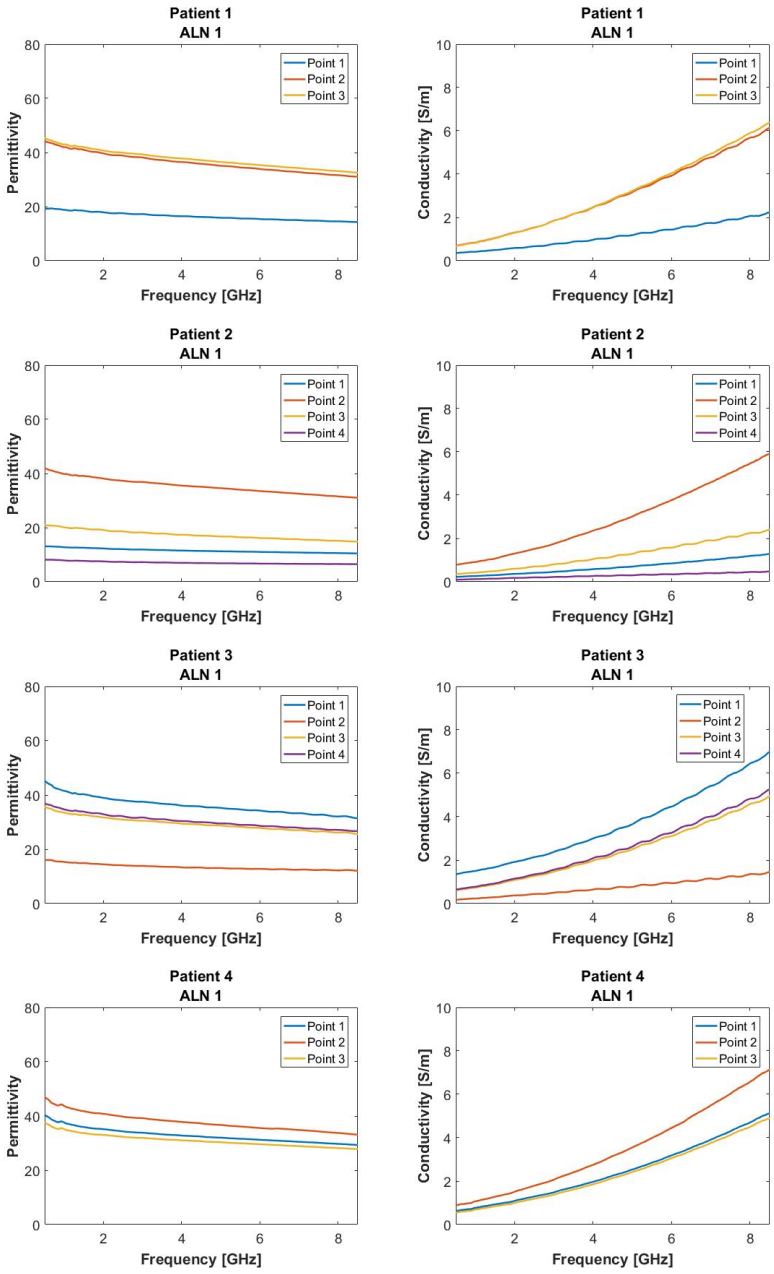

Figure B.1: Human axillary lymph node (ALN) dielectric properties. **(Left)** Permittivity and **(right)** conductivity resulting from measurements conducted on 11 ALNs excised from 9 patients. Each pair of figures in a row corresponds to the measurement of one ALN; each graph within the same figure corresponds to one measurement point. The origin of each ALN (patient number) is indicated above each figure.

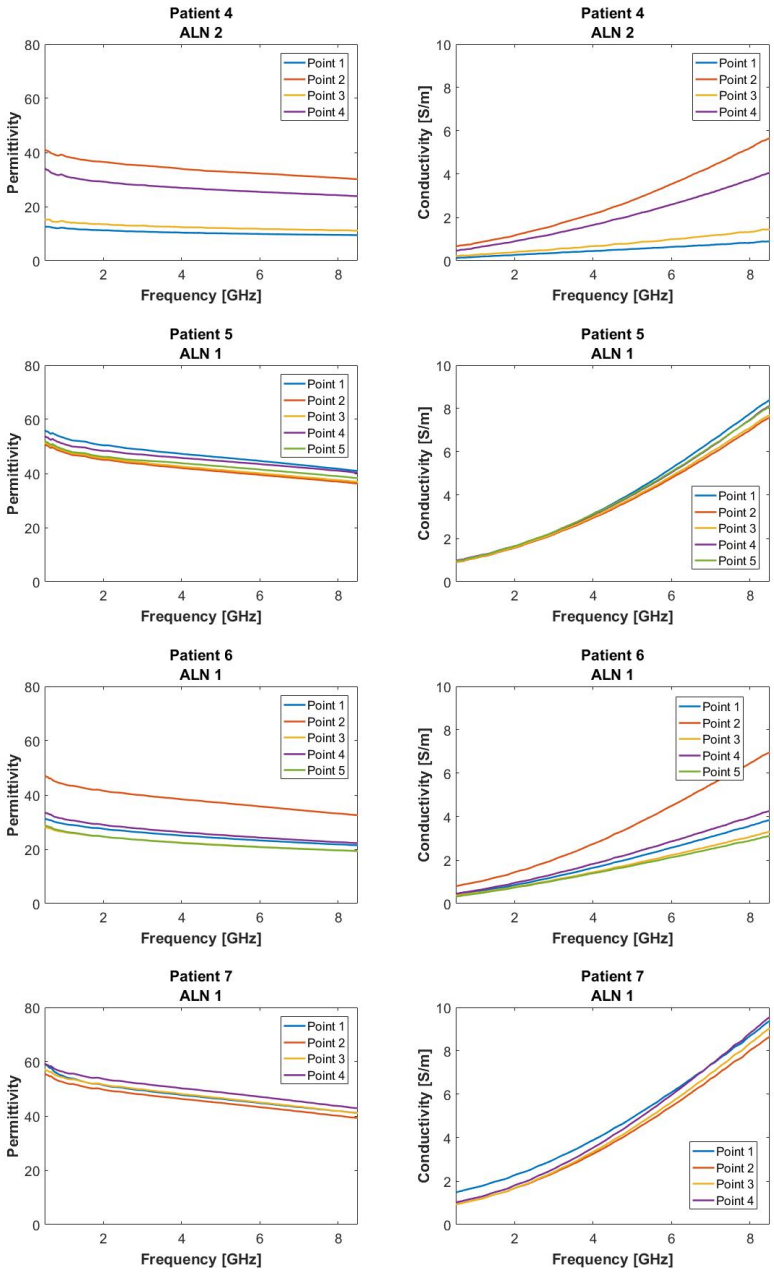

Figure B.1: *(continued)* Human ALN dielectric properties. **(Left)** Permittivity and **(right)** conductivity resulting from measurements conducted on 11 ALNs excised from 9 patients. Each pair of figures in a row corresponds to the measurement of one ALN; each graph within the same figure corresponds to one measurement point. The origin of each ALN (patient number) is indicated above each figure.

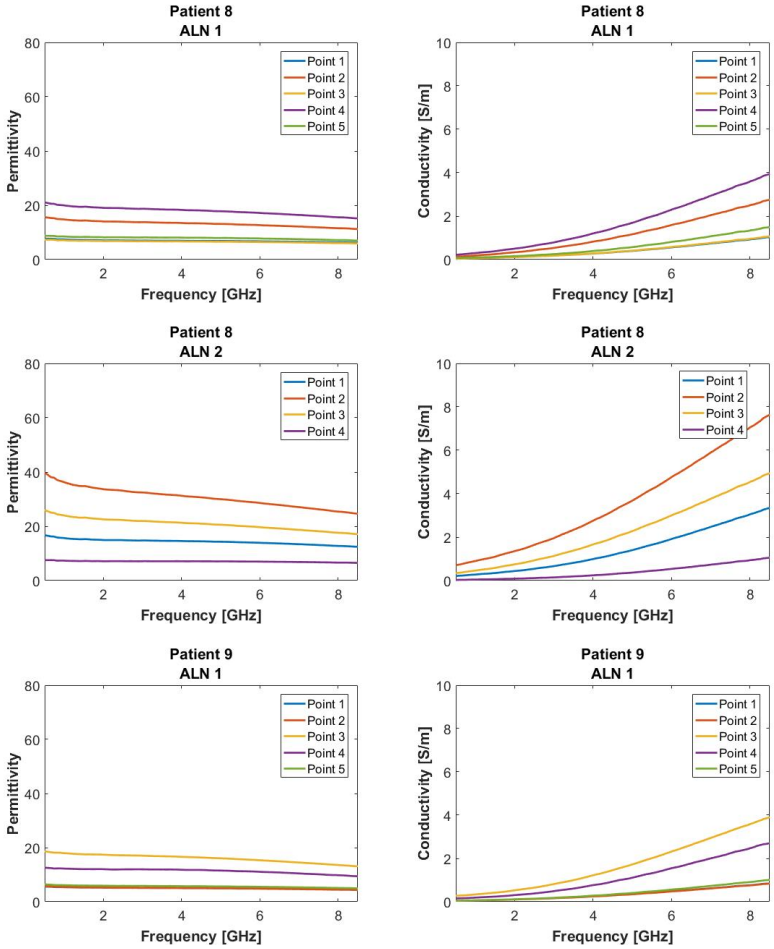

Figure B.1: *(continued)* Human ALN dielectric properties. **(Left)** Permittivity and **(right)** conductivity resulting from measurements conducted on 11 ALNs excised from 9 patients. Each pair of figures in a row corresponds to the measurement of one ALN; each graph within the same figure corresponds to one measurement point. The origin of each ALN (patient number) is indicated above each figure.

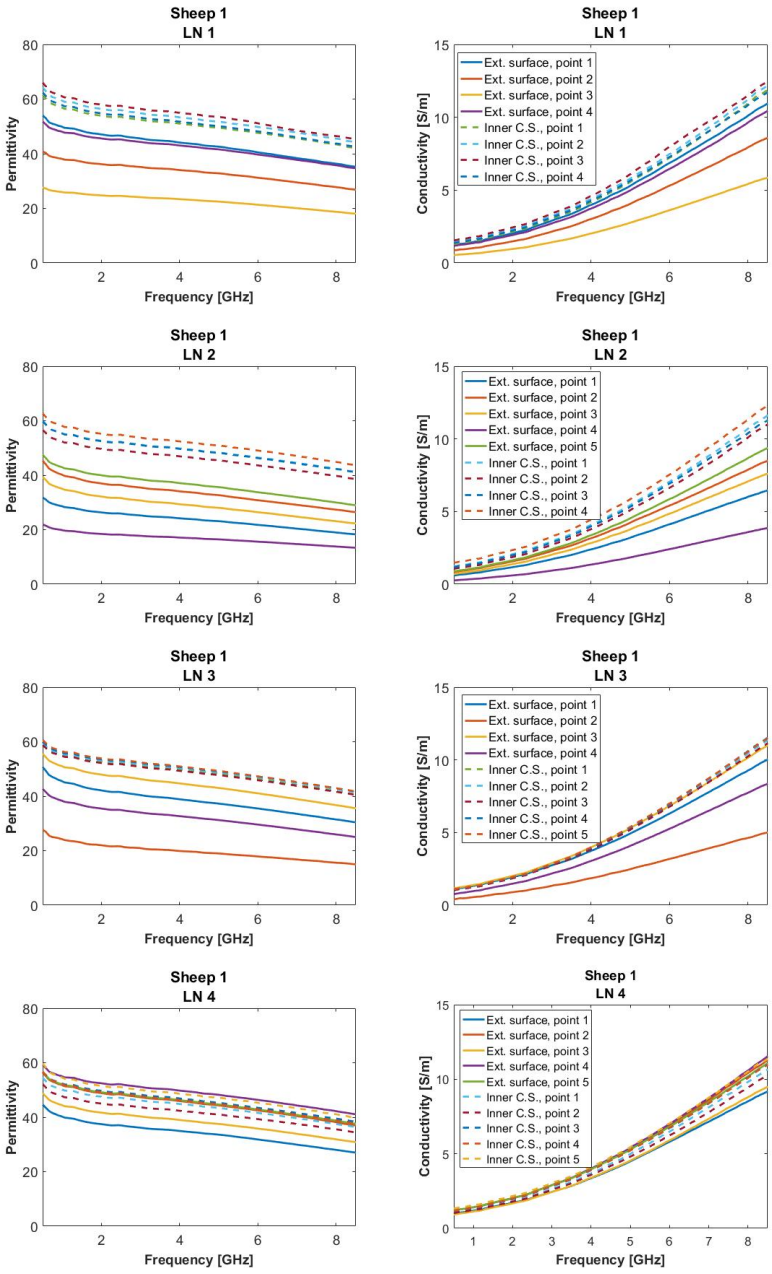

Figure B.2: Animal lymph node (LN) dielectric properties. **(Left)** Permittivity and **(right)** conductivity resulting from measurements conducted on 8 inguinal lymph nodes (LNs) excised from 2 sheep corpses. Each pair of figures in a row corresponds to the measurement of one LN; each graph within the same figure corresponds to one measurement point. **Solid lines** indicate external surface measurements; **Dashed lines** indicate inner cross-section (CS) measurements. The origin of each LN (sheep number) is indicated above each figure.

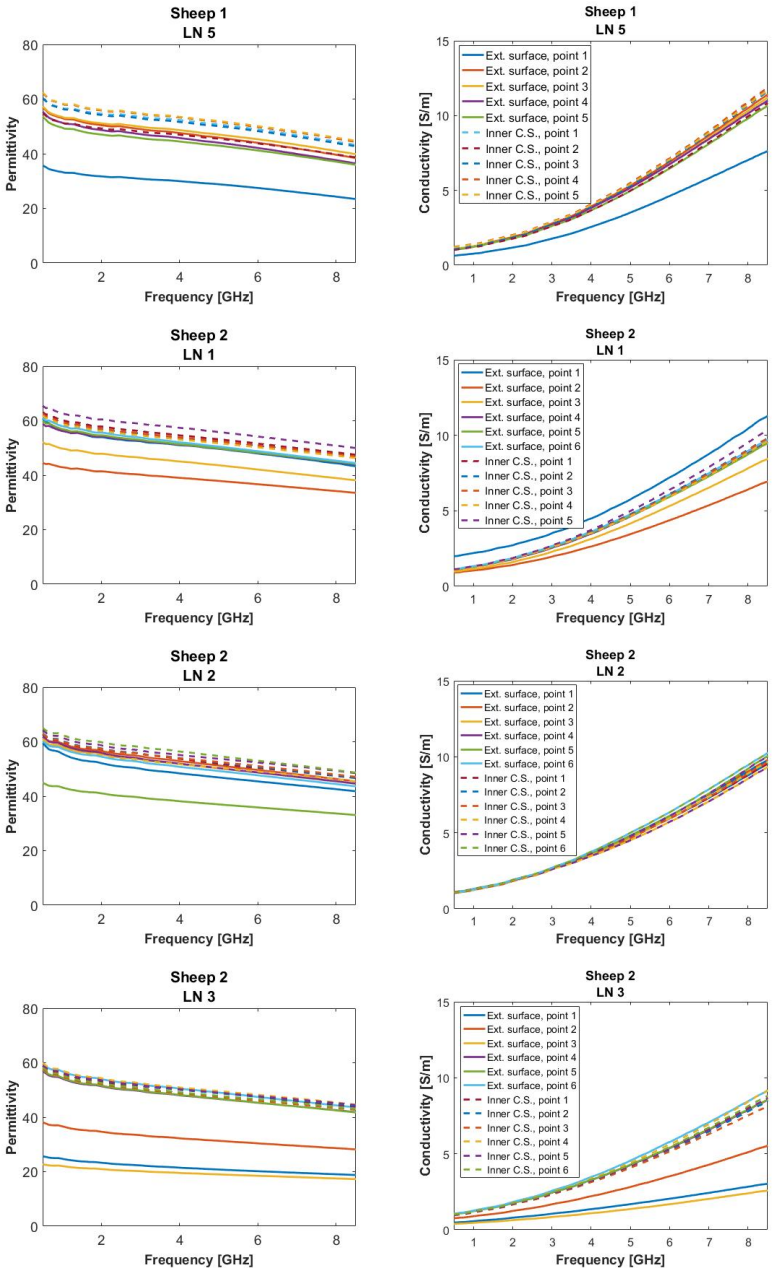

Figure B.2: (*continued*) Animal LN dielectric properties. **(Left)** Permittivity and **(right)** conductivity resulting from measurements conducted on 8 inguinal lymph nodes (LNs) excised from 2 sheep corpses. Each pair of figures in a row corresponds to the measurement of one LN; each graph within the same figure corresponds to one measurement point. **Solid lines** indicate external surface measurements; **Dashed lines** indicate inner cross-section (CS) measurements. The origin of each LN (sheep number) is indicated above each figure.

References

[1] "Breast Cancer Fact Sheets," *World Health Organization*, 2020, http://gco.iarc.fr/today [Available online], accessed on 09/2022.

[2] A. E. Giuliano, S. B. Edge, and G. N. Hortobagyi, "Eighth Edition of the AJCC Cancer Staging Manual: Breast Cancer," *Annals of Surgical Oncology*, vol. 25, no. 7, pp. 1783–1785, 2018.

[3] G. Hortobagyi, "Physician to Physician AJCC 8^{th} Edition," https://www.facs.org/media/u4djjc4v/breast-8th-ed.pdf, 2017, [Available online]. Accesses on 09/2022.

[4] W. Pawlina and M. H. Ross, *Histology: a Text and Atlas: with Correlated Cell and Molecular Biology*. Lippincott Williams & Wilkins, 2018.

[5] D. Male, *Histology, Microscopy, Anatomy and Disease*. OpenLearn, the Open University, https://www.open.edu/openlearn/mod/oucontent/view.php?id=65373&section=2.2 [Available online]. Accessed on 07/2022.

[6] G. C. Bentel, L. B. Marks, P. H. Hardenbergh, and L. R. Prosnitz, "Variability of the Depth of Supraclavicular and Axillary Lymph Nodes in Patients with Breast Cancer: is a Posterior Axillary Boost Field Necessary?" *International Journal of Radiation Oncology - Biology - Physics*, vol. 47, no. 3, pp. 755–758, 2000.

[7] B. Ludescher, M. Rommel, T. Willmer, A. Fritsche, F. Schick, and J. Machann, "Subcutaneous Adipose Tissue Thickness in Adults - Correlation with BMI and Rec-

ommendations for Pen Needle Lengths for Subcutaneous Self-Injection," *Clinical Endocrinology*, vol. 75, no. 6, pp. 786–790, 2011.

[8] M. Houshyari, A. S. Y. Kashi, S. S. Varaki, A. Rakhsha, and E. R. Blookat, "Regional Lymph Node Radiotherapy in Breast Cancer: Single Anterior Supraclavicular Field vs. Two Anterior and Posterior Opposed Supraclavicular Fields," *Electronic Physician*, vol. 7, no. 2, pp. 1032–1038, 2015.

[9] S. Kalli, A. Semine, S. Cohen, S. P. Naber, S. S. Makim, and M. Bahl, "American Joint Committee on Cancer's Staging System for Breast Cancer: What the Radiologist Needs to Know," *Radiographics*, vol. 38, no. 7, pp. 1921–1933, 2018.

[10] G. H. Lyman, A. E. Giuliano, M. R. Somerfield, A. B. Benson III, D. C. Bodurka, H. J. Burstein, A. J. Cochran, H. S. Cody III, S. B. Edge, S. Galper *et al.*, "American Society of Clinical Oncology Guideline Recommendations for Sentinel Lymph Node Biopsy in Early-Stage Breast Cancer," *Journal of Clinical Oncology*, vol. 23, no. 30, pp. 7703–7720, 2005.

[11] U. Veronesi, F. Rilke, A. Luini, V. Sacchini, V. Galimberti, T. Campa, E. D. Bei, M. Greco, A. Magni, M. Merson *et al.*, "Distribution of Axillary Node Metastases by Level of Invasion. An Analysis of 539 Cases," *Cancer*, vol. 59, no. 4, pp. 682–687, 1987.

[12] P. P. Rosen, M. L. Lesser, D. W. Kinne, and E. J. Beattie, "Discontinuous or "Skip" Metastases in Breast Carcinoma. Analysis of 1228 Axillary Dissections." *Annals of Surgery*, vol. 197, no. 3, p. 276, 1983.

[13] U. Veronesi, G. Paganelli, G. Viale, A. Luini, S. Zurrida, V. Galimberti, M. Intra, P. Veronesi, C. Robertson, P. Maisonneuve *et al.*, "A Randomized Comparison

of Sentinel-Node Biopsy with Routine Axillary Dissection in Breast Cancer," *New England Journal of Medicine*, vol. 349, no. 6, pp. 546–553, 2003.

[14] D. L. Morton, J. F. Thompson, R. Essner, R. Elashoff, S. L. Stern, O. E. Nieweg, D. F. Roses, C. P. Karakousis, N. Mozzillo, D. Reintgen *et al.*, "Validation of the Accuracy of Intraoperative Lymphatic Mapping and Sentinel Lymphadenectomy for Early-Stage Melanoma: a Multicenter Trial," *Annals of Surgery*, vol. 230, no. 4, pp. 453–463, 1999.

[15] R. E. Mansel, L. Fallowfield, M. Kissin, A. Goyal, R. G. Newcombe, J. M. Dixon, C. Yiangou, K. Horgan, N. Bundred, I. Monypenny *et al.*, "Randomized Multicenter Trial of Sentinel Node Biopsy Versus Standard Axillary Treatment in Operable Breast Cancer: the ALMANAC Trial," *Journal of the National Cancer Institute*, vol. 98, no. 9, pp. 599–609, 2006.

[16] D. N. Krag, S. J. Anderson, T. B. Julian, A. M. Brown, S. P. Harlow, T. Ashikaga, D. L. Weaver, B. J. Miller, L. M. Jalovec, T. G. Frazier *et al.*, "Technical Outcomes of Sentinel-Lymph-Node Resection and Conventional Axillary-Lymph-Node Dissection in Patients with Clinically Node-Negative Breast Cancer: Results from the NSABP B-32 Randomised Phase III Trial," *The Lancet Oncology*, vol. 8, no. 10, pp. 881–888, 2007.

[17] V. E. Mortellaro, J. Marshall, L. Singer, S. N. Hochwald, M. Chang, E. M. Copeland, and S. R. Grobmyer, "Magnetic Resonance Imaging for Axillary Staging in Patients with Breast Cancer," *Journal of Magnetic Resonance Imaging: An Official Journal of the International Society for Magnetic Resonance in Medicine*, vol. 30, no. 2, pp. 309–312, 2009.

[18] P. A. Baltzer, M. Dietzel, H. P. Burmeister, R. Zoubi, M. Gajda, O. Camara, and W. A. Kaiser, "Application of MR Mammography beyond Local Staging: Is There a

Potential to Accurately Assess Axillary Lymph Nodes? Evaluation of an Extended Protocol in an Initial Prospective Study," *American Journal of Roentgenology*, vol. 196, no. 5, pp. W641–W647, 2011.

[19] S. Alvarez, E. Añorbe, P. Alcorta, F. López, I. Alonso, and J. Cortés, "Role of Sonography in the Diagnosis of Axillary Lymph Node Metastases in Breast Cancer: a Systematic Review," *American Journal of Roentgenology*, vol. 186, no. 5, pp. 1342–1348, 2006.

[20] S. M. Dudea, M. Lenghel, D. Vasilescu, and M. M. Duma, "Ultrasonography of Superficial Lymph Nodes: Benign vs. Malignant," *Medical Ultrasonography*, vol. 14, no. 4, pp. 294–306, 2012.

[21] D. M. Holwitt, M. E. Swatske, W. E. Gillanders, B. S. Monsees, F. Gao, R. L. Aft, T. J. Eberlein, and J. A. Margenthaler, "The Combination of Axillary Ultrasound and Ultrasound-Guided Biopsy Is an Accurate Predictor of Axillary Stage in Clinically Node-Negative Breast Cancer Patients," *American Journal of Surgery*, vol. 196, no. 4, p. 477, 2008.

[22] M. Greco, F. Crippa, R. Agresti, E. Seregni, A. Gerali, R. Giovanazzi, A. Micheli, S. Asero, C. Ferraris, M. Gennaro *et al.*, "Axillary Lymph Node Staging in Breast Cancer by 2-Fluoro-2-Deoxy-D-Glucose-Positron Emission Tomography: Clinical Evaluation and Alternative Management," *Journal of the National Cancer Institute*, vol. 93, no. 8, pp. 630–635, 2001.

[23] R. L. Wahl, B. A. Siegel, R. E. Coleman, and C. G. Gatsonis, "Prospective Multicenter Study of Axillary Nodal Staging by Positron Emission Tomography in Breast Cancer: a Report of the Staging Breast Cancer with PET Study Group," *Journal of Clinical Oncology*, vol. 22, no. 2, pp. 277–285, 2004.

[24] J. Liu and S. G. Hay, "Prospects for Microwave Imaging of the Lymphatic System in the Axillary," in *IEEE-APS Topical Conference on Antennas and Propagation in Wireless Communications (APWC), Cairns, Australia.* IEEE, 2016, pp. 183–186.

[25] A. Malich, T. Fritsch, C. Mauch, T. Boehm, M. Freesmeyer, M. Fleck, R. Anderson, and W. Kaiser, "Electrical Impedance Scanning: a New Technique in the Diagnosis of Lymph Nodes in Which Malignancy Is Suspected on Ultrasound," *The British Journal of Radiology*, vol. 74, no. 877, pp. 42–47, 2001.

[26] S. C. Hagness, A. Taflove, and J. E. Bridges, "Two-Dimensional FDTD Analysis of a Pulsed Microwave Confocal System for Breast Cancer Detection: Fixed-Focus and Antenna-Array Sensors," *IEEE Transactions on Biomedical Engineering*, vol. 45, no. 12, pp. 1470–1479, 1998.

[27] Y. Xie, B. Guo, L. Xu, J. Li, and P. Stoica, "Multistatic Adaptive Microwave Imaging for Early Breast Cancer Detection," *IEEE Transactions on Biomedical Engineering*, vol. 53, no. 8, pp. 1647–1657, 2006.

[28] R. C. Conceição, J. J. Mohr, and M. O'Halloran, *An Introduction to Microwave Imaging for Breast Cancer Detection*. Springer, 2016.

[29] R. Eleutério, A. Medina, and R. C. Conceição, "Initial Study with Microwave Imaging of the Axilla to Aid Breast Cancer Diagnosis," in *USNC-URSI Radio Science Meeting (Joint with AP-S Symposium), Memphis, TN, USA*. IEEE, 2014, p. 306.

[30] R. Eleutério and R. C. Conceição, "Initial Study for Detection of Multiple Lymph Nodes in the Axillary Region Using Microwave Imaging," in *9th European Conference on Antennas and Propagation (EuCAP), Lisbon, Portugal*. IEEE, 2015, pp. 1–3.

[31] D. M. Godinho, J. M. Felício, T. Castela, N. M. Silva, L. M. Orvalho, C. A. Fernandes, and R. C. Conceição, "Extracting Dielectric Properties for MRI-Based Phantoms for Axillary Microwave Imaging Device," in *14th European Conference on Antennas and Propagation (EuCAP), Copenhagen, Denmark.*, pp. 1–4.

[32] M. Savazzi, E. Porter, M. O'Halloran, J. R. Costa, C. Fernandes, J. M. Felicío, and R. C. Conceição, "Development of a Transmission-Based Open-Ended Coaxial-Probe Suitable for Axillary Lymph Node Dielectric Measurements," in *14th European Conference on Antennas and Propagation (EuCAP), Copenhagen, Denmark.* IEEE, 2020, pp. 1–5.

[33] D. M. Godinho, J. M. Felício, T. Castela, N. A. Silva, L. M. Orvalho, C. A. Fernandes, and R. C. Conceição, "Development of MRI-Based Axillary Numerical Models and Estimation of Axillary Lymph Node Dielectric Properties for Microwave Imaging," *Medical Physics*, vol. 48, no. 10, pp. 5974–5990, 2021.

[34] M. Savazzi, J. R. Costa, C. A. Fernandes, J. M. Felício, and R. C. Conceição, "Numerical Assessment of Microwave Imaging for Axillary Lymph Nodes Screening Using Anthropomorphic Phantom," in *15th European Conference on Antennas and Propagation (EuCAP), Dusseldorf, Germany.* IEEE, 2021, pp. 1–4.

[35] D. M. Godinho, J. M. Felício, C. A. Fernandes, and R. C. Conceição, "Experimental Evaluation of an Axillary Microwave Imaging System to Aid Breast Cancer Staging," *IEEE Journal of Electromagnetics, RF and Microwaves in Medicine and Biology*, vol. 6, no. 9, pp. 68–76, 2021.

[36] D. M. Godinho, C. Silva, C. Baleia, J. M. Felício, T. Castela, N. A. Silva, M. L. Orvalho, C. A. Fernandes, and R. C. Conceição, "Modelling Level I Axillary Lymph Nodes depth for Microwave Imaging," *Physica Medica*, vol. 104, pp. 160–166, 2022.

[37] M. Savazzi, S. Abedi, N. Ištuk, N. Joachimowicz, H. Roussel, E. Porter, M. O'Halloran, J. R. Costa, C. A. Fernandes, J. M. Felício, and R. C. Conceição, "Development of an Anthropomorphic Phantom of the Axillary Region for Microwave Imaging Assessment," *Sensors*, vol. 20, no. 17, pp. 49–68, 2020.

[38] D. M. Godinho, "Microwave Imaging to Improve Breast Cancer Diagnosis," Ph.D. dissertation, Faculdade de Ciências da Universidade de Lisboa, 2022.

[39] M. Pato, R. Eleutério, R. C. Conceição, and D. M. Godinho, "Evaluating the Performance of Algorithms in Axillary Microwave Imaging towards Improved Breast Cancer Staging," *Sensors*, vol. 23, no. 3, p. 1496, 2023.

[40] M. Savazzi, O. Karadima, D. O. R. Duarte, J. T. Vasquez, F. Vipiana, P. Kosmas, C. A. Fernandes, J. M. Felício, and R. C. Conceição, "Experimental assessment of axillary lymph node microwave tomography using anthropomorphic phantoms," *IEEE Journal of Electromagnetics, RF and Microwaves in Medicine and Biology*, 2023.

[41] F. Vipiana and L. Crocco, *Electromagnetic Imaging for a Novel Generation of Medical Devices - Fundamental Issues, Methodological Challenges and Practical Implementation*. Springer, 2023 (*expected*).

[42] J. W. Choi, J. Cho, Y. Lee, J. Yim, B. Kang, K. K. Oh, W. H. Jung, H. J. Kim, C. Cheon, H.-D. Lee *et al.*, "Microwave Detection of Metastasized Breast Cancer Cells in the Lymph Node; Potential Application for Sentinel Lymphadenectomy," *Breast Cancer Research and Treatment*, vol. 86, no. 2, pp. 107–115, 2004.

[43] T. Cameron, M. Okoniewski, E. Fear, D. Mew, B. Banks, and T. Ogilvie, "A Preliminary Study of the Electrical Properties of Healthy and Diseased Lymph Nodes,"

in *14th International Symposium on Antenna Technology and Applied Electromagnetics & the American Electromagnetics Conference, Ottawa, ON, Canada*. IEEE, 2010, pp. 1–3.

[44] "Agilent Basics of Measuring the Dielectric Properties of Materials," http://academy.cba.mit.edu/classes/input_devices/meas.pdf, 2006, [Available online], accessed on 09/2022.

[45] P. Meaney, T. Rydholm, and H. Brisby, "A Transmission-Based Dielectric Property Probe for Clinical Applications," *Sensors*, vol. 18, no. 10, p. 3484, 2018.

[46] D. M. Hagl, D. Popovic, S. C. Hagness, J. H. Booske, and M. Okoniewski, "Sensing Volume of Open-Ended Coaxial Probes for Dielectric Characterization of Breast Tissue at Microwave Frequencies," *IEEE Transactions on Microwave Theory and Techniques*, vol. 51, no. 4, pp. 1194–1206, 2003.

[47] D. Popovic, M. Okoniewski, D. Hagl, J. Booske, and S. Hagness, "Volume Sensing Properties of Open-Ended Coaxial Probes for Dielectric Spectroscopy of Breast Tissue," in *IEEE Antennas and Propagation Society International Symposium (Digest). Held in conjunction with: USNC/URSI National Radio Science Meeting, Boston, MA, USA*. IEEE, 2001, pp. 254–257.

[48] S. Gabriel, R. Lau, and C. Gabriel, "The Dielectric Properties of Biological Tissues: II. Measurements in the Frequency Range 10 Hz to 20 GHz," *Physics in Medicine & Biology*, vol. 41, no. 11, p. 2251, 1996.

[49] A. Peyman, S. Holden, S. Watts, R. Perrott, and C. Gabriel, "Dielectric Properties of Porcine Cerebrospinal Tissues at Microwave Frequencies: in Vivo, in Vitro and Systematic Variation with Age," *Physics in Medicine & Biology*, vol. 52, no. 8, p. 2229, 2007.

[50] F. M. Ghannouchi and R. G. Bosisio, "Measurement of Microwave Permittivity Using a Six-Port Reflectometer with an Open-Ended Coaxial Line," *IEEE Transactions on Instrumentation and Measurement*, vol. 38, no. 2, pp. 505–508, 1989.

[51] J. S. Bobowski and T. Johnson, "Permittivity Measurements of Biological Samples by an Open-Ended Coaxial Line," *Progress In Electromagnetics Research B*, vol. 40, pp. 159–183, 2012.

[52] A. La Gioia, M. O'Halloran, A. Elahi, and E. Porter, "Investigation of Histology Radius for Dielectric Characterisation of Heterogeneous Materials," *IEEE Transactions on Dielectrics and Electrical Insulation*, vol. 25, no. 3, pp. 1064–1079, 2018.

[53] N. K. Nikolova, *Introduction to Microwave Imaging*. Cambridge University Press, 2017.

[54] W. C. Chew and Y.-M. Wang, "Reconstruction of Two-Dimensional Permittivity Distribution Using the Distorted Born Iterative Method," *IEEE Transactions on Medical Imaging*, vol. 9, no. 2, pp. 218–225, 1990.

[55] J. D. Shea, P. Kosmas, S. C. Hagness, and B. D. Van Veen, "Three-Dimensional Microwave Imaging of Realistic Numerical Breast Phantoms via a Multiple-Frequency Inverse Scattering Technique," *Medical Physics*, vol. 37, no. 8, pp. 4210–4226, 2010.

[56] Z. Miao and P. Kosmas, "Multiple-Frequency DBIM-TwIST Algorithm for Microwave Breast Imaging," *IEEE Transactions on Antennas and Propagation*, vol. 65, no. 5, pp. 2507–2516, 2017.

[57] M. Koutsoupidou, P. Kosmas, S. Ahsan, Z. Miao, I. Sotiriou, and T. Kallos, "Towards a Microwave Imaging Prototype Based on the DBIM-TwIST Algorithm and a Custom-Made Transceiver System," in *International Conference on Electromagnetics in Advanced Applications (ICEAA), Rome, Italy.* IEEE, 2017, pp. 1004–1007.

[58] S. Ahsan, Z. Guo, Z. Miao, I. Sotiriou, M. Koutsoupidou, E. Kallos, G. Palikaras, and P. Kosmas, "Design and Experimental Validation of a Multiple-Frequency Microwave Tomography System Employing the DBIM-TwIST Algorithm," *Sensors*, vol. 18, no. 10, p. 3491, 2018.

[59] Z. Miao, S. Ahsan, P. Kosmas, J. A. Tobon Vasquez, F. Vipiana, M. Casu, and M. Vacca, "Application of the DBIM-TwIST Algorithm to Experimental Microwave Imaging Data," in *11th European Conference on Antennas and Propagation (EuCAP), Paris, France*. IEEE, 2017, pp. 1611–1614.

[60] O. Karadima, M. Rahman, I. Sotiriou, N. Ghavami, P. Lu, S. Ahsan, and P. Kosmas, "Experimental Validation of Microwave Tomography with the DBIM-TwIST Algorithm for Brain Stroke Detection and Classification," *Sensors*, vol. 20, no. 3, p. 840, 2020.

[61] S. Gabriel, R. Lau, and C. Gabriel, "The Dielectric Properties of Biological Tissues: III. Parametric Models for the Dielectric Spectrum of Tissues," *Physics in Medicine And Biology*, vol. 41, pp. 2271–2293.

[62] Z. Miao, "Implementation and Optimisation of Microwave Medical Imaging Based on the Multiple-Frequency DBIM-TwIST Algorithm," *King's College London, United Kingdom*, 2018.

[63] O. Karadima, "Validation of Microwave Imaging Algorithms for Medical Devices," Ph.D. dissertation, King's College London, 2023.

[64] P. Lu, "Development of novel algorithms for microwave medical imaging applications," Ph.D. dissertation, King's College London, 2023.

[65] J. M. Bioucas-Dias and M. A. Figueiredo, "A new TwIST: Two-Step Iterative

Shrinkage/Thresholding Algorithms for Image Restoration," *IEEE Transactions on Image Processing*, vol. 16, no. 12, pp. 2992–3004, 2007.

[66] M. Ostadrahimi, P. Mojabi, C. Gilmore, A. Zakaria, S. Noghanian, S. Pistorius, and J. LoVetri, "Analysis of Incident Field Modeling and Incident/Scattered Field Calibration Techniques in Microwave Tomography," *IEEE Antennas and Wireless Propagation Letters*, vol. 10, pp. 900–903, 2011.

[67] W. T. Joines, Y. Zhang, C. Li, and R. L. Jirtle, "The Measured Electrical Properties of Normal and Malignant Human Tissues from 50 to 900 MHz," *Medical Physics*, vol. 21, no. 4, pp. 547–550, 1994.

[68] X. Yu, Y. Sun, K. Cai, H. Yu, D. Zhou, D. Lu, and S. X. Xin, "Dielectric Properties of Normal and Metastatic Lymph Nodes ex Vivo from Lung Cancer Surgeries," *Bioelectromagnetics*, vol. 41, no. 2, pp. 148–155, 2020.

[69] D. Lu, H. Yu, Z. Wang, Z. Chen, J. Fan, X. Liu, J. Zhai, H. Wu, X. Yu, and K. Cai, "Classification of Metastatic and Non-Metastatic Thoracic Lymph Nodes in Lung Cancer Patients Based on Dielectric Properties Using Adaptive Probabilistic Neural Networks," *Frontiers in Oncology*, vol. 11, p. 376, 2021.

[70] D. Lu, J. Peng, Z. Wang, Y. Sun, J. Zhai, Z. Wang, Z. Chen, Y. Matsumoto, L. Wang, S. X. Xin, and K. Cai, "Dielectric Property Measurements for the Rapid Differentiation of Thoracic Lymph nodes Using XGBoost in Patients with Non-Small Cell Lung Cancer: a Self-Control Clinical Trial," *Translational Lung Cancer Research*, vol. 11, no. 3, p. 342, 2022.

[71] P. M. Meaney, A. P. Gregory, N. R. Epstein, and K. D. Paulsen, "Microwave Open-Ended Coaxial Dielectric Probe: Interpretation of the Sensing Volume re-Visited," *BMC Medical Physics*, vol. 14, no. 1, pp. 1–11, 2014.

[72] "CST Studio Suite," https://www.3ds.com/products-services/simulia/products/cst-studio-suite/, accessed on 09/2022.

[73] A. Kiourti, J. R. Costa, C. A. Fernandes, A. G. Santiago, and K. S. Nikita, "Miniature Implantable Antennas for Biomedical Telemetry: from Simulation to Realization," *IEEE Transactions on Biomedical Engineering*, vol. 59, no. 11, pp. 3140–3147, 2012.

[74] T. Karacolak, R. Cooper, E. S. Unlu, and E. Topsakal, "Dielectric Properties of Porcine Skin Tissue and in Vivo Testing of Implantable Antennas Using Pigs as Model Animals," *IEEE Antennas and Wireless Propagation Letters*, vol. 11, pp. 1686–1689, 2012.

[75] P. Stauffer, F. Rossetto, M. Prakash, D. Neuman, and T. Lee, "Phantom and Animal Tissues for Modelling the Electrical Properties of Human Liver," *International Journal of Hyperthermia*, vol. 19, no. 1, pp. 89–101, 2003.

[76] C. Gabriel and A. Peyman, "Dielectric Measurement: Error Analysis and Assessment of Uncertainty," *Physics in Medicine & Biology*, vol. 51, no. 23, p. 6033, 2006.

[77] "Keysight 85070E, Dielectric Probe Kit 200 MHz to 50 GHz," https://www.keysight.com/us/en/assets/7018-01196/technical-overviews/5989-0222.pdf, [Online PDF]. Accessed on 09/2022.

[78] A. La Gioia, E. Porter, I. Merunka, A. Shahzad, S. Salahuddin, M. Jones, and M. O'Halloran, "Open-Ended Coaxial Probe Technique for Dielectric Measurement of Biological Tissues: Challenges and Common Practices," *Diagnostics*, vol. 8, no. 2, p. 40, 2018.

[79] A. Peyman, C. Gabriel, and E. Grant, "Complex Permittivity of Sodium Chloride Solutions at Microwave Frequencies," *Bioelectromagnetics: Journal of the Bioelec-*

tromagnetics Society, The Society for Physical Regulation in Biology and Medicine, The European Bioelectromagnetics Association, vol. 28, no. 4, pp. 264–274, 2007.

[80] G. Maenhout, T. Markovic, I. Ocket, and B. Nauwelaers, "Effect of Open-Ended Coaxial Probe-to-Tissue Contact Pressure on Dielectric Measurements," *Sensors*, vol. 20, no. 7, p. 2060, 2020.

[81] E. Porter, A. La Gioia, S. Salahuddin, S. Decker, A. Shahzad, M. A. Elahi, M. O'Halloran, and O. Beyan, "Minimum Information for Dielectric Measurements of Biological Tissues (MINDER): A Framework for Repeatable and Reusable Data," *International Journal of RF and Microwave Computer-Aided Engineering*, vol. 28, no. 3, p. e21201, 2018.

[82] A. Campbell and D. Land, "Dielectric Properties of Female Human Breast Tissue Measured in Vitro at 3.2 GHz," *Physics in Medicine & Biology*, vol. 37, no. 1, p. 193, 1992.

[83] "A Large-Scale Study of the Ultrawideband Microwave Dielectric Properties of Normal, Benign and Malignant Breast Tissues Obtained from Cancer Surgeries, author=Lazebnik, Mariya and Popovic, Dijana and McCartney, Leah and Watkins, Cynthia B and Lindstrom, Mary J and Harter, Josephine and Sewall, Sarah and Ogilvie, Travis and Magliocco, Anthony and Breslin, Tara M and others, journal=Physics in Medicine & Biology, volume=52, number=20, pages=6093, year=2007, publisher=IOP Publishing."

[84] "MyWAVE COST Action: Open-access Repository of Dielectric and Thermal Properties of Biological Tissues," 2022, Available from 10/2022. [Online]. Available: https://www.um.edu.mt/projects/mywave/data-repository/

[85] "University Hospital Galway (Galway, Ireland)," Website: https://saolta.ie/hospital/university-hospital-galway, accessed on 09/2022.

[86] P. M. Meaney, A. P. Gregory, J. Seppälä, and T. Lahtinen, "Open-Ended Coaxial Dielectric Probe Effective Penetration Depth Determination," *IEEE Transactions on Microwave Theory and Techniques*, vol. 64, no. 3, pp. 915–923, 2016.

[87] W. D. Hurt, "Multiterm Debye Dispersion Relations for Permittivity of Muscle," *IEEE Transactions on Biomedical Engineering*, no. 1, pp. 60–64, 1985.

[88] A. Shahzad, S. Khan, M. Jones, R. M. Dwyer, and M. O'Halloran, "Investigation of the Effect of Dehydration on Tissue Dielectric Properties in Ex Vivo Measurements," *Biomedical Physics & Engineering Express*, vol. 3, no. 4, p. 045001, 2017.

[89] "Instituto Nacional de Investigação Agrária e Veterinária (INIAV), Lisbon, Portugal," Website: http://www.iniav.pt/, accessed on 10/2020.

[90] N. Bengtsson, J. Melin, K. Remi, and S. Säoderlind, "Measurements of the Dielectric Properties of Frozen and Defrosted Meat and Fish in the Frequency Range 10–200 MHz," *Journal of the Science of Food and Agriculture*, vol. 14, no. 8, pp. 592–604, 1963.

[91] B. Bodakian and F. Hart, "The Dielectric Properties of Meat," *IEEE Transactions on Dielectrics and Electrical Insulation*, vol. 1, no. 2, pp. 181–187, 1994.

[92] S. Ley, S. Schilling, O. Fiser, J. Vrba, J. Sachs, and M. Helbig, "Ultra-Wideband Temperature Dependent Dielectric Spectroscopy of Porcine Tissue and Blood in the Microwave Frequency Range," *Sensors*, vol. 19, no. 7, p. 1707, 2019.

[93] M. Lazebnik, M. C. Converse, J. H. Booske, and S. C. Hagness, "Ultrawideband Temperature-Dependent Dielectric Properties of Animal Liver Tissue in the Mi-

crowave Frequency Range," *Physics in Medicine & Biology*, vol. 51, no. 7, p. 1941, 2006.

[94] T. W. Beck, "The Importance of a Priori Sample Size Estimation in Strength and Conditioning Research," *The Journal of Strength & Conditioning Research*, vol. 27, no. 8, pp. 2323–2337, 2013.

[95] J. Cohen, *Statistical Power Analysis for the Behavioral Sciences*. Academic press, 2013.

[96] "G*Power 3.1 Manual," https://www.psychologie.hhu.de/fileadmin/redaktion/Fakultaeten/Mathematisch-Naturwissenschaftliche_Fakultaet/Psychologie/AAP/gpower/GPowerManual.pdf, chapter 22. [Online PDF]. Accessed on 09/2022.

[97] H. Fallahi, J. Sebek, and P. Prakash, "Broadband Dielectric Properties of Ex Vivo Bovine Liver Tissue Characterized at Ablative Temperatures," *IEEE Transactions on Biomedical Engineering*, vol. 68, no. 1, pp. 90–98, 2020.

[98] P. Basaran, N. Basaran-Akgul, and B. Rasco, "Dielectric Properties of Chicken and Fish Muscle Treated with Microbial Transglutaminase," *Food Chemistry*, vol. 120, no. 2, pp. 361–370, 2010.

[99] M. Lazebnik, E. L. Madsen, G. R. Frank, and S. C. Hagness, "Tissue-Mimicking Phantom Materials for Narrowband and Ultrawideband Microwave Applications," *Physics in Medicine & Biology*, vol. 50, no. 18, p. 4245, 2005.

[100] M. Klemm, J. Leendertz, D. Gibbins, I. Craddock, A. Preece, and R. Benjamin, "Microwave Radar-Based Breast Cancer Detection: Imaging in Inhomogeneous Breast Phantoms," *IEEE Antennas and Wireless Propagation Letters*, vol. 8, pp. 1349–1352, 2009.

[101] A. Mashal, F. Gao, and S. C. Hagness, "Heterogeneous Anthropomorphic Phantoms with Realistic Dielectric Properties for Microwave Breast Imaging Experiments," *Microwave and Optical Technology Letters*, vol. 53, no. 8, pp. 1896–1902, 2011.

[102] A. A. Bakar, A. Abbosh, and M. Bialkowski, "Fabrication and Characterization of a Heterogeneous Breast Phantom for Testing an Ultrawideband Microwave Imaging System," in *Asia-Pacific Microwave Conference 2011, Melbourne, VI, Australia*. IEEE, 2011, pp. 1414–1417.

[103] C. Hahn and S. Noghanian, "Heterogeneous Breast Phantom Development for Microwave Imaging Using Regression Models," *International Journal of Biomedical Imaging*, vol. 2012, p. 6, 2012.

[104] M. J. Burfeindt, T. J. Colgan, R. O. Mays, J. D. Shea, N. Behdad, B. D. Van Veen, and S. C. Hagness, "MRI-Derived 3-D-Printed Breast Phantom for Microwave Breast Imaging Validation," *IEEE Antennas and Wireless Propagation Letters*, vol. 11, pp. 1610–1613, 2012.

[105] N. Joachimowicz, C. Conessa, T. Henriksson, and B. Duchêne, "Breast Phantoms for Microwave Imaging," *IEEE Antennas and Wireless Propagation Letters*, vol. 13, pp. 1333–1336, 2014.

[106] B. L. Oliveira, D. O'Loughlin, M. O'Halloran, E. Porter, M. Glavin, and E. Jones, "Microwave Breast Imaging: Experimental Tumour Phantoms for the Evaluation of New Breast Cancer Diagnosis Systems," *Biomedical Physics & Engineering Express*, vol. 4, no. 2, p. 025036, 2018.

[107] J. Garrett and E. Fear, "A New Breast Phantom with a Durable Skin Layer for Microwave Breast Imaging," *IEEE Transactions on Antennas and Propagation*, vol. 63, no. 4, pp. 1693–1700, 2015.

[108] N. Joachimowicz, B. Duchêne, C. Conessa, and O. Meyer, "Anthropomorphic Breast and Head Phantoms for Microwave Imaging," *Diagnostics*, vol. 8, no. 4, p. 85, 2018.

[109] B. J. Mohammed and A. M. Abbosh, "Realistic Head Phantom to Test Microwave Systems for Brain Imaging," *Microwave and Optical Technology Letters*, vol. 56, no. 4, pp. 979–982, 2014.

[110] B. McDermott, E. Porter, A. Santorelli, B. Divilly, L. Morris, M. Jones, B. McGinley, and M. O'Halloran, "Anatomically and Dielectrically Realistic Microwave Head Phantom with Circulation and Reconfigurable Lesions," *Progress in Electromagnetics Research B*, 2017.

[111] S. Salahuddin, B. McDermott, E. Porter, M. O'Halloran, M. A. Elahi, and A. Shahzad, "An Empirical Dielectric Mixing Model for Biological Tissues," in *13th European Conference on Antennas and Propagation (EuCAP), Krakow, Poland.* IEEE, 2019, pp. 1–5.

[112] "Fundação Champalimaud (Lisbon, Portugal)," Website: https://fchampalimaud.org/, accessed on 09/2022.

[113] "What is the Body Mass Index?" Website: https://www.nhs.uk/common-health-questions/lifestyle/what-is-the-body-mass-index-bmi/#:~:text=For%20most%20adults%2C%20an%20ideal,well%20as%20height%20and%20weight., accessed on 09/2022.

[114] "FormLabs," Available online: https://formlabs.com/, accessed on 09/2022.

[115] "3D Slicer," https://www.slicer.org/, accessed on 09/2022.

[116] A. Fedorov, R. Beichel, J. Kalpathy-Cramer, J. Finet, J.-C. Fillion-Robin, S. Pujol, C. Bauer, D. Jennings, F. Fennessy, M. Sonka *et al.*, "3D Slicer as an Image Comput-

ing Platform for the Quantitative Imaging Network," *Magnetic Resonance Imaging*, vol. 30, no. 9, pp. 1323–1341, 2012.

[117] M. van Eijnatten, R. van Dijk, J. Dobbe, G. Streekstra, J. Koivisto, and J. Wolff, "CT Image Segmentation Methods for Bone Used in Medical Additive Manufacturing," *Medical Engineering & Physics*, vol. 51, pp. 6–16, 2018.

[118] M. van Eijnatten, J. Koivisto, K. Karhu, T. Forouzanfar, and J. Wolff, "The Impact of Manual Threshold Selection in Medical Additive Manufacturing," *International Journal of Computer Assisted Radiology and Surgery*, vol. 12, no. 4, pp. 607–615, 2017.

[119] T. Rydholm, A. Fhager, M. Persson, S. D. Geimer, and P. M. Meaney, "Effects of the Plastic of the Realistic Geeps-L2E-Breast Phantom," *Diagnostics*, vol. 8, no. 3, p. 61, 2018.

[120] P. Cingoni, M. Corsini, and G. Ranzuglia, "Meshlab: an Open-Source 3D Mesh Processing System," *Ercim News*, vol. 63, pp. 45–46, 2008.

[121] L. R. Herrmann, "Laplacian-Isoparametric Grid Generation Scheme," *Journal of the Engineering Mechanics Division*, vol. 102, no. 5, pp. 749–907, 1976.

[122] "Blender," Available online: https://www.blender.org/, accessed on 09/2022.

[123] "Proto-pasta conductive PLA," Available online: https://www.proto-pasta.com/pages/conductive-pla, accessed on 09/2022.

[124] "Ultimaker 3," Available online: https://ultimaker.com/, accessed on 09/2022.

[125] P. Hasgall, F. Di Gennaro, C. Baumgartner, E. Neufeld, B. Lloyd, M. Gosselin, D. Payne, A. Klingenböck, and N. Kuster, "IT'IS Database for Thermal and Elec-

tromagnetic Parameters of Biological Tissues," itis.swiss/database, version 4.0, May 2018.

[126] B. Faenger, S. Ley, M. Helbig, J. Sachs, and I. Hilger, "Breast Phantom with a Conductive Skin Layer and Conductive 3D-Printed Anatomical Structures for Microwave Imaging," in *11th European Conference on Antennas and Propagation (EuCAP), Paris, France*. IEEE, 2017, pp. 1065–1068.

[127] N. Joachimowicz, C. Conessa, T. Henriksson, and B. Duchêne, "Breast Phantoms for Microwave Imaging," *IEEE Antennas and Wireless Propagation Letters*, vol. 13, pp. 1333–1336, 2014.

[128] A. Santorelli, O. Laforest, E. Porter, and M. Popović, "Image Classification for a Time-Domain Microwave Radar System: Experiments with Stable Modular Breast Phantoms," in *9th European Conference on Antennas and Propagation (EuCAP), Lisbon, Portugal*. IEEE, 2015, pp. 1–5.

[129] J. M. Felício, C. A. Fernandes, and J. R. Costa, "Complex Permittivity and Anisotropy Measurement of 3D-Printed PLA at Microwaves and Millimeter-Waves," in *22nd International Conference on Applied Electromagnetics and Communications (ICECOM), Dubrovnik, Croatia.* IEEE, 2016, pp. 1–6.

[130] J. R. Costa, C. R. Medeiros, and C. A. Fernandes, "Performance of a Crossed Exponentially Tapered Slot Antenna for UWB Systems," *IEEE Transactions on Antennas and Propagation*, vol. 57, no. 5, pp. 1345–1352, 2009.

[131] J. M. Felício, J. M. Bioucas-Dias, J. R. Costa, and C. A. Fernandes, "Antenna Design and Near-Field Characterization for Medical Microwave Imaging Applications," *IEEE Transactions on Antennas and Propagation*, vol. 67, no. 7, pp. 4811–4824, 2019.

[132] J. M. Felicio, J. M. Bioucas-Dias, J. R. Costa, and C. A. Fernandes, "Microwave Breast Imaging Using a Dry Setup," *IEEE Transactions on Computational Imaging*, 2019.

[133] J. A. Tobon Vasquez, R. Scapaticci, G. Turvani, M. Ricci, L. Farina, A. Litman, M. R. Casu, L. Crocco, and F. Vipiana, "Noninvasive Inline Food Inspection via Microwave Imaging Technology: an Application Example in the Food Industry," *IEEE Antennas and Propagation Magazine*, vol. 62, no. 5, pp. 18–32, 2020.

[134] M. Bevacqua, L. Crocco, L. Di Donato, T. Isernia, and R. Palmeri, "Exploiting Sparsity and Field Conditioning in Subsurface Microwave Imaging of Nonweak Buried Targets," *Radio Science*, vol. 51, no. 4, pp. 301–310, 2016.

[135] D. Kurrant, A. Baran, J. LoVetri, and E. Fear, "Integrating Prior Information into Microwave Tomography Part 1: Impact of Detail on Image Quality," *Medical physics*, vol. 44, no. 12, pp. 6461–6481, 2017.

[136] M. Klemm, J. Leendertz, D. Gibbins, I. Craddock, A. Preece, and R. Benjamin, "Microwave Radar-Based Breast Cancer Detection: Imaging in Inhomogeneous Breast Phantoms," *IEEE Antennas and Wireless Propagation Letters*, vol. 8, pp. 1349–1352, 2009.

[137] G. Ruvio, R. Solimene, A. Cuccaro, D. Gaetano, J. E. Browne, and M. J. Ammann, "Breast Cancer Detection Using Interferometric MUSIC: Experimental and Numerical Assessment," *Medical Physics*, vol. 41, no. 10, p. 103101, 2014.

[138] D. Byrne, M. Sarafianou, and I. J. Craddock, "Compound Radar Approach for Breast Imaging," *IEEE Transactions on Biomedical Engineering*, vol. 64, no. 1, pp. 40–51, 2016.

[139] M. Solis-Nepote, T. Reimer, and S. Pistorius, "An Air-Operated Bistatic System for Breast Microwave Radar Imaging: Pre-Clinical validation," in *41st Annual International Conference of the IEEE Engineering in Medicine and Biology Society (EMBC), Berlin, Germany.*, 2019, pp. 1859–1862.

[140] J. R. Costa and C. A. Fernandes, "Broadband Slot Feed for Integrated Lens Antennas," *IEEE Antennas and Wireless Propagation Letters*, vol. 6, pp. 396–400, 2007.

[141] J. M. Lopez-Sanchez and J. Fortuny-Guasch, "3-D Radar Imaging Using Range Migration Techniques," *IEEE Transactions on Antennas and Propagation*, vol. 48, no. 5, pp. 728–737, 2000.

[142] O. Bucci, L. Crocco, and T. Isernia, "Improving the Reconstruction Capabilities in Inverse Scattering Problems by Exploitation of Close-Proximity Setups," *Journal of the Optical Society of America A: Optics and Image Science, and Vision*, vol. 16, no. 7, pp. 1788–1798, 1999.

[143] Z. Miao, P. Kosmas, and S. Ahsan, "Impact of Information Loss on Reconstruction Quality in Microwave Tomography for Medical Imaging," *Diagnostics*, vol. 8, no. 3, p. 52, 2018.

[144] J. A. Tobon Vasquez, R. Scapaticci, G. Turvani, G. Bellizzi, N. Joachimowicz, B. Duchêne, E. Tedeschi, M. R. Casu, L. Crocco, and F. Vipiana, "Design and Experimental Assessment of a 2D Microwave Imaging System for Brain Stroke Monitoring," *International Journal of Antennas and Propagation*, vol. 2019, 2019.

[145] W. Guo, S. Ahsan, M. He, M. Koutsoupidou, and P. Kosmas, "Printed Monopole Antenna Designs for a Microwave Head Scanner," in *18th Mediterranean Microwave Symposium (MMS), Istanbul, Turkey.* IEEE, 2018, pp. 384–386.

[146] D. Kurrant, E. Fear, A. Baran, and J. LoVetri, "Integrating Prior Information into Microwave Tomography Part 2: Impact of Errors in Prior Information on Microwave Tomography Image Quality," *Medical physics*, vol. 44, no. 12, pp. 6482–6503, 2017.

[147] O. M. Bucci, L. Crocco, and R. Scapaticci, "On the Optimal Measurement Configuration for Magnetic Nanoparticles-Enhanced Breast Cancer Microwave Imaging," *IEEE Transactions on Biomedical Engineering*, vol. 62, no. 2, pp. 407–414, 2014.

[148] D. O. Rodriguez-Duarte, J. A. Tobon Vasquez, R. Scapaticci, G. Turvani, M. Cavagnaro, M. R. Casu, L. Crocco, and F. Vipiana, "Experimental Validation of a Microwave System for Brain Stroke 3-D Imaging," *Diagnostics*, vol. 11, no. 7, p. 1232, 2021.

[149] S. Tu, J. McCombe, D. Shumakov, and N. Nikolova, "Fast Quantitative Microwave Imaging with Resolvent Kernel Extracted from Measurements," *Inverse Problems*, vol. 31, no. 4, p. 045007, 2015.

[150] D. O. Rodriguez-Duarte, J. A. Tobon Vasquez, R. Scapaticci, L. Crocco, and F. Vipiana, "Brick-Shaped Antenna Module for Microwave Brain Imaging Systems," *IEEE Antennas and Wireless Propagation Letters*, vol. 19, no. 12, pp. 2057–2061, 2020.

[151] A. Baran, D. J. Kurrant, A. Zakaria, E. C. Fear, and J. LoVetri, "Breast Imaging Using Microwave Tomography with Radar-Based Tissue-Regions Estimation," *Progress In Electromagnetics Research*, vol. 149, pp. 161–171, 2014.

[152] M. Savazzi, J. M. Felício, J. R. Costa, C. A. Fernandes, and R. C. Conceição, "Study of Freezing and Defrosting Effects on Complex Permittivity of Biological Tissues," *IEEE Antennas and Wireless Propagation Letters*, vol. 20, no. 12, pp. 2210–2214, 2021.

[153] M. Savazzi, O. Karadima, J. M. Felício, C. A. Fernandes, P. Kosmas, and R. C. Conceição, "Effect of Varying Prior Information in Axillary 2D Microwave Tomography," in *16th European Conference on Antennas and Propagation (EuCAP), Madrid, Spain.* IEEE, 2022, pp. 1–5.